S-matrix Bootstrap: Towards Inelasticity

José Manuel da Silva Rainha Pereira
Mestrado em Física
Departamento de Física e Astronomia
2022

Orientador
Miguel Sousa da Costa, Centro de Física do Porto

Coorientador
António Leite Antunes, Centro de Física do Porto

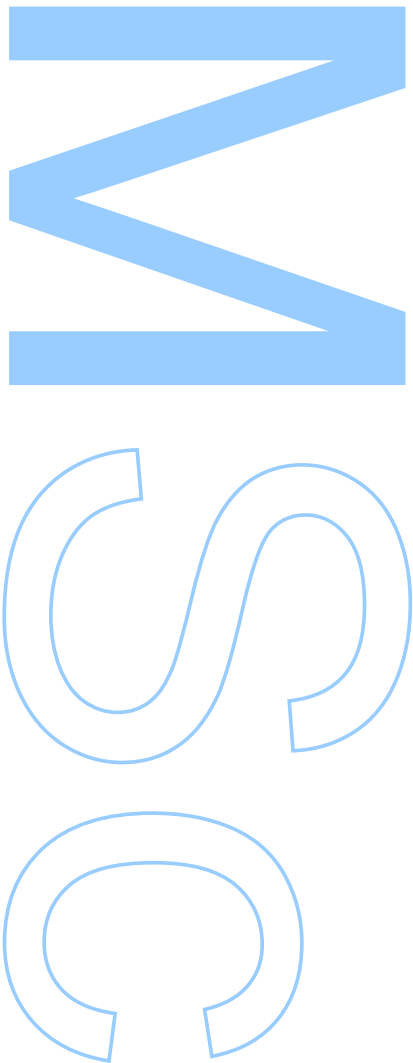

U.PORTO

FACULDADE DE CIÊNCIAS
UNIVERSIDADE DO PORTO

Todas as correções determinadas pelo júri, e só essas, foram efetuadas.

O Presidente do Júri,

Porto, _____/_____/_____

Declaração de Honra

Eu, José Manuel da Silva Rainha Pereira, inscrito no Mestrado em Física da Faculdade de Ciências da Universidade do Porto declaro, nos termos do disposto na alínea a) do artigo 14.º do Código Ético de Conduta Académica da U.Porto, que o conteúdo da presente dissertação reflete as perspetivas, o trabalho de investigação e as minhas interpretações no momento da sua entrega.

Ao entregar esta dissertação, declaro, ainda, que a mesma é resultado do meu próprio trabalho de investigação e contém contributos que não foram utilizados previamente noutros trabalhos apresentados a esta ou outra instituição.

Mais declaro que todas as referências a outros autores respeitam escrupulosamente as regras da atribuição, encontrando-se devidamente citadas no corpo do texto e identificadas na secção de referências bibliográficas. Não são divulgados na presente dissertação quaisquer conteúdos cuja reprodução esteja vedada por direitos de autor.

Tenho consciência de que a prática de plágio e auto-plágio constitui um ilícito académico.

José Manuel da Silva Rainha Pereira

Porto, 11 de outubro de 2022

UNIVERSIDADE DO PORTO

MASTERS THESIS

S-matrix Bootstrap: Towards Inelasticity

Author:
José PEREIRA

Supervisor:
Miguel COSTA

Co-supervisor:
António ANTUNES

A thesis submitted in fulfilment of the requirements
for the degree of MSc. Physics

at the

Faculdade de Ciências da Universidade do Porto
Departamento de Física e Astronomia

" We count these moments. These moments when we dare to aim higher, to break barriers, to reach for the stars, to make the unknown known. We count these moments as our proudest achievements. "

Matthew McConaughey as *Joseph "Coop" Cooper*, Interstellar

Acknowledgements

The journey through the realms of the S-matrix Bootstrap was long and full of hardships. However, it was not a lone endeavour.

First and foremost, I must thank Miguel Costa, my advisor, for giving me the opportunity to work in the high energies field, showing me that Physics can be as alluring as it can be enigmatic. In addition, some credit must also be given to António Antunes, my co-advisor. Had I not met him, certainly this experience would have been completely different. I cannot thank him enough for the numerous enlightening discussions, for being a great role model and, above all else, for being a kind human. All the moments we shared together will serve as lessons for my future career. A special thanks to Aditya Hebbar, Alexandre Homrich, Andrea Guerrieri, João Penedones, Miguel Correia and Pedro Vieira, brilliant physicist whose discussions helped elevate this thesis.

Secondly, I am deeply grateful to a handful of people, in particular Gonçalo Gomes, Pedro Mano, Ricardo Tavares, Rodrigo Silva, Ana Cruz, Beatriz Gamboa and Teresa Miranda, without whom I could not have gotten through college. A special thanks to Rodrigo, who always made time to support me throughout this thesis. Even if they were not all named, my gratitude rests with all my friends who have been there for me.

All great people need a great family to support them. As such, my hard work would have been in vain if it were not for my mother, Isabel, and my sister, Catarina. Words will never be enough to describe how eternally thankful I am for all your sacrifices, patience and inspiration.

Finally, to make a human complete, there is a need for love. For that, I have my girlfriend Leonor to thank for. I will be forever in your debt for making me a better human, for all the the happiness you have brought to my life and, most importantly, for believing in me in my darkest hours.

UNIVERSIDADE DO PORTO

Abstract

Faculdade de Ciências da Universidade do Porto
Departamento de Física e Astronomia

MSc. Physics

S-matrix Bootstrap: Towards Inelasticity

by José PEREIRA

This thesis focuses on the principles that make up the S-matrix Bootstrap philosophy and their application to simple but instructive QFTs of massive neutral scalar particles. In addition, it explores the introduction of particle production in unitarity conditions, where several new results are obtained.

Firstly, we present an historical background of the S-matrix Bootstrap and of how its techniques developed. This is proceeded by an analysis of the main properties of the S-matrix, the central object of study, with special emphasis on Analiticity, Crossing symmetry and Unitarity, following [1, 2]. Then, we move on to Dispersion Relations and, finally, to the Partial-wave expansion, essential for the Bootstrap of higher dimensions QFTs.

In the second chapter, which follows [3], we start by studying massive neutral scalar fields in two-dimensional Lorentzian space, where the two main approaches to the Bootstrap, the primal and the dual, are presented and extensively worked on. In the context of $2 \to 2$ collisions, the most general QFTs whose mass spectrum assumes a bound state is studied. Using the previously mentioned techniques, the cubic coupling of the lighter masses to the bound state is maximized, which, combined with a given analytic structure, eventually leads to the sine-Gordon S-matrix. Moreover, we obtain the space of allowed theories which admit two and even three bound states. Finally, other quantities are maximized in the absence of a cubic coupling, and then the dual method is applied.

Subsequently, we proceed with the same optimization scheme for higher dimensions, in particular in 4D. In addition to maximizing the cubic coupling, another historically relevant quantity, the effective quartic coupling, is analysed.

Before presenting the conclusions, we move to the main chapter of the thesis: the implementation of particle production in the maximization of chosen physical observables. As before, we start by analysing QFTs in two dimensions, where the cubic coupling is yet again maximized. However, particle production is introduced as a special constraint, which yields new interesting results. Some modifications to the usual Ansatz are suggested, so as to improve said results. Finally, this is carried out in higher dimensions, where the SDPB [4] program is the main technical tool to solving all the problems. As such, generalizations of the previous constraints are introduced, whether directly on the S-matrix partial-waves or on the imaginary part of the amplitude in the forward limit, via the optical theorem.

Finally, an overview of the thesis is given, as well as future directions and open problems which this work generates.

In the appendices, several derivations and generalizations are presented, so as to make the rest of the thesis easier to follow.

UNIVERSIDADE DO PORTO

Resumo

Faculdade de Ciências da Universidade do Porto
Departamento de Física e Astronomia

Mestrado em Física

S-matrix Bootstrap

por José PEREIRA

Esta tese foca-se nos princícpios que estableceram a filosofia do "S-matrix Bootstrap"e na sua aplicação a casos simples e pedagógicos de teorias quânticas de campo (TQCs) massivas, escalares e sem carga. Para além disso, exploramos a introdução de inelasticidade nas condições de unitariedade, obtendo, assim, novos resultados.

Numa primeira fase, fazemos uma introdução histórica, que visa expôr o surgimento e o desenvolvimento da técnica de "S-matrix Bootstrap". Segue-se uma análise das principais características da "S-matrix", o objeto principal de estudo, com ênfase nas propriedades de Analiticidade, "Crossing symmetry"e Unitariedade, seguindo de perto [1, 2]. Por fim, prosseguimos com o assunto de relações de dispersão e, finalmente, a expansão em ondas parciais, essencial para o método de "Bootstrap"em TQCs de maiores dimensões.

No segundo capítulo, que segue [3], começamos por estudar campos massivos, escalares e sem carga num espaço Lorentziano dois-dimensional, introduzindo assim as duas principais abordagens ao "Bootstrap", o "primal"e o "dual", extensivamente estudadas. No contexto de colisão de $2 \to 2$, consideramos a TQC mais geral cujo espectro de massa assume um estado ligado. Usando as técnicas previamente indicadas, o acoplamento cúbico das massas mais leves ao estado ligado é maximizado, o que, combinado com uma estrutura analítica bem especificada, eventualmente dá origem à solução da "S-matrix"de "sine-Gordon". Para além disso, obtemos o espaço de teorias permitidas que assumem dois ou mais estados ligados. Por fim, outras quantidades são maximizadas na ausência do acoplamento cúbico, e, depois, o método "dual"é aplicado.

De seguida, procedemos com o mesmo esquema de otimização em maiores dimensões, em particular em quatro dimensões. Não só maximizamos o acoplamento cúbico como

também introduzimos outra quantidade física historicamente relevante, o acoplamento quártico, que é de igual modo analisado.

Antes de apresentarmos as conclusões, seguimos para o capítulo de maior relevo na tese: a implementação da produção de partículas na maximização de observáveis físicas. Tal como antes, começamos por analisar as TQCs em duas dimensões, onde se maximiza o acoplamento cúbico. No entanto, introduz-se a produção de partículas como uma condição adicional, que dá origem a resultados novos e interessantes. Algumas modificações ao "Ansatz"são sugeridas, de modo a melhorar os resultados. Finalmente, efetuamos este processo para maiores dimensões, onde o programa SDPB [4] é a peça principal na resolução dos problemas de otimização. Como tal, foram introduzidas generalizações às condições previamente utilizadas, quer diretamente nas ondas parciais da "S-matrix"ou na parte imaginária da amplitude no limite de colisão frontal, via teorema ótico.

Por fim, fazemos um resumo dos principais resultados da tese e discutimos eventuais direções a tomar.

Nos apêndices, encontram-se as demonstrações e generalizações utilizadas, apresentadas de modo que o leitor consiga seguir mais facilmente a tese.

Contents

List of Figures

List of Tables

Glossary

CDD	Castillejo-Dalitz-Dyson
LHS	Left Hand Side
PSD	Positive Semidefinite
QCD	Quantum Chromodynamics
QFT	Quantum Field Theory
RHS	Right Hand Side

Chapter 1

Introduction to S-matrix Bootstrap

1.1 Historical background

Around the 1930s and 1940s, quantum field theory, QFT, had been plagued by a plethora of technical and experimental issues [5, 6]. Whereas many individuals such as Stueckelberg, Feynman and Tomonaga focused on improving such QFTs [6], Heisenberg was motivated to find a theory based on concepts which would not be affected by eventual developments in the theory of elementary particles [6], hence reintroducing a previously studied object by John Wheeler [7] named the *S-matrix*.

In particular, there was an attempt to describe the strong interaction which, at the time, had not been possible with QFT [6]. With the advent of the S-matrix came the *bootstrap* program, which consisted in solving a determined theory based on self-consistent conditions [5, 8], and which proved useful in regards to the previous issue. The S-matrix bootstrap became the relevant technique which was highly developed throughout those years. However, this approach posed many mathematical challenges, which later led to its abandonment [5]. The main contributor was the fact that, between the 1970s and 1980s, there had been some developments in the quantum field theory community, namely the adoption of the quantum chromodynamics (QCD) approach [5].

Eventually, the S-matrix formalism gave rise to the duality program, which also had some connection to the Regge program [5]. In studying this subject, Veneziano proposed an analytical model, in 1968, featuring what became known as the Veneziano amplitude, which became the basis for a workable bootstrap program [9]. This marked the beginning of String Theory.

The S-matrix topic remained practically dormant until the revival of conformal bootstrap [10]. Recent developments in technology, together with newer formulations, make the bootstrap approach - S-matrix bootstrap in this context - more relevant than ever. So as to understand how S-matrix bootstrap is done nowadays, we start by reviewing the literature on the S-matrix and its properties.

1.2 S-matrix properties

In view of the historical importance of the S-matrix, it is relevant to understand in what principles it is based on. The key points necessary for the remainder of the dissertation are *Analyticity*, *Crossing-symmetry* and *Unitarity*. Some formulations also require knowledge about *Dispersion relations* and *Partial-wave expansion*, which will be briefly discussed. There are a multitude of properties which will not be explored, as there are complete textbooks dedicated to that matter. In case there are relevant topics - but not necessary to follow this thesis - the appropriate literature will be referenced.

The main references used in this introductions are [1, 2, 8, 11].

1.2.1 Analyticity, Crossing-symmetry and Unitarity

In the present context, the S-matrix will be used to describe the scattering of particles. So as to build a tool consistent with physical observations and considerations, the S-matrix must satisfy the following properties [1]:

1. The superposition principle of quantum mechanics: if $|\psi_a\rangle$ and $|\psi_b\rangle$ are physical states, then so is $|\psi_c\rangle = a|\psi_a\rangle + b|\psi_b\rangle$, $a, b \in \mathbb{C}$;

2. The short-range character of the interaction: it is known from nuclear physics that the strong force has a range shorter than 10^{-15} m [11];

3. Conservation of probability (regarding transitions);

4. The requirements from Special Relativity. In particular, the S-matrix must be invariant under Lorentz transformations;

5. Causality and the existence of macroscopic time.

Due to requirement (2), both the initial and the final states (asymptotically in the past and future, respectively) are composed exclusively of free particles, and hence the Hilbert space is the Fock space of free particles [8].

Physically speaking, (5) is one of the most important requirements in the list. However, its mathematical consequences are hard to derive, and as such it is often relaxed to the condition that causality requires the transition amplitudes to be real-boundary valued functions of more general functions of complex variables [1]. Thus, (5) is replaced by

- Transition amplitudes are the boundary values of analytical functions in the real axis.

In [1], section 1.1, it is shown the connection between this requirement and causality, using a simple example of the scattering of a wave packet.

With these fundamental features in mind, we focus on the mathematical aspect of the matter. The initial and final states (states of free particles) will be labelled by discrete symbols, even though they correspond to continuous states of momenta, spins and other quantum numbers. In this setting, we can define the scattering operator [11], $\hat{S}$, such that the probability of transitioning from state $|i\rangle$ to $|f\rangle$ is given by

$$P_{fi} = \left|\langle f|\hat{S}|i\rangle\right|^2 \tag{1.1}$$

Let $|m\rangle$, $m = 1, 2, ...$ be a basis of complete, normalized and orthogonal states,

$$\langle m|n\rangle = \delta_{m,n}, \quad \sum_m |m\rangle\langle m| = 1. \tag{1.2}$$

Since probability is conserved (condition (3)), for an arbitrary normalized initial state $|i\rangle = \sum_m a_m|m\rangle$ and $|f\rangle = |n\rangle$, Equation 1.1 implies that

$$\begin{aligned} 1 &= \sum_f \left|\langle f|\hat{S}|i\rangle\right|^2 \\ &= \sum_{n,m,m'} a_m^* a_{m'} \langle m|\hat{S}^\dagger|n\rangle\langle n|\hat{S}|m'\rangle \\ &= \sum_{m,m'} a_m^* a_{m'} \langle m|\hat{S}^\dagger\hat{S}|m'\rangle \end{aligned} \tag{1.3}$$

where $\hat{S}^\dagger$ is the hermitian conjugate of the operator $\hat{S}$. Since the initial state is normalized, $\sum_m |a_m|^2 = 1$. For the above equation to hold for any coefficient a_m, it is necessary that $\langle m|\hat{S}^\dagger\hat{S}|m'\rangle$, or rather $\hat{S}^\dagger\hat{S}$, be the identity operator,

$$\hat{S}^\dagger\hat{S} = \hat{1}. \tag{1.4}$$

Doing the same for an arbitrary final state, we come to the conclusion that

$$\hat{S}\hat{S}^\dagger = \hat{1}. \tag{1.5}$$

which means $\hat{S}$ is a **unitary** operator.

As a consequence of Lorentz invariance, in the case of spinless particles it is required that the matrix element $\langle m|\hat{S}|n\rangle$ be independent of the chosen Lorentz frame. Let $p = (E_{\vec{p}}, \vec{p})$ be the four-momenta of a single particle of mass m, with energy $E_{\vec{p}} = \sqrt{m^2 + \vec{p}^2}$ ((+,-,-,-) signature, and admit that the space of states consists in an n-particle Fock space, where each particle is defined by its momentum, $|p_1, p_2, ..., p_n\rangle$. For $2 \to 2$ scattering, $\langle p_3, p_4|\hat{S}|p_1, p_2\rangle$ can be written as a function of the *Mandelstam invariants* s, t and u

$$s = (p_1 + p_2)^2, \quad t = (p_1 - p_3)^2, \quad u = (p_1 - p_4)^2 \tag{1.6}$$

which means that $s + t + u = 4m^2$.

In any scattering process, particles being collided can either interact or not. So as to capture this behaviour, it is usual to write [1, 11]

$$\hat{S} = \hat{1} + i\hat{T} \tag{1.7}$$

where $\hat{T}$ is the amplitude operator and contains all the information for processes where particles collide. In terms of this operator, the unitarity condition reads

$$\hat{T} - \hat{T}^\dagger = i\hat{T}^\dagger\hat{T} = i\hat{T}\hat{T}^\dagger \tag{1.8}$$

For $2 \to 2$ scattering,

$$\langle p_3, p_4|\hat{T}|p_1, p_2\rangle - \langle p_3, p_4|\hat{T}^\dagger|p_1, p_2\rangle = i\langle p_3, p_4|\hat{T}^\dagger\hat{T}|p_1, p_2\rangle = i\langle p_3, p_4|\hat{T}\hat{T}^\dagger|p_1, p_2\rangle \tag{1.9}$$

Using Lorentz symmetry, the previous equation can be written as [1]

$$\begin{aligned} 2\,\mathrm{Im}\,\langle p_3, p_4|\hat{T}|p_1, p_2\rangle &= \sum_n \langle n|\hat{T}|p_3, p_4\rangle^* \langle n|\hat{T}|p_1, p_2\rangle \\ &= \sum_n \langle p_3, p_4|\hat{T}|n\rangle \langle p_1, p_2|\hat{T}|n\rangle^* \end{aligned} \tag{1.10}$$

where $|n\rangle$ correspond to intermediate states allowed by conservation of energy and momentum. In case $n > 2$, then $|p_1, ..., p_n\rangle$ is a state with more than 2 particles: if there is enough energy, such states become available, which introduces particle production. The energy at which particle production becomes possible is known as the *inelastic threshold*.

For total energies below this threshold, Equation 1.10 can be written as [1]

$$\begin{aligned} 2\,\mathrm{Im}\,\langle p_3, p_4|T|p_1, p_2\rangle = (2\pi)^{-2} \int d^4k_1 d^4k_2\, \delta^{(+)}(k_1^2 - m^2)\delta^{(+)}(k_2^2 - m^2) \\ \times\, \delta^{(4)}(p_1 + p_2 - k_1 - k_2)\langle p_3, p4|T|k_1, k_2\rangle \\ \times\, \langle p_1, p_2|T|k_1, k_2\rangle^* \end{aligned} \tag{1.11}$$

where the appropriate conventions [1] have been taken and T is the amplitude, related to the amplitude operator $\hat{T}$ by

$$\langle p_3, p_4|\hat{T}|p_1, p_2\rangle = (2\pi)^4\delta^{(4)}(p_1 + p_2 - p_3 - p_4)\, T \tag{1.12}$$

The main takeaway is the following: when relaxing Equation 1.11 so as to include states above the inelastic threshold, new terms, related to new particle states, must be added in the RHS. However, that means a sudden change in the LHS of the same equation, at the precise location where energy allows for new states: a discontinuity is encountered. This analysis is true at each energy allowing for the production of higher particles states, which introduces a multitude of similar singularities at each energy threshold.

Up until now, T is being considered as a function of the invariant variable s defined in 1.6, and t remains fixed (for now, assuming 4D space). The aforementioned singular points can be shown to be *branch-points* [1], which introduce cuts starting at said points $s \in \{4m^2, 9m^2, 16m^2, ...\}$ (where m is the mass of the colliding particles), running along the real axis. These points are called *normal thresholds*, where $s = 4m^2$ is the lowest threshold which corresponds to the two-particles state. Mathematically, *branch-cuts* isolate what are called *Riemann surfaces*, in which the amplitude must be single valued. By convention, the first sheet of these Riemann surfaces is named the *physical sheet*, where the physical scattering amplitude is just the boundary value of the complex function T at the real axis. Other sheets can be accessed by crossing a branch-cut: we name them *unphysical sheets*, and they are of little importance for this thesis.

Nonetheless, cuts are not the only singular structures in theories. Physically, it is possible that the two-particle state gives rise to one-particle state [1]. It can be shown that such case indeed exists and corresponds to the unphysical value*). Moreover, it can be shown (using either unitarity and causality or perturbation theory) that such singularity

*The minimum physical energy associated with two particle scattering is $s = 4m^2$. Lower energies than the previous value are, therefore, unphysical.

corresponds to a *pole*, instead of a branch-cut [1, 11]. These poles correspond to *bound-states* of the theory. For the purposes of this dissertation, both poles and branch-cuts are the sole singularities admitted in the S-matrix theory.

With this in mind, we can proceed with several considerations. For two particle scattering, the elastic T is a function of Lorentz invariants, s, t and u (cf. Equation 1.6). However, in 4D (the usual case), T is function of only two independent variables, s and t [1],

$$\langle p_3, p_4|\hat{T}|p_1, p_2\rangle = (2\pi)^4\delta^{(4)}(p_1 + p_2 - p_3 - p_4)\, T(s, t) \tag{1.13}$$

So as to mathematically describe what the physical amplitude should be like, we must decide which side of the branch-cut to choose, before taking the limit towards the real line. According to perturbation theory [1, 2, 11], physical amplitudes are given by the limit

$$T(s, t) = \lim_{\epsilon\to 0} T(s + i\epsilon, t) \tag{1.14}$$

where $s > 4m^2$ and $t, u < 0$ are considered to be real variables. This is the result of taking the so-called $i\epsilon$*-prescription* [1], developed by Feynman. Equation 1.14 is the starting point to considering the rest of the analyticity results we will discuss. Before discussing such results, there is another useful feature we must consider, often called **Real analyticity** or **Hermitian analyticity**, which consist in the fact that

$$T(s^*, t^*) = T^*(s, t) \tag{1.15}$$

which can be obtained using the Schwarz reflection principle [1, 11], for instance, or within axiomatic QFT in [12].

Regarding **analyticity**, we chose to mainly follow [2] rather than usual textbooks [1, 11], since all the sequential developments are better condensed rather than spread across several chapters. In view of this, we simply reiterate the conclusions of said paper. These results concern neutral scalar particles.

Firstly, it has been shown [13, 14] that, for the $\pi^0\pi^0 \to \pi^0\pi^0$ case (which are neutral scalar particles), $T(s, t)$ is an analytic function of s with cuts for $s > 4m^2$ and $u > 4m^2$, for $-28m^2 < t \leq 0$, in the s-channel.

Secondly, progress has been made regarding the analytic properties of $T(s, t)$ for complex t and fixed energy $s > 4m^2$, thanks to Lehmann [15]. Lehmann was able to prove that $T(s, \cos\theta)$ is analytic inside an ellipse, the *small Lehman ellipse*, with foci at $\cos\theta = \pm 1$

and semi-major axis $\cos\theta_{\text{sL}} > 1$ - whose exact value is greatly dependent on the theory, energy, mass of the particles, to name a few. Moreover, he showed as well that the $\text{Disc}_s T(s, \cos\theta)$ is analytic for a larger ellipse, the *large Lehmann ellipse*, with a semi-major axis $\cos\theta_{LL} = 2\cos^2\theta_{sL} - 1$.

For s and t simultaneously complex, Bros, Epstein and Glaser proved that there is a region around any $(s, \cos\theta)$ point where $T(s,t)$ is analytical [16].

Finally, A. Martin was able to demonstrate that $T(s,t)$ is analytic for $|t| < R$ and the s plane with the cut [17]. For the scattering of similar particles, $R = 4m^2$ [2].

In practice, an extended notion of analyticity will be considered, *extended analyticity*, which is not yet rigorously proven but seems consistent with some results [2]. Extended analyticity is the belief that the amplitude $T(s,t)$ is an analytical function of the variables, s and t, except for some pole singularities in the region $s \in [0, 4m^2]$ and a cut starting at $s = 4m^2$, as well as the image of said singularities under crossing. These are the sole singularities imposed by unitarity.

The last missing piece is **crossing-symmetry**. In this regard, using the *LSZ* reduction formula it has been shown in QFT [18], for $2 \to 2$ scattering, that

$$T(s,t) = T(t,s) = T(u,t) \tag{1.16}$$

As such, there is only one important complex function, the amplitude, which describes the scattering in different channels by taking the appropriate limits and bounds.

For a more elaborate reading about the S-matrix properties, some textbooks such as the ones referenced already ([1, 11]) are suggested.

1.2.2 Dispersion relations

Other useful tools in the S-matrix toolkit are the **dispersion relations**, which consist in the representation of the S-matrix/amplitude in terms of the Cauchy's integral formula [11]. To that matter, we fix the spectrum so as to include one bound-state (and its image under crossing). Let us choose a contour γ such as the one represented in Figure 1.1, inside which $T(s,t)$, for fixed u, must be an analytic function. According to Cauchy's integral formula (any dependence on other variables apart from s are omitted)

$$T(s) = \frac{1}{2\pi i} \oint_\gamma ds' \, \frac{T(s')}{s' - s} \tag{1.17}$$

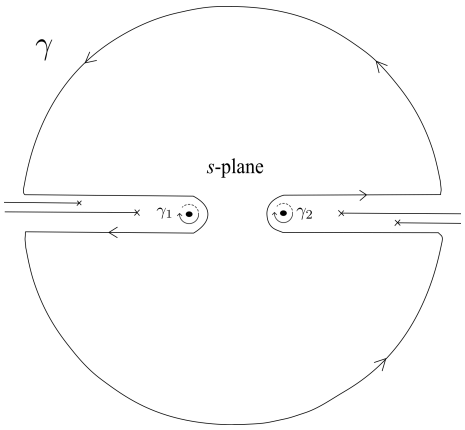

FIGURE 1.1: Integration contour γ of Equation 1.17 in the s-plane. The dark points correspond to a bound-state in the s-channel and its image under crossing- symmetry. The lines running to the left and right correspond to the branch-cuts starting at the normal thresholds, in the s-channel (right) and in the t-channel (left).

Let us assume that $T(s)$ decays fast enough in the infinity, i.e. $T(s) \to 0$, $|s| \to \infty$. It does not have to be the case: if the function is polynomially bounded in s^n, one must introduce *subtractions*. In most cases in this dissertation this shall not be needed, which is why we do not further develop the topic (see [1, 11]). Thus, when blowing up the contour from Figure 1.1, the arcs will tend do 0 as the contour approaches infinity. We are just left with the segments on either side of the branch cuts and smaller contours around each pole (which we denote by γ_1 and γ_2). Mathematically,

$$T(s) = \frac{1}{2\pi i}\left[-\oint_{\gamma_1} - \oint_{\gamma_2}\right] ds' \, \frac{T(s')}{s'-s} + \frac{1}{2\pi i}\int_{-u_0}^{\infty} ds' \, \frac{T_t(s')}{s'-s} + \frac{1}{2\pi i}\int_{4m^2}^{\infty} ds' \, \frac{T_s(s')}{s'-s} \tag{1.18}$$

where T_s and T_t are the discontinuities of $T(s)$ across the cuts in the s-channel and t-channel, respectively. The minus sign in the integrals around the poles account for the fact that, originally, γ_1 and γ_2 are contours in the clockwise direction. These integrals can be simplified using the *Residue Theorem*, which gives

$$\begin{aligned} \frac{1}{2\pi i}\left[-\oint_{\gamma_1} - \oint_{\gamma_2}\right] ds' \, \frac{T(s')}{s'-s} &= -\left[\text{Res}\, \frac{T(s')}{s'-s}\bigg|_{s'=4m^2-m_1^2-u_0} + \text{Res}\, \frac{T(s')}{s'-s}\bigg|_{s'=m_1^2}\right] \\ &\equiv -\frac{g_t^2}{s-(4m^2-m_1^2-u_0)} - \frac{g_s^2}{s-m_1^2} \end{aligned} \tag{1.19}$$

where, by definition, $g_t^2 \equiv -\operatorname{Res} T(s')\big|_{s'=4m^2-m_1^2-u_0}$ and $g_s^2 \equiv -\operatorname{Res} T(s')\big|_{s'=m_1^2}$. Thus, Equation 1.17 reads

$$\begin{aligned} T(s) &= -\frac{g_t^2}{s-(4m^2-m_1^2-u_0)} - \frac{g_s^2}{s-m_1^2} + \frac{1}{2\pi i}\int_{-u_0}^{\infty} ds' \frac{T_t(s')}{s'-s} + \frac{1}{2\pi i}\int_{4m^2}^{\infty} ds' \frac{T_s(s')}{s'-s} \\ &= -\frac{g_t^2}{t(s)-m_1^2} - \frac{g_s^2}{s-m_1^2} + \frac{1}{2\pi i}\int_{-u_0}^{\infty} ds' \frac{T_t(s')}{s'-s} + \frac{1}{2\pi i}\int_{4m^2}^{\infty} ds' \frac{T_s(s')}{s'-s} \end{aligned} \tag{1.20}$$

This is the final form of the dispersion relation. Further simplifications can (and will) be made. For a more elaborate derivation of such results, consult Appendix A.

Another known dispersion relation is the one proposed by Mandelstam, where, instead of using just the one discontinuity, double discontinuities are considered. The advantage is that it is generalized for all s, t and u, but requires more careful treatment. For a more detailed discussion, check [1].

1.2.3 Partial-wave expansion

The unitarity condition, as was introduced in subsection 1.2.1, is of quadratic form. In some cases, like in higher dimensions (cfe. Chapter 3), it attains a complicated form which is not always easily solvable. To circumvent this problem, it is often required to diagonalize the expressions. To do so, we must look for the natural eigenbasis: this is where the partial-wave expansion shines the most. All of the following results can be found in [2, 19].

Let us consider the scattering in $d+1$ spacetime dimensions, and center our attention in the $2 \to 2$ scattering of two identical real scalar massive particles of mass m - the lightest in the theory. Any $2 \to 2$ S-matrix element can be written as

$$\langle p_3, p_4|\hat{S}|p_1, p_2\rangle = \mathbb{1} + i(2\pi)^{d+1}\delta^{(d+1)}(p_1+p_2-p_3-p_4)T(s,t,u) \tag{1.21}$$

with

$$\mathbb{1} = (2\pi)^{2d} 4E_{\boldsymbol{p}_1}E_{\boldsymbol{p}_2}\left\{\delta^{(d)}(\boldsymbol{p}_1-\boldsymbol{p}_3)\delta^{(d)}(\boldsymbol{p}_2-\boldsymbol{p}_4) - (3 \leftrightarrow 4)\right\} \tag{1.22}$$

The channel under assumption is the s-channel, for which physical energies correspond to $s \geq 4m^2$, $t \leq 0$ and $u \leq 0$. As stated before, there are only two independent Mandelstam variables - s and t - meaning that $T(s,t,u) \equiv T(s,t,4-s-t)$ (which will often be referred

to as $T(s,t)$ by abuse of language). The scattering angle can be written as

$$x = \cos(\theta) = 1 + \frac{2t}{s-4} = -1 - \frac{2u}{s-4} \tag{1.23}$$

As is shown in [2], *Elastic Unitarity*, which is a regime in which energy allows only for the production of two particles, i.e. $4m^2 < s < 16m^2$, takes the form

$$2\,T_s(s,t) = \frac{1}{2}\int \frac{d^d\boldsymbol{q'}}{(2\pi)^d(2E_{\boldsymbol{q'}})}\int \frac{d^d\boldsymbol{q''}}{(2\pi)^d(2E_{\boldsymbol{q''}})}\,(2\pi)^{d+1}\delta^{(d+1)}(p_1+p_2-q'-q'')\times \\ \times\, T^{(+)}(s,t')T^{(-)}(s,t''), \tag{1.24}$$

where

$$T^{(\pm)} \equiv \lim_{\epsilon\to 0} T(s\pm i\epsilon, t), \qquad T_s(s,t) = \text{Disc}_s T(s,t) \equiv \frac{1}{2\pi}\left(T^{(+)}(s,t) - T^{(-)}(s,t)\right) \tag{1.25}$$

and $t' = -(p_1-q')^2$, $t'' = -(q''-p_4)^2$ (real analiticity was used). This intricate expression can be greatly simplified if the right change of basis is introduced - as one might have guessed, is the change of basis to that which transform in the irreducible representations of the SO$(1,d)$ group. The easiest route is to expand the amplitude $T(s,t)$ in terms of *partial-wave coefficients* $f_\ell(s)$

$$T(s,t) = \sum_{\ell=0}^{\infty} n_\ell^{(d)} f_\ell(s) P_\ell^{(d)}(\cos(\theta)) \tag{1.26}$$

where the sum runs over even ℓ (odd ℓ yield 0), $n_\ell^{(d+1)}$ are normalization factors

$$n_\ell^{(d)} = \frac{(4\pi)^{\frac{d+1}{2}}(d+2\ell-2)\Gamma(d+\ell-2)}{\pi\,\Gamma\left(\frac{d-1}{2}\right)\Gamma(\ell+1)} \tag{1.27}$$

and $P_\ell^{(d+1)}(\cos(\theta))$ are hypergeometric polynomials - the Legendre polynomials in $d+1$ dimensions. Following [2], one arrives at the simple expression

$$f_\ell(s) = \frac{\mathcal{N}_d}{2}\int_{-1}^{1} dx\,(1-x^2)^{\frac{d-3}{2}} P_\ell^{(d)}(x)\,T(s,t(x)) \tag{1.28}$$

where, by definition and Equation 1.23,

$$P_\ell^{(3)}(x) = P_\ell(x), \quad \mathcal{N}_d = \frac{(16\pi)^{\frac{1-d}{2}}}{\Gamma\left(\frac{d-1}{2}\right)}, \quad t(x) = \frac{1}{2}(s-4)(x-1) \tag{1.29}$$

and $P_\ell(x)$ are the Legendre polynomials normalized to $P_\ell(1) = 1$. In turn, we can use Equation 1.28 to write

$$\begin{aligned} S_\ell(s) &\equiv 1 + i\frac{(s-4)^{\frac{d-2}{2}}}{\sqrt{s}} f_\ell(s) \\ &= 1 + i\frac{(s-4)^{\frac{d-2}{2}}}{\sqrt{s}} \frac{\mathcal{N}_d}{2} \int_{-1}^{1} dx\, (1-x^2)^{\frac{d-3}{2}} P_\ell^{(d)}(x)\, T(s, t(x)) \end{aligned} \tag{1.30}$$

Since we treat the scattering of identical particles, Bose symmetry must apply. In turn, this implies that $S_\ell(s) = 1$ for odd ℓ: the integral is over a odd function, and therefore must be 0 - which explains why the partial-wave expansion in Equation 1.26 only admitted even ℓ.

To sum up, in the present context of scattering of massive scalar particles, the total angular momentum is conserved. As such, the natural basis for the expansion of the unitarity condition is that which has such quantities as eigenstates. Using this machinery, the bootstrap equations yield simpler expressions which only need to be evaluated for an array of s values, as well as ℓ.

Chapter 2

2D Scattering: massive scalar particles

2.1 Primal approach

2.1.1 Primal philosophy

The S-matrix bootstrap program can be carried out in a plethora of ways, depending on the given setup. There are two main approaches that have been widely considered: the *primal* and the *dual*. Each one of them has different advantages and mechanisms, which will be thoroughly discussed.

To first understand each formulation, one must recall that, so as to study strongly coupled field theories, one should look at S-matrices. Briefly, from the previous section:

- The mass spectrum is connected to the position of (pole) singularities in the S-matrix;
- The interaction strength between stable particles, i.e., couplings correspond to the magnitude of the residues at each singularity.

Intuitively, couplings should be bounded: for a fixed mass spectrum, increasing the interaction between the particles would result either in new bound-states or lower the mass enough to surpass that of the lightest particle, which violates spectral assumptions. Therefore, they comes as a natural quantity to put an upper bound on, as was done in [3].

With these remarks, the primal formulation can be better understood: it is a process in which one constructs a *feasible* scattering amplitude, i.e., consistent with a set of constraints and/or axioms like unitarity, crossing symmetry and analyticity, in addition to a specific mass spectrum. Given this spectrum and space of allowed amplitudes, one proceeds with optimizing a physical quantity such as the coupling.

As final remark, we note that the 2D case is particularly easier to bootstrap than in higher dimensions, due to the fact that no scattering angles exist and, as such, only one Mandelstam variable is independent. The work in the following subsections is inspired and based on [3].

2.1.2 Initial setup

So as to simplify the proceeding analysis, only the elastic $2 \to 2$ scattering S-matrix elements of a 2D relativistic quantum field theory will be considered; the scattering involves chargeless and identical particles of mass m. Furthermore, we assume that these are the lightest particles of the mass spectrum.

In two dimensions, there are yet other kinematical simplifications. Firstly, $u = 0$ for identical particles, which means s is the only independent Mandelstam invariant. According to Figure 2.1,

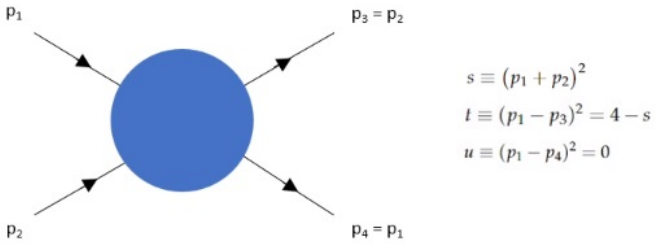

FIGURE 2.1: Time runs from left to right. In 2D, $u = 0$ which means s is the only independent Mandelstam variable ($m^2 = 1$). Therefore, $S(s,t,u) \overset{2D}{=} S(s)$.

Secondly, other simplifications arise due to the same support in the connected and disconnected parts. Let us consider the operator equation

$$\hat{S} = \hat{1} + i\,\hat{T} \tag{2.1}$$

After sandwiching the previous expression between two particles states,

$$\begin{aligned}\langle \mathrm{i}|\hat{S}|\mathrm{f}\rangle &= (2\pi)^2\, 4E_1E_2\left[\delta\left(\vec{p_1}-\vec{p_3}\right)\delta\left(\vec{p_2}-\vec{p_4}\right)+\vec{p_1}\longleftrightarrow\vec{p_3}\right]+i(2\pi)^2\delta^{(2)}\left(\vec{P}\right)T \\ &= 2\,(2\pi)^2\sqrt{s\left(s-4m^2\right)}\,\delta^{(2)}\left(\vec{P}\right)\times\left[1+i\frac{T(s)}{2\sqrt{s\left(s-4m^2\right)}}\right] \\ &\equiv \langle \mathrm{i}|\hat{1}|f\rangle\times S(s)\end{aligned} \tag{2.2}$$

where $\vec{P}\equiv\vec{p_1}+\vec{p_2}-\vec{p_3}-\vec{p_4}$ and

$$S(s)\equiv 1+i\frac{T(s)}{2\sqrt{s\left(s-4m^2\right)}}. \tag{2.3}$$

In what follows, $S(s)$ will be the main focus of our attention. In this setup, crossing symmetry translates to

$$S(s)=S(4m^2-s), \tag{2.4}$$

while unitarity states that, for physical energies [*],

$$\left|S(s)\right|^2\leq 1,\quad s\geq 4m^2. \tag{2.5}$$

Regarding the analytical structure, $S(s)$ admits cuts - a region for which there is particle production in the s/t-channel - or poles - where bound-states appear. Figure 2.2 summarizes these properties neatly.

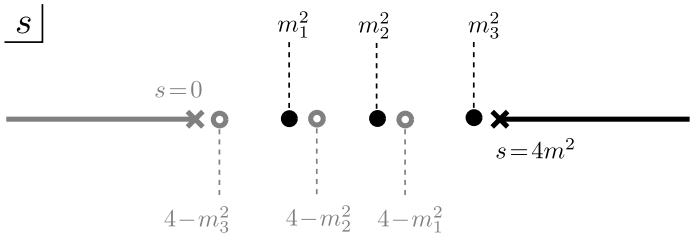

FIGURE 2.2: Analytical structure of $S(s)$ for the scattering of the lightest particles in the mass spectrum. The right s-channel cut starts at $s=4m^2$ (two-particle production) and runs to infinity; it represents the physical region where particle production is allowed. The other cut, the t-channel cut, is simply the crossing symmetric counterpart of the previous one, allowed by 2.4. bound-states are represented by poles in the region $s\in\,]0,4m^2[$, whether they are s- or t- channel poles (distinguished by the sign of the residue at each pole). Adapted from [3].

[*] $s+i\epsilon,\ s\geq 4m^2$

Our interest resides in studying the bound-states (b.s.) - resulting from single-particle outer states - which will be simply referred to as *particles*. Due to 2.4, these b.s. should come in pairs as

$$S(s) \simeq -J_i \times \frac{g_i^2}{s - m_i^2} \quad , \quad S(s) \simeq -J_i \times \frac{g_i^2}{4m^2 - s - m_i^2}, \qquad \left(J_i \equiv \frac{m^4}{2m_i\sqrt{4m^2 - m_i^2}} \right) \tag{2.6}$$

where the first is an s-pole and the second a t-pole. The J_i factor normalizes g_i^2 to be the residue in the matrix element T rather than S. Taking into account that g_i^2 should be positive for a unitarity theory, s-poles have negative residue while t-poles have positive residue.

These considerations allow for a simple setup, where the input is an arbitrary mass spectrum, the objective is "maximize the coupling to the lightest exchanged particle, g_1, compatible with such spectrum" and the result is an S-matrix which satisfies all the aforementioned axioms. Some final details:

- By definition, the mass spectrum $m_1 < m_2 < ... < m_N$ of N masses should satisfy $m_j < 2m$;
- m_1 might have the same value as m, depending whether $\mathbb{Z}_2$ symmetry is considered or not.

2.1.3 Numerical Ansatz via dispersion relations

Having all the analytical background brushed up, the next step is to proceed with numerical considerations. A natural step would be proposing an Ansatz for the $S(s)$ matrix element; however, our intuition is not yet prepared for such a big leap. The second best option is to make use of what is already known from previous sections, namely *dispersion relations*.

One starts with the Cauchy integral formula

$$S(s) - S_\infty = \oint_\gamma \frac{dx}{2\pi i} \frac{S(x) - S_\infty}{x - s}, \tag{2.7}$$

where γ is a closed anti-clockwise contour enclosing the s point, such that $S(s) - S_\infty$ is holomorphic inside and on it. Assuming that S_∞ is bounded by a constant at infinity - it need not be this way, in which case subtractions would have to be introduced - we can

blow up the contour to capture every singular behaviour of $S(s)$. Dropping the contribution of the line integral at infinity, only the poles and cuts are accounted for. This gives for a simple expression of the form

$$S(s) = S_\infty - \sum_i J_i \times \left(\frac{g_i^2}{s - m_i^2} + \frac{g_i^2}{4m^2 - s - m_i^2} \right) + \int_{4m^2}^{\infty} dx\, \rho(x) \left(\frac{1}{x - s} + \frac{1}{x - 4m^2 - s} \right), \tag{2.8}$$

where we have defined the distribution $\rho(x)$ as the discontinuity of the $S(s)$ element, $2\pi i\, \rho(s) \equiv S(s + i0^+) - S(s - i0^+)$. To obtain Equation 2.8 from Equation 2.7, one must write the discontinuity along the t-channel cut in terms of the s-channel one:

$$\begin{aligned}
(...) &= \int_{-\infty}^{0} dx\, \frac{S(x + i0^+) - S_\infty}{x - s} + \int_{0}^{-\infty} dx\, \frac{S(x - i0^+) - S_\infty}{x - s} \\
&= \int_{-\infty}^{0} dx \left[\frac{S(x + i0^+) - S_\infty}{x - s} - \frac{S(x - i0^+) - S_\infty}{x - s} \right] \\
&= \int_{-\infty}^{0} dx\, \frac{S(x + i0^+) - S(x - i0^+)}{x - s} \\
&\overset{x \to 4m^2 - x}{=} \int_{4m^2}^{\infty} dx\, \frac{S(4m^2 - x + i0^+) - S(4m^2 - x - i0^+)}{4m^2 - x - s} \\
&= \int_{4m^2}^{\infty} dx\, \frac{S\left(4m^2 - \left[x + i0^+\right]\right) - S\left(4m^2 - \left[x - i0^+\right]\right)}{x - 4m^2 + s} \\
&= \int_{4m^2}^{\infty} dx\, \frac{S(x + i0^+) - S(x - i0^+)}{x - 4m^2 + s}
\end{aligned} \tag{2.9}$$

where from next-to-last to the last step we used Equation 2.4. With this particular expression in mind, the maximization of the target variable g_1 comes down to an optimization problem in the space of variables $\{S_\infty, g_i^2, \rho(x)\}$.

In order to proceed with the optimization challenge, some numerical adaptations are needed: so as to take advantage of some numerical approaches, it is convenient to discretize the continuous distribution $\rho(x)$. To that end, $\rho(x)$ shall be evaluated in a grid of points $x_n \in [4, \infty[$ ($m^2 = 1$ from now on) such that it can be approximated by a linear spline connecting the points $(x_n, \rho(x_n) \equiv \rho_n)$, as is illustrated in Figure 2.3.

For example, for $x \in [x_n, x_{n+1}]$ the spline

$$\rho(x) \simeq \rho_n + (\rho_{n+1} - \rho_n) \times \left(\frac{x - x_n}{x_{n+1} - x_n} \right). \tag{2.10}$$

As it stands, this approximation does not yield a finite integral result, unless one assumes that it is only valid up to a cutoff, which we define as x_M. After said cutoff, the

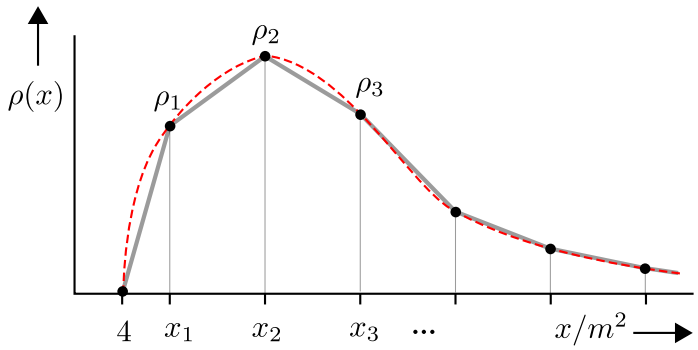

FIGURE 2.3: Example of the discretization of a generic distribution vs. its corresponding spline. The red dashed line represents some random distribution $\rho(x)$, while the grey represents the approximation taken by connecting the points from the discretization grid. Adapted from [3].

distribution is assumed to decay as $\rho(x) \sim 1/x$: for $x > x_M$, $\rho(x) \simeq \rho_M x_M/x$. After choosing a grid of points $\{x_0, x_1, ..., x_M\}$ such that $x_0 = 4$, the integrals in Equation 2.8 can be performed to yield the simple expression

$$S(s) \approx S_\infty - \sum_i J_i \times \left(\frac{g_i^2}{s - m_i^2} + \frac{g_i^2}{4 - s - m_i^2} \right) + \sum_{n=1}^{M} \rho_n K_n(s). \tag{2.11}$$

By standard integration procedures,

$$\begin{aligned} K_n(s) = &\left(\frac{s - x_{n-1}}{x_{n-1} - x_n} \right) \times \log(x_{n-1} - s) + \left(\frac{s - x_{n+1}}{x_n - x_{n+1}} \right) \times \log(x_{n+1} - s) \\ &- \frac{(x_{n-1} - x_{n+1})(s - x_n)}{(x_{n-1} - x_n)(x_n - x_{n+1})} \times \log(x_n - s) + (s \to 4 - s) \end{aligned} \tag{2.12}$$

with $n = 1, ..., M - 1$ while for $n = M$

$$\begin{aligned} K_M(s) = &\left(\frac{s - x_{M-1}}{x_{M-1} - x_M} \right) \times \log(x_{M-1} - s) - \frac{x_M}{s} \times \log(x_M) \\ &+ \frac{(x_{M-1} - x_M - s)(s - x_M)}{s(x_{M-1} - x_M)} \times \log(x_M - s) + 1 + (s \to 4 - s) \end{aligned} \tag{2.13}$$

In practice, Equation 2.11 needs to be evaluated, together with Equation 2.5, for some values of $s_0 > 4m^2$, which simply produces quadratic constraints in the aforestated space of variables. Thus, the space of solutions to the maximization problem must belong to the intersection of all the regions traced out by the constraints, for all $\{s_0\}$, simultaneously. The following step is implementing the developed machinery and obtaining some results.

2.1.4 Maximization of the cubic coupling with dispersion Ansatz

Most of the previous section was devoted to developing a numerical approach to the given optimization problem. Now, what is left is to apply it. For that purpose, a more

concrete optimization algorithm is needed. Fortunately, `Mathematica`'s built-in function `FindMaximum` can easily carry out the maximization problem: however, a set of constraints and an objective are needed. As for the objective, it is clear that one wished to maximize g_1^2; the constraint part will require a bit more work. According to the developed method, it is necessary to choose a grid where Equations 2.5 and 2.11 can be evaluated. As it turns out, the most convenient choice is to take $\{s_0\}$ as precisely the grid used in the discretization of $\rho(x)$, so as to make use of the identity

$$\text{Im } S(x_n + i0^+) = -\pi\rho_n \tag{2.14}$$

All in all, we get a set of M constraints

$$\left[S_\infty - \sum_i J_i \left(\frac{g_i^2}{x_m - m_i^2} + \frac{g_i^2}{4m^2 - x_m - m_i^2}\right) + \sum_{n=1}^{M} Re[K_n(x_m)]\rho_n\right]^2 + (\pi\rho_m)^2 \leq 1 \tag{2.15}$$

for $m = 1, ..., M$. Note that $\text{Re}\left[K_n(x_a)\right]$ can be easily computed using the substitution $\log(...) \to \log\left(\left|(...)\right|\right)$ where applicable.

To illustrate, let us consider the S-matrix with a bound-state (i.e., an s-channel pole) of mass m_1, coupled to the lightest mass of the spectrum, m, with coupling strength g_1^2. The result is in Figure 2.4.

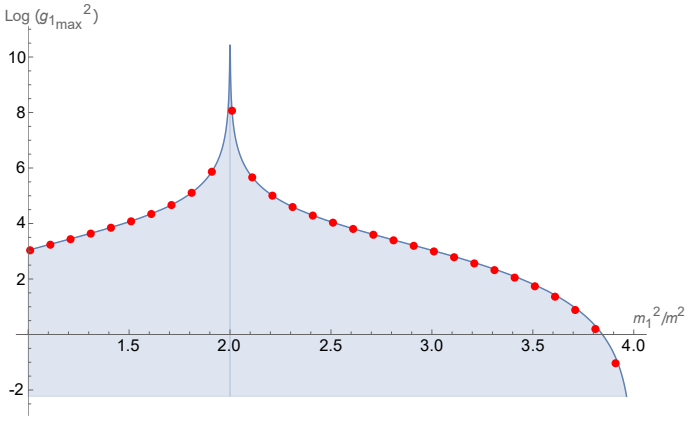

FIGURE 2.4: Result of maximizing the cubic coupling g_1^2 between masses m and m_1, for the S-matrix element of the scattering of two m particles with only one bound-state. In red, we present the numerical data; the curve which they rest upon is the residue of the sine-Gordon S-matrix element or its negative counterpart. The blue shaded region consists of the allowed space of solutions consistent with our assumptions.

In order to plot the preceding figure, an Ansatz with $M = 10$ was used; unitarity was imposed in a grid $s_i(n) = 4 + 100 \times \left(\frac{i}{n}\right)^4$, $i \in \{1, 2, ..., n\}$ [20] and $n = 200$ points. Such values yielded good results, as it is evident in Figure 2.5.

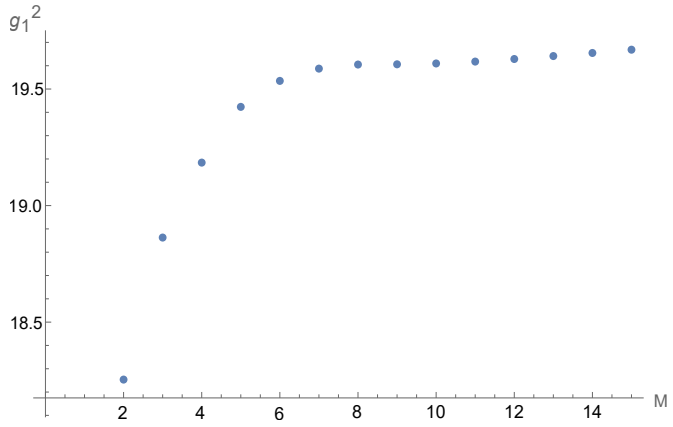

FIGURE 2.5: Convergence of g_1^2 vs. M. For $M = 10$, the objective has already attained its optimal value. For $M \geq 12$, the plateau is lost: numerical instability kicks in and n must be increased.

The most careful reader might have noticed that an analytical solution - the sine-Gordon S-matrix - was introduced for comparison, with no previous reason; this will become clearer in later subsections. Unfortunately, it was not possible to reproduce Figure 5 in [3], which presents the numerical S-matrix components versus the sine-Gordon S-matrix, since the components of the S-matrix had still not converged. This problem will be mitigated in upcoming subsections, when another Ansatz is developed.

In the meantime, some comments regarding the results are due. First and foremost, the most outstanding feature of Figure 2.4 is the fact that the numerical data seems to precisely coincide with the sine-Gordon S-matrix solution: this was not imposed a priori.

Secondly, a divergence stands out, for $m_1^2 = 2m^2$, with a rather simple explanation: when $m_1^2 = 2m^2$, the s-channel pole coincides with the t-channel pole; since they have the same "strength" but opposite sign (both decay as $\sim 1/s$), it results in mutual annihilation and the residue is left unbounded. Moreover, there seems to be a symmetry around $m_1^2 = 2m^2$, i.e, $g^2_{1_{max}}(m_1^2) = g^2_{1_{max}}(4m^2 - m_1^2)$: at the S-matrix expression level, choosing a solution for $m_1^2 > 2m^2$ amounts to multiplying the expression by -1, effectively changing what the s- and t- channel poles are. This is later corroborated by Figure 2.9.

Lastly, for weakly coupled particles (i.e., for $m_1 \approx 2m$), we expect the coupling magnitude to be small; this is what has been observed, since the logarithm tends to $-\infty$.

Even though the S-matrix element components have yet to stabilize, we can say with confidence that the data in Figure 2.4 has practically converged. Nonetheless, a striking

resemblance between these components and those of the *sine-Gordon* S-matrix [20–22],

$$S_{SG}(s) = \frac{\sqrt{s(4m^2 - s)} + \sqrt{m_1^2(4m^2 - m_1^2)}}{\sqrt{s(4m^2 - s)} - \sqrt{m_1^2(4m^2 - m_1^2)}}, \tag{2.16}$$

(where the same mass convention as above is used) became increasingly evident. It would be more reasonable and insightful to determine an Ansatz that performed better, however. In this spirit, a new numerical Ansatz may be introduced that solves the preceding convergence predicament.

2.1.5 Double ρ expansion: a new map, a new hope

The problem with using a spline is, among others, the fact that only an approximation to the real $\rho(x)$ distribution is being used. The discretization of a continuous distribution allows for some loss of precision; the accumulation of such errors can lead to noticeable discrepancies compared to the analytical case. Therefore, the previous method should be avoided.

Let us consider the same setup as previously: an S-matrix corresponding to $2 \to 2$ scattering of the lightest particles of the spectrum, m, which also allows for a bound-state of mass m_1. The coupling strength is g_1^2, which we try to maximize. To tackle this problem, we start with a useful change of variables [19, 20, 23] to the unit disk ρ_s

$$s \mapsto \rho_s = \frac{\sqrt{4m^2 - s_0} - \sqrt{4m^2 - s}}{\sqrt{4m^2 - s_0} + \sqrt{4m^2 - s}}, \qquad s = \frac{s_0(1 - \rho_s)^2 + 16m^2\rho_s}{(1 + \rho_s)^2} \tag{2.17}$$

where $s_0 < 4m^2$ is a free parameter indicating the centre of the map. This mapping can be better visualized in Figure 2.6. For convenience, we fix $s_0 = 2m^2$ so as to map the crossing symmetric point $s = t = 2m^2$ to the centre of the disk ρ_s.

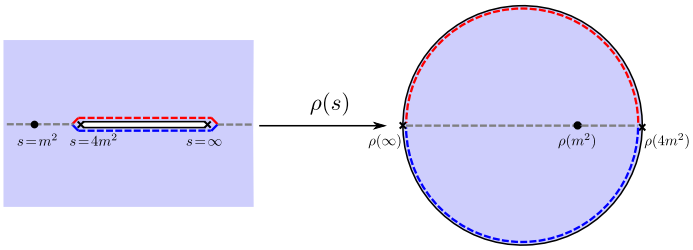

FIGURE 2.6: Illustration of the mapping 2.17. Adapted from [19].

The top and bottom parts of the cut are mapped to the top and bottom part of the disk; the region where poles appear, $s \in [0, 4m^2]$, is mapped to the region $\rho_s \in [2\sqrt{2} - 3, 1]$.

Regarding the S-matrix, the condition that its element must only depend on one independent Mandelstam variable, in 2D, is relaxed. Thus, $S(s)$ is thought of as a function of two (not actually) independent variables, s and t; in addition, it has a cut for $s > 4m^2$ and another for $t > 4m^2$, simultaneously, as well as s- and t-channel poles.

A useful feature of the ρ map is the fact that it maps to a unit disk: this means that any holomorphic function has a well-defined Taylor Expansion. Admitting that the analytical structure is as simple as considering two crossing symmetric poles and a mapping of the rest of the s-plane and t-plane, one can suggest an Ansatz for $S(\rho_s, \rho_t)$ [19], analytic for both ρ_s and ρ_t inside the disk,

$$S(s,t) = -J_\rho \times \left[\frac{g_\rho^2}{\rho(s) - \rho(m_1^2)} + \frac{g_\rho^2}{\rho(t) - \rho(m_1^2)}\right] + \sum_{a,b=0}^{\infty} c_{ab}\ \rho_s^a \rho_t^b \tag{2.18}$$

where $J_\rho = \frac{\sqrt{4m^2-m_1^2}\left(\sqrt{2m^2}+\sqrt{4m^2-m_1^2}\right)^2}{\sqrt{2}}$ accounts for the fact that g_ρ^2 is the amplitude coupling in the ρ variable. So as to be crossing symmetric, one must impose that c_{ab} be symmetric in its indexes, $c_{ab} = c_{ba}$; regarding further symmetries, it is now possible to impose the Mandelstam relation $s + t + u = 4m^2$ which, in the ρ variables, has the form

$$\rho_s + \rho_t + 4\rho_s\rho_t + \rho_s^2\rho_t + \rho_s\rho_t^2 = 0 \tag{2.19}$$

If $\rho(a,b) = \rho_s^a\rho_t^b + \rho_s^b\rho_t^a$ is a *symmetric polynomial*, then Equation 2.19 becomes

$$\rho(1,0) + \rho(1,1) + \rho(2,0) = 0 \tag{2.20}$$

The previous expression adds redundancy to Equation 2.18, which means many c_{ab} can be re-written as the sum of other coefficients: this amounts to set a particular set of constants to 0. To decide which coefficients get ruled out, one only needs to successively multiply the symmetrized expression 2.20 by other symmetric polynomials, which yields new conditions. A full set of terms which can be eliminated is illustrated in Figure 2.7:

Thus, we set a numerical cutoff for each coefficient, $a \leq M$ and $b \leq M$. Regarding unitarity, Equation 2.5 is evaluated in the same s-grid as was used in the previous section. Implementing the new Ansatz yields results which are illustrated in Figures 2.8 and 2.9. As anticipated, numerical data fit perfectly with the sine-Gordon S-matrix solution! However, contrary to preceding results, the numerical S-matrix components seem to converge exceptionally better with the new Ansatz 2.18. For these plots, unitarity was evaluated

*Only the number of terms which survive is considered, even though one could mix the order of the coefficients. In this case, the coefficients are ordered using `ReverseSort` in `Mathematica`.

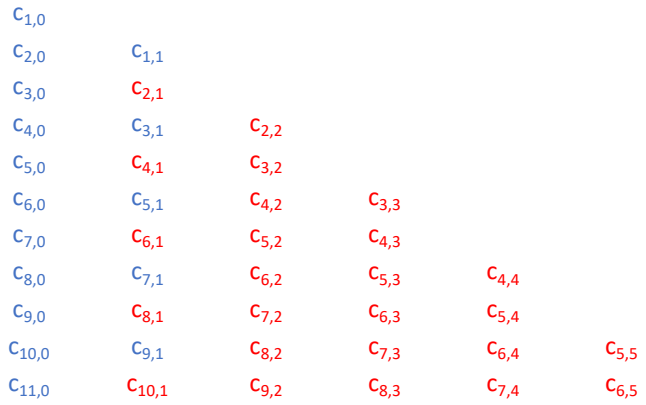

FIGURE 2.7: Independent coefficients (in blue) of 2.18. The coefficients in red are set to 0. At each level (N starts at 1), the number of terms which survive* is equal to the total number of symmetric polynomials in two variables, of degree N, minus the total number of constraints for each case, which is the total number of polynomials of degree $(N-3)$: $\left\lfloor \frac{N}{2} \right\rfloor - \left\lfloor \frac{N-3}{2} \right\rfloor$. Adapted from [19].

in an s-grid with $n = 100$ points and with $M = 5$. Other parameters can be used, but the presented ones achieve a good balance in terms of accuracy vs. numerical complexity. Figure 2.10 shows that, for $M = 5$, the primal objective has already converged.

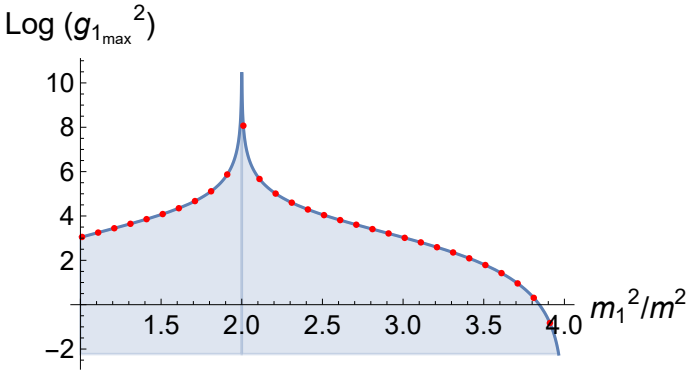

FIGURE 2.8: Result of maximizing g_ρ^2 (red dots) vs. the sine-Gordon S-matrix (blue curve). As in the previous method, the data beautifully agrees with the proposed curve.

According to Figure 2.9, the numerical solution seems to saturate unitarity for all $s > 4m^2$, which has immediate consequences. Using the conservation of probability for the $2 \to n$ scattering

$$\begin{aligned} 1 &= \sum_n \left|S_{2\to n}\right|^2, \quad s > 4m^2 \\ &= \left|S_{2\to 2}\right|^2 + \sum_{n>2} \left|S_{2\to n}\right|^2 \\ \Leftrightarrow \left|S_{2\to 2}(s)\right|^2 &= 1 - \sum_{n>2} \left|S_{2\to n}(s)\right|^2 \end{aligned} \tag{2.21}$$

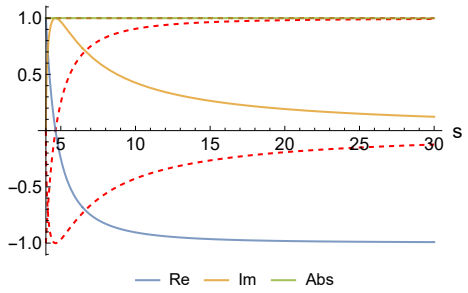

(A) $m_1 = m$.

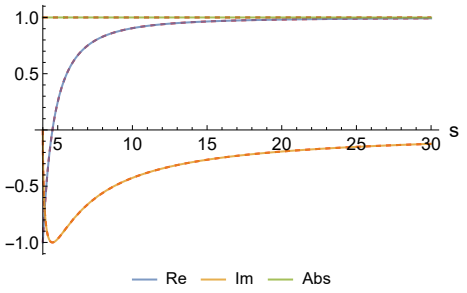

(B) $m_1 = \sqrt{3}m$.

FIGURE 2.9: Numerical S-matrix components for (A) $m_1 = m$ and (B) $m_1 = \sqrt{3}m$ vs. sine-Gordon. The red dashed lines are the Real, Imaginary parts and Absolute value of the sine-Gordon S-matrix. Whereas, in the first case, numerical data seem to suggest that the S-matrix which maximizes g_1 is $-S_{SG}$, in the second case that matrix is precisely S_{SG}.

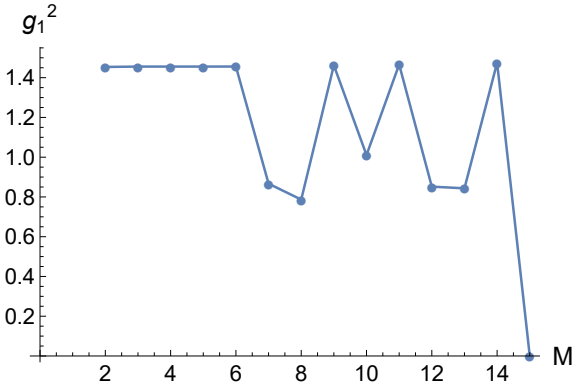

FIGURE 2.10: Convergence of g_1^2 with M for $m_1 = \sqrt{3}m$. For $M = 5$, it seems that the objective is already stable. For higher values of M, it seems that numerical instabilities kick in.

For this to happen, it is necessary that $\left|S_{2\to n}(s)\right|^2$ be 0: it is just the statement that there should not be particle production. The absence of particle production is closely related to *integrable models* [24, 25], in the context of integrable bootstrap theories. The important aspect is that such kind of theories feature S-matrices that can be obtained analytically: when $m_1 > \sqrt{2}m$, the S-matrix which saturates unitarity $\forall\, s > 4m^2$ and has a single s-channel pole at $s = m_1^2$ is the sine-Gordon S-matrix (which, in its original context, describes the scattering of the lightest *breathers* of the theory).

The upcoming subsection will give the final and definite proof of the connection between residue maximization and unitarity saturation for physical energies, which opens a new door for analytical solutions of S-matrices with more than one b.s..

2.1.6 CDD factors

In order to consider mass spectra with more than one bound-state, it is important to understand the underlying theory of the sine-Gordon S-matrix and its nature. As seen, previous solutions started to step into the realm of *unitary integrable* theories. Therefore, we should be able use part of, if not almost all, of developed theory therein to find analytic expressions for the maximal g_1^2 coupling of S-matrices with more than one bound-state.

To begin with, one changes variables from the Mandelstam variable s to the hyperbolic rapidity θ using the map $s = 4m^2\cosh^2(\theta/2)$. This mapping maps the entirety of the physical s-plane plus the cuts into a region called the *physical strip*, $\mathrm{Im}(\theta) \in [0, \pi]$, as is illustrated in Figure 2.11.

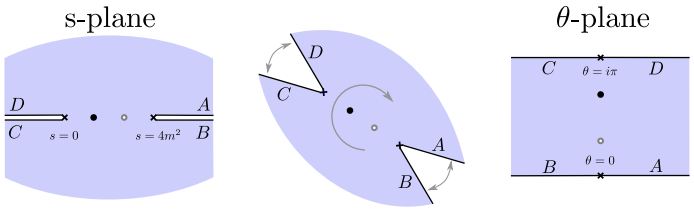

FIGURE 2.11: Map from the s-plane to the θ-plane. Adapted from [3].

In this variable, Equations 2.4 and 2.5 (crossing and unitarity, respectively) take the form

$$S(\theta) = S(i\pi - \theta), \quad S(\theta + i0^+)S(-\theta + i0^+) = f(\theta) \tag{2.22}$$

where $f(\theta) \in [0, 1]$, $\theta \in \mathbb{R}$ might encode some of the inelasticity (particle production). Following [3, 26],

$$S(\theta) = S_{CDD}(\theta) \times \exp\left(-\int_{-\infty}^{+\infty} \frac{d\theta'}{2\pi i} \frac{\log f(\theta')}{\sinh(\theta - \theta' + i0^+)}\right) \tag{2.23}$$

where $S_{CDD}(\theta)$ is the solution to 2.22 when $f(\theta) = 1$ while the exponential is known as the *minimal solution* (a particular solution) to 2.22. All the singular behaviour (poles) is condensed in the former.

As a side note, one is able to explain why the previous maximization process leads naturally to unitary S-matrices. Since $f(\theta)$ is an even function, the integral can be symmetrized to yield

$$S(it) = S_{CDD}(it) \times \exp\left(\int_{-\infty}^{+\infty} \frac{d\theta'}{2\pi} \frac{\sin(t)\cosh(\theta')}{\left|\sinh(it - \theta')\right|^2} \times \log f(\theta')\right) \tag{2.24}$$

where $t \in [0, \pi]$. Since $f(\theta') \leq 1 \implies \log f(\theta') \leq 0$ and $\frac{\sin(t)\cosh(\theta')}{|\sinh(it-\theta')|^2} \geq 0$ in $[0, \pi]$, we conclude that the minimal solution can only decrease with t; in order to maximize the potential value of $S(it)$, one must then choose $f(\theta) = 1$: this is precisely the statement that $|S(s)|^2$ must be 1. Hence, the previous argument must be true whatever form $S_{CDD}(\theta)$ might take. This argument proves why unitarity is to be expected when maximizing the residue of $S(s)$ and why it should hold up for any given number of b.s..

Up until now, we have only paid attention to the analytical part of the solutions. However, the real physics is at the singular region, where all the poles appear. In this spirit, the CDD term is introduced. It simultaneously solves

$$S_{\text{CDD}}(\theta) = S_{\text{CDD}}(i\pi - \theta), \quad S(\theta)_{\text{CDD}} S(-\theta)_{\text{CDD}} = 1 \tag{2.25}$$

as proposed. The solution to these equations is found to be the product of the so-called *CDD factors* [27],

$$S_{CDD}(\theta) = \pm \prod_j [\alpha_j], \quad [\alpha] = \frac{\sinh(\theta) + i\sinh(\alpha)}{\sinh(\theta) - i\sinh(\alpha)} \tag{2.26}$$

Depending on what value α takes, the CDD factor may be categorized as:

- **CDD-pole:** Re$[\alpha] \in [0, \pi]$. The CDD factor has a pole at $\theta = i\alpha$ in the physical strip (in the s-plane, $s \in [0, 4m^2]$). Due to locality constraints, $\alpha \in [0, \pi]$;
- **CDD-zero:** Re$[\alpha] \in [-\pi, 0]$. The CDD has a pole outside the physical strip (i.e., on another Riemann sheet other than the first). In this case, $\alpha \in [-\pi, 0]$ and the CDD factor has a zero at $\theta = -i\alpha$ inside the physical strip;
- **CDD-resonance:** Re$[\alpha] \in [-\pi, 0]$. α may be a complex number; however, its value must comply with the other axioms.

Relevant to our purposes are the first two CDD factors. In order to gain intuition, Figure 2.12 depicts some examples.

- **CDD-pole:** the factor changes sign at each pole (s- and t-channel poles). The tails are always negative;
- **CDD-zero:** the factor changes sign at each zero.

Given Figure 2.12, one might assume that the S-matrix which maximizes g_1 and is compatible with the mass spectrum $\{m_1/m, m_2/m, ...\}$ is merely given by the product

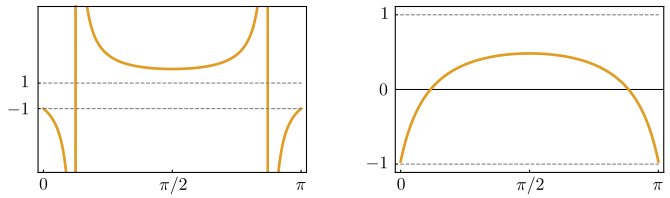

FIGURE 2.12: Difference between a (A) CDD-pole and a (B) CDD-zero. Both functions change signs at either (A) s-/t-channel pole or at (B) a zero. However, the amplitude of CDD-poles is always greater than 1, contrary to CDD-zeros. This will be important when constructing S-matrices from the product of CDD-factors. Adapted from [3].

of CDD-poles corresponding to each b.s.. However, this assumption is erroneous: one must not forget that the sign of a s-channel (t-channel) pole is negative (positive) in the s variable (in the θ variable, one can show* that it is actually the opposite); when taking the product of CDD-poles, this is not generally the case.

A solution to a generic mass spectrum can be obtained [19]. Nonetheless, it is rather cumbersome and serves us little purpose; for that reason, we decide to focus on the case of a two and three b.s. spectrum.

2.1.7 Two and three bound-states

As seen in section 2.1.5, the case of a single bound-state of mass $m_1 < 2m$ has solution $S(s) = \pm[\alpha_1]$, where α_1 is to be fixed by the relation $m_1^2 = 4m^2\cosh^2(i\alpha_1/2)$; the sign should be fixed later, in order to make the residue of the s-channel positive†.

The second case is that of a mass spectrum with two particles, $m_1 < m_2 < 2m$ and will be studied extensively; the optimization problem is that of maximizing the coupling pertaining to the process $m + m \to m_1$, i.e., g_1. According to the same logic as before, one expects four distinct regions, since both m_1 and m_2 can be greater or lesser then $\sqrt{2}m$‡:

- **Region A:** $m_1 < m_2 < \sqrt{2}m$;
- **Region B:** $m_1 < \sqrt{2}m < m_2$ (but $4m^2 - m_1^2 < m_2^2$);
- **Region C:** $m_1 < \sqrt{2}m < m_2$ (but $4m^2 - m_1^2 > m_2^2$);

*Near the s-channel pole, $S(s) \approx -J_i \frac{g_i^2}{s-m_i^2}$. Using the $s \mapsto \theta$ map and `Series` in `Mathematica` for θ near the corresponding $\theta_{m_i^2}$ value, $S(\theta) \approx +i\frac{\gamma^2}{\theta-\theta_{m_i^2}}$, where γ^2 is a real, positive number that depends on g_i^2 and J_i through some Jacobians. The same process applies to the t-channel pole.

†Henceforth, otherwise stated, the sign residue convention used is that of the θ variable.

‡According to Figures 2.8 and 2.9, this seems to be the most natural "inflection point" for the residue sign. Also corroborated by plots of the residue of the sine-Gordon vs. the position of the b.s..

- **Region D:** $\sqrt{2}m < m_1 < m_2$.

At first sight, it may seem rather confusing when considering these regions as they are, which is why Figure 2.13 may facilitate the analysis. We start by trying to guess the solution for Region B and C: intuitively, it should be rather easier since s- and t-channel poles alternate. Taking into account that the residue of s-channel poles has symmetric sign to that of t-channel ones (by definition) and making use of Figure 2.12 (A), one concludes that the solution is given by $S = \pm [\alpha_1] [\alpha_2]$. Regarding the overall sign, it must be fixed a posteriori*.

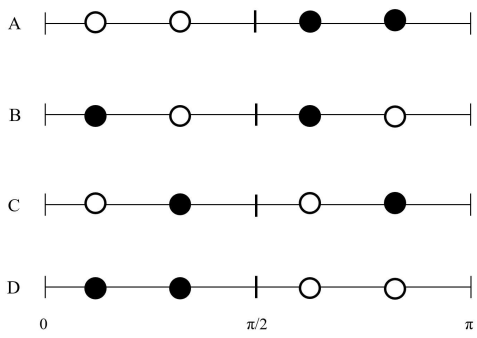

FIGURE 2.13: Position of the s- and t-channel poles for each of the masses m_1 and m_2 ($m_1 < m_2 < 2m$), according to the regions defined in subsection 2.1.7. Black (white) dots represent s-channel (t-channel) poles. The horizontal axis represents the value of α in the CDD-factor convention $[\alpha]$. Heavily adapted from [19].

Cases A and D are not so simple: s- and t-channel poles lie side by side, making it impossible for the residue to have the correct sign (CDD-poles alternate signs when passing through poles). As such, one must introduce a CDD-zero $[-\beta_1]$ between the s-channel poles $\alpha_2 < \beta_1 < \alpha_2$ (which, by crossing symmetry, has a t-channel CDD-zero between the two t-channel poles); the value of β_1, i.e., the position of the CDD-zero is fixed by the requirement that g_1^2 be maximum. According to Figure 2.14, this amounts to pushing β_1 as far away as possible from α_1, eventually colliding with α_2: this means that the bound-state m_1^2 is no longer coupled to the lightest particle. Thus, the optimal S-matrix must be $S = \pm [\alpha_1]$! Once more, the overall sign must be fixed a posteriori: for case A, one should include the sign (-1) - again, because of the tails of CDD-zeros; for D, that is no longer required. Hence, $S_A = -[\alpha_1]$ and $S_D = +[\alpha_1]$.

*According to [19], the sign of the residue closest to $i\pi$ has the form $(-1)^N \times$(positive), where N is the number of bound-states in the spectrum. If $N = 2$, for region B the closest pole is t-channel and thus one should include an overall sign (-1) (since the tails of both CDD-factors are negative, $(-1) \times (-1) \times (-1) = (-1)$, as intended). For C, it is the opposite.

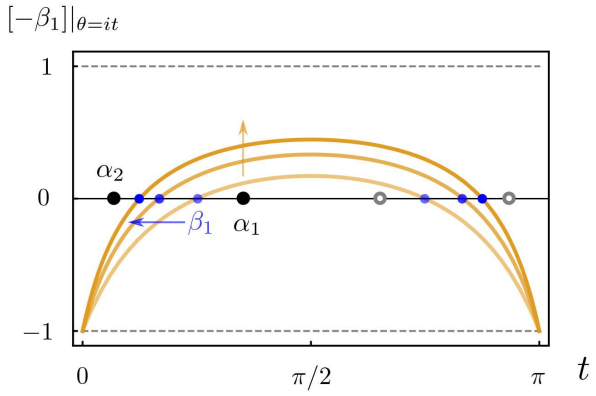

FIGURE 2.14: Amplitude of the CDD-zero $[-\beta_1]$ such that $\alpha_2 < \beta_1 < \alpha_2$. As we move β_1 successively closer to α_2, the amplitude of the CDD-zero increases. Then, in order to maximize the residue at $\theta = i\alpha_1$, one must push β_1 as far away as possible, colliding it with the CDD-pole $[\alpha_2]$. Adapted from [19].

When it comes to three b.s., the thought process is essentially the same, with the added difficulty of having to manage one more mass. In this case, we consider the simple example where m_1 has the same mass as the lightest particle, such that our bound-state spectrum is $\{m, m_2, m_3\}$ ($m_2 < m_3$). Apart from this, everything remains the same: the objective is still to maximize the coupling of m to $m_1 = m$. Since it is a bit cumbersome to derive each S-matrix, we proceed with enumerating each zone and the respective S-matrix:

- **Region A:** $m_2 < m_3 < \sqrt{2}m \longrightarrow S_A = -[\alpha_1]$;
- **Region B:** $m_2 < \sqrt{2}m < m_3$ (with $4m^2 - m_2^2 > m_3^2$) $\longrightarrow S_B = [\alpha_1][\alpha_3]$;
- **Region C:** $m_2 < \sqrt{2}m < m_3$ (with $4m^2 - m_2^2 < m_3^2$) $\longrightarrow S_C = -[\alpha_1][\alpha_2][\alpha_3]$;
- **Region D:** $\sqrt{2}m < m_2 < m_3 \longrightarrow S_D = [\alpha_1][\alpha_3]$;
- **Region E:** $m_2 < \sqrt{2}m < \sqrt{3}m < m_3 \longrightarrow S_E = -[\alpha_1][\alpha_3]$;
- **Region F:** $\sqrt{2}m < m_2 < \sqrt{3}m < m_3 \longrightarrow S_F = [\alpha_1][\alpha_2][\alpha_3]$;
- **Region G:** $\sqrt{3}m < m_2 < m_3 \longrightarrow S_G = -[\alpha_1][\alpha_2]$.

The last step in this section is to compare the numerical data with the analytical predictions. For that reason, we use both Ansatz 2.8 and 2.18 and apply the proper algorithm for each of them. The results are in Figures 2.15, 2.16, 2.17 and 2.18.

Computationally-wise, the dispersion Ansatz performs much faster than the ρ Ansatz. Regarding the latter, using the `FindMaximum` tool as it is was not enough: it was necessary to increase its parameters `PrecisionGoal` and `AccuracyGoal` to 9; moreover, `MaxIterations` was set to 1800, while using the `InteriorPoint` method for the search of the maximum. In contrast, the parameters `PrecisionGoal` and `AccuracyGoal` were set to 9 and `MaxIterations` to 1000, for the former case. It was this big discrepancy that made up for the large difference in computational time. Nonetheless, both Ansätze delightfully agree with the proposed analytical solution, making it clear that the two approaches are robust. Note that the proposed parameters were not enough to obtain the figures bellow: in some cases, convergence was so slow that it became necessary to increase either n, M, `MaxIterations` or a combination of these. For the spectrum with three bound-states, using the ρ Ansatz, it takes too long to obtain satisfactory results, hence fewer points were plotted.

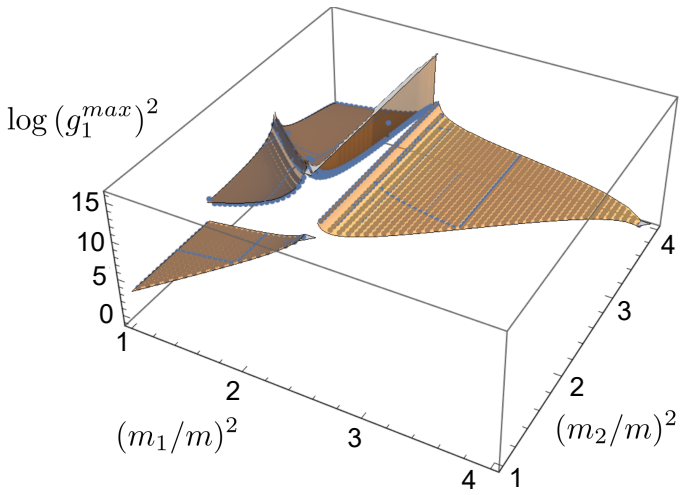

FIGURE 2.15: Maximization of g_1^2 subject to the mass spectrum $\{m_1, m_2\}$ and the usual conditions (dispersion Ansatz). Numerical data is in blue dots, while the analytical results correspond to the orange surfaces. $M = 10$ (numerical cutoff) and $n = 60$ (number of points where unitarity is imposed) were used.

Up until now, we have only been concerned with determining the QFT whose S-matrix had the greatest possible value for the coupling of its lightest particle to the mass of the b.s.. However, many other theories reside in the "inner region" (i.e., allowed region of QFTs; check the blue region in Figure 2.8, for example) which we have not addressed. For that reason, we briefly study, in the next subsection, how the value of the S-matrix at the crossing symmetric point evolves with the value of g_1^2.

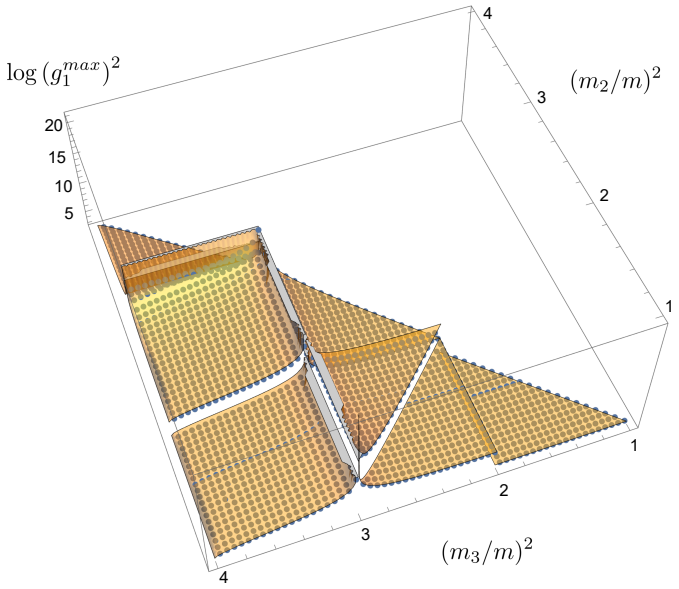

FIGURE 2.16: Maximization of g_1^2 subject to the mass spectrum $\{m, m_2, m_3\}$ and the usual condition (dispersion Ansatz). Numerical data is in blue dots, while the analytical results correspond to the orange surfaces. $M = 10$ (numerical cutoff) and $n = 60$ (number of points where unitarity is imposed), were used.

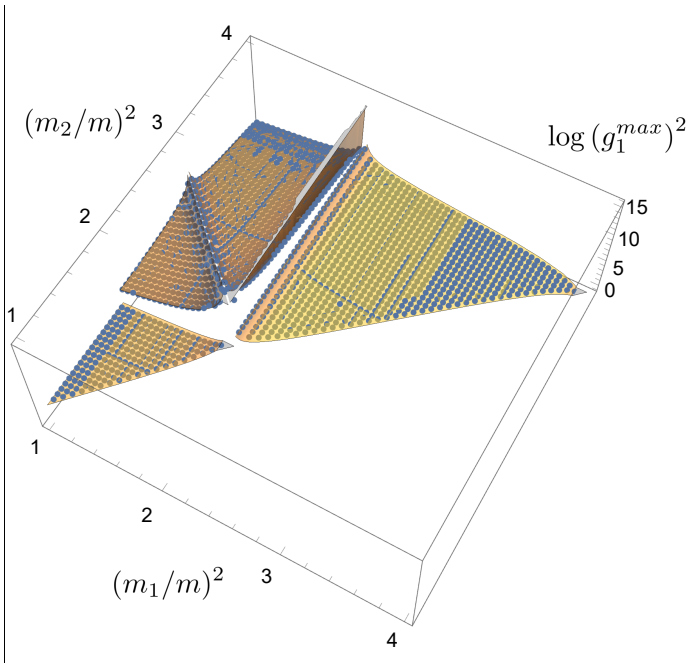

FIGURE 2.17: Maximization of g_1^2 subject to the mass spectrum $\{m_1, m_2\}$ and the usual conditions (ρ Ansatz). Numerical data is in blue dots, while the analytical results correspond to the orange surfaces. Using $M = 5$ (numerical cutoff) and $n = 200$ (number of points where unitarity is imposed), we can already see an almost perfect agreement between all the data.

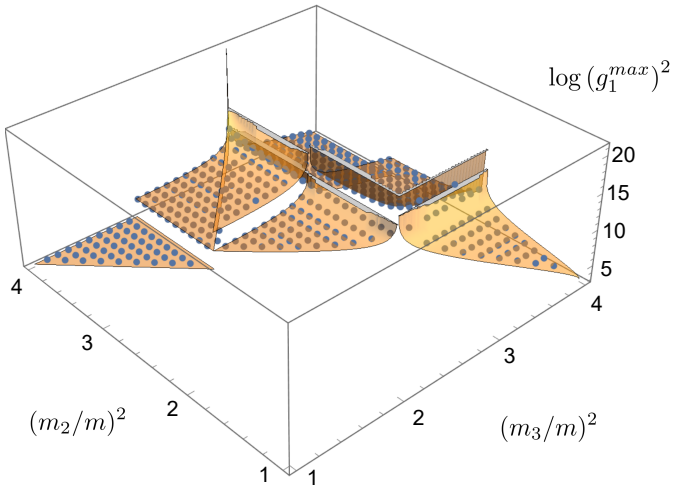

FIGURE 2.18: Maximization of g_1^2 subject to the mass spectrum $\{m, m_2, m_3\}$ and the usual conditions (ρ Ansatz). Numerical data is in blue dots, while the analytical results correspond to the orange surfaces. Using $M = 5$ (numerical cutoff) and $n = 200$ (number of points where unitarity is imposed), we can already see an almost perfect agreement between all the data.

2.1.8 $S(2)$ vs. g_1^2

The aim of this subsection is very simple: we consider the same QFT as in subsections 2.1.4 and 2.1.5, where there is only one bound-state of mass m_1 (apart from the lightest mass, m) coupled to m by an interaction strength g_1; the objective is to vary $g_1 \in [0, g_1^{max}]$ and maximize/minimize $S(2)$ subject to that coupling (using the `FindMaximum` and `FindMinimum` tools). This quantity, $S(2)$, comes as a natural extension of the *quartic coupling* in higher dimensions, $S(s^*, t^*, u^*) = S\left(4/3, 4/3, 4/3\right)$ (which is of historical importance), in that both are calculated at the crossing symmetric point - in 2D, for the former case. Even though this is region of unphysical energies, it is one in which the S-matrix attains real values. The upcoming results are a novelty, and hence do not follow any paper - to our knowledge.

Without loss of generality, the Ansatz in the ρ variable will be used, although the other one would be correct as well. Also, we set the mass of the lightest particle to 1, $m = 1$. Figure 2.19 illustrates the maximum and minimum allowed values of $S(2)$ as function of g_1.

There are some features in the previous figure that may be worth discussing. The most striking aspect is the fact that the minimum and maximum values of $S(2)$ ($s = 2m^2$, but we set $m = 1$) seem to converge as g_1 approaches g_1^{max}: this means that there is only one theory, for $m_1 = \sqrt{3}$, whose S-matrix has a coupling g_1^{max}. If somehow there was

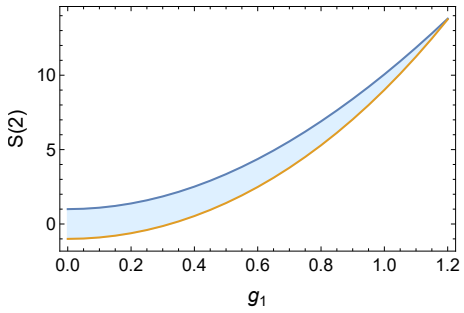

FIGURE 2.19: Plot of g_1 vs. $S(2)$ for $m_1 = \sqrt{3}$. The blue curve represents the maximum value of $S(2)$ for a given g_1; the orange represents the minimum. The blue shaded region contains all allowed values. As g_1 approaches its maximum value, there should only be one solution for both maximum and minimum values: $S_{SG}(2)$. The solutions to $g_1 = 0$ are free bosons ($S(2) = +1$) and free Majorana fermions ($S(2) = -1$) [28].

any questions regarding the fact that there might be another S-matrix whose interaction strength was as great as possible, this makes it transparent: only the sine-Gordon S-matrix is allowed.

As g_1 gets smaller, the $\max\left[S(2)\right]$ and $\min\left[S(2)\right]$ curves open up, delimiting the light blue region in Figure 2.19: it consists of the space of all the allowed values of $S(2)$ for each g_1.

Eventually, g_1 reaches the origin and the $\max/\min$ curves attain curious values: ± 1, respectively. This comes as no surprise: on account of $S(s) = 1 + i \times T$, if $\left|S(2)\right| = 1$ it means that there is no connected part, i.e., it must be a free particle! In this case, $S(2) = +1$ coincides with the S-matrix for free bosons, whereas $S(2) = -1$ represents that of free Majorana fermions [28].

Lastly, the S-matrix components pertaining to each solution are plotted. Of relevance to us are the S-matrices for $g_1 = 0$ and $g_1 = g_1^{max}$, which were discussed previously. The result is in Figure 2.20 and 2.21

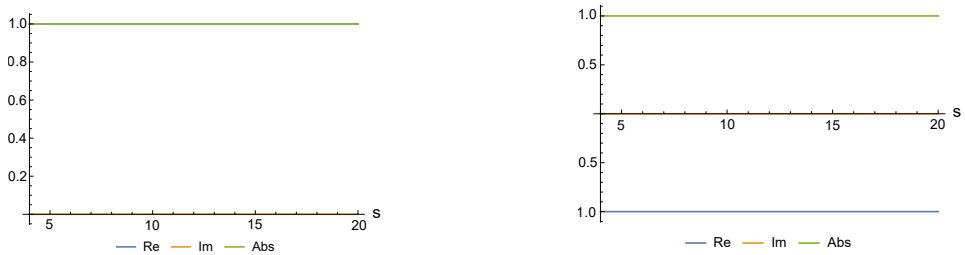

(A) (B)

FIGURE 2.20: Plot of the S-matrix components for the case (A) $S(2) = +1$ (free bosons) and (B) $S(2) = -1$ (free Majorana fermions). As predicted previously, these S-matrices are purely real.

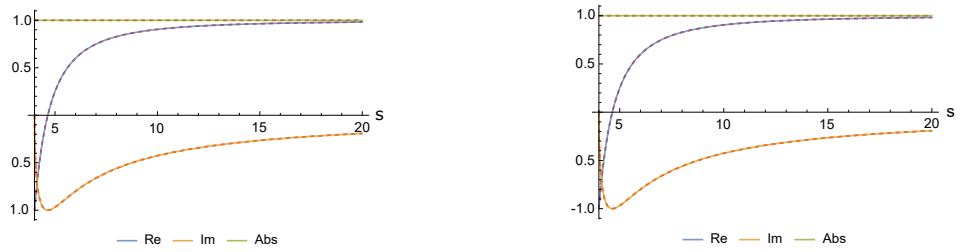

FIGURE 2.21: Resulting S-matrix components of the solutions to (A) $\max S(2)$ and (B) $\min S(2)$ when $g_1 = g_1^{max}$. The red dashed plots correspond to the Real, Imaginary part and Absolute value of the sine-Gordon S-matrix. Clearly, both solutions agree perfectly with the integrable QFT.

In particular, Figure 2.21 corroborates our assumption that the S-matrix that minimizes and maximizes, simultaneously, $S(2)$ for $g_1 = g_1^{max}$ is unique!

With this short subsection, we end the discussion of maximization of cubic couplings using the primal approach. Before closing this section, though, there is yet another aspect that can be explored. According to Figure 2.20, when $g_1 = 0$ the S-matrix at $s = 2m^2$ is bounded by $\left|S(2m^2)\right| = 1$; however, any value in-between is also an allowed QFT. With that in mind, we set to explore yet another quantity of the S-matrix, its second derivative at $s = 2m^2$ vs. $S(2m^2)$ which, as we will see, is closely related to [28].

2.1.9 $S(2)$ vs $S''(2)$

In the absence of bound-states, relevant quantities to study are $S(2m^2)$ and its derivatives, $S^{(n)}(2m^2),\ n > 1$. This can be better understood in the optics of Effective Field Theory, EFT. At low energies, in 2D, for weakly coupled and massless theories, one can dismiss Feynman diagrams that are not tree-level-like. In this context, the amplitude admits a low EFT expansion [29]

$$T_{low}(s,t) = -g^2\left[\frac{1}{s}+\frac{1}{t}\right] - \lambda + g_2(s^2+t^2) + g_4(s^2+t^2)^2 + ... \tag{2.27}$$

which can be obtained from a Lagrangian density

$$\mathcal{L}_{low}(s) = -\frac{1}{2}(\partial_\mu\phi)^2 - \frac{g}{3!}\phi^3 - \frac{\lambda}{4!}\phi^4 + \frac{g_2}{2}[(\partial_\mu\phi)^2]^2 + ... \tag{2.28}$$

Specifically, in the absence of a cubic coupling, $g^2 = 0$. Thus, Equation 2.27 simply becomes

$$T_{low}(s) = -\lambda + c_2 s^2 + c_4 s^4 + ... \tag{2.29}$$

where $\{c_i\}$ are just a redefinition in terms of $\{g_i\}$. Effectively speaking, it is a Taylor expansion around $s = 0$. Therefore, the study of $S(2m^2)$ simply relates to the latter by a modification of the point around which we choose to Taylor expand: instead of $s = 0$, one chooses $s = 2m^2$.

Since unitarity and crossing symmetry are required, it is evident that $S(2m^2)$ is a local extremum of $S(s)$: $s = 2m^2$ is a symmetric point, which means that $S(2m^2 + i \times \epsilon) = S(2m^2 - i \times \epsilon)$, and thus it can only be a local maximum or minimum. This section will closely follow the philosophy of [28]: given $S(2m^2)$ in the allowed range, we extremize $S^{(2)}(2m^2)$. The relation between our results and that of [28] will become clearer once the appropriate change of basis is introduced; in the meantime, we present the result of the suggested problem in Figure 2.22

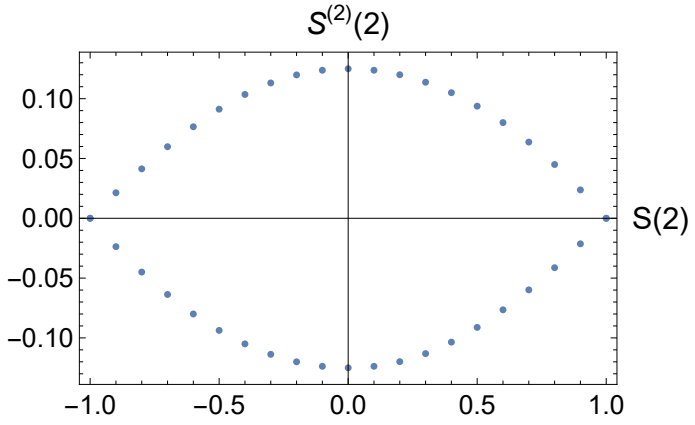

FIGURE 2.22: Plot of $S^{(2)}(2)$ vs $S(2)$ ($m = 1$).

To make contact with [28], we make use of some definitions therein proposed,

$$\Lambda \equiv -\lim_{s\to 2m^2} T(s), \quad \Lambda^{(n)} \equiv \lim_{s\to 2m^2} \partial_s^n T(s) \tag{2.30}$$

where $T(s)$ is the same as defined in subsection 2.1.2. Using the definition of $S(s)$, we get the simple result (we set $m = 1$)

$$\begin{aligned} S(2) &= 1 + i \times \frac{T(2)}{2\sqrt{2(2-4)}} \\ &= 1 + i \times \frac{-\Lambda}{4i} \\ \Leftrightarrow \Lambda &= 4\left(1 - S(2)\right) \end{aligned} \tag{2.31}$$

and

$$\begin{aligned}\Lambda^{(2)} &= \lim_{s\to 2}\partial_s^2 T(s)\\ &= \lim_{s\to 2}\partial_s^2\left[2\sqrt{s(s-4)}\left(\frac{S(s)-1}{i}\right)\right]\\ &= \lim_{s\to 2}\left\{2\partial_s^2\sqrt{s(s-4)}\left(\frac{S(s)-1}{i}\right)\right.\\ &\quad \left.+2\sqrt{s(s-4)}\partial_s^2\left(\frac{S(s)}{i}\right)+4\partial_s\left[\sqrt{s(s-4)}\right]\partial_s S(s)\right\}\\ &= 1-S(2)+4S^{(2)}(2)\end{aligned} \tag{2.32}$$

All that is left is to check whether our numerical data coincides with Figure 1 in the article. Since we do not have the data used in said plot, we proceeded with the second best solution: using a specialized piece of software such as `plotdigitizer`, we were able to get a sample of points from the image in question and plot it against our own. The final result is illustrated in Figure 2.23

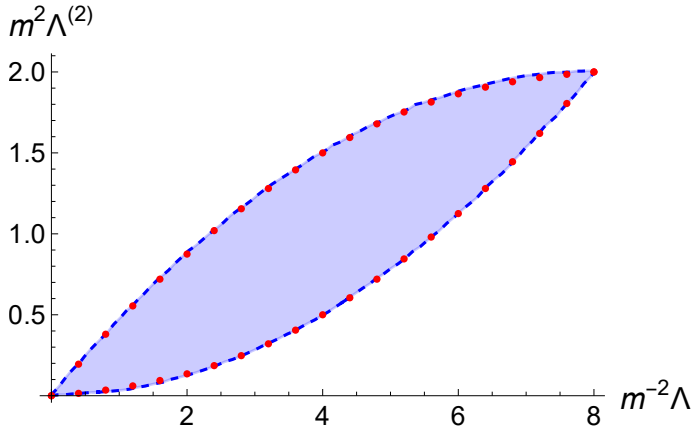

FIGURE 2.23: Data from [28] (blue dashed curve) vs. our numerical data (red points), after the proper coordinate change. Our data matches that of the paper perfectly. Thus, only the latter will be used. The shaded region is that of the allowed QFTs. Heavily adapted from [28].

Visibly, the analytical solution in red splendidly agrees with our data. The most interesting part of this shape is that in its boundaries reside known theories. For example, the sinh-Gordon model (very similar to the sine-Gordon model; however, this model does not admit bound-states, since its poles are outside the physical sheet) can be shown to correspond to the parameter

$$\Lambda = 8m^2\left(1-\frac{1}{1+\sin\gamma}\right), \quad \gamma\in[0,\pi/2] \tag{2.33}$$

where m is the mass of the lightest particle in the theory and $\Lambda \in [0, 4m^2]$. In turn, the S-matrix can be written as

$$S(\theta) = 1 + \frac{2i\Lambda}{(\Lambda - 8m^2)\sinh\theta - i\Lambda} \tag{2.34}$$

where θ is the rapidity. Using Equations 2.31 and 2.32, it is straightforward to determine the corresponding $(\Lambda, \Lambda^{(2)})$ coordinates.

On the other hand, if γ is analytically continued, the *Staircase Model* [30] is obtained. In this case, $\gamma = \frac{\pi}{2} + i\theta_0$ which, in practical terms, means that the Staircase model is given precisely by Equation 2.34 but with $\Lambda \in [4m^2, 8m^2]$.

Finally, two known points can be identified

$$S_{f.b.}(s) = +1 \implies (\Lambda, \Lambda^{(2)}) = (0, 0); \quad S_{f.M.f.}(s) = -1 \implies (\Lambda, \Lambda^{(2)}) = (8, 2) \tag{2.35}$$

for a free boson and a free Majorana fermion, respectively. These models are carefully identified in Figure 2.24, together with the analytical curve of Figure 2.23.

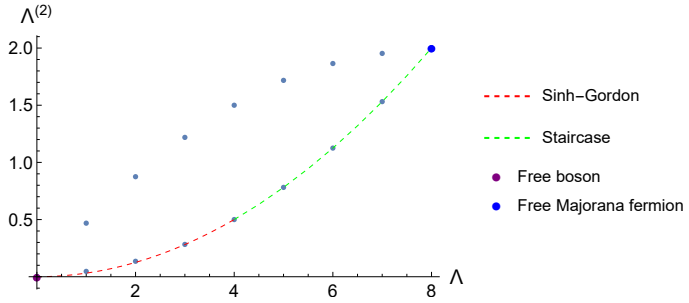

FIGURE 2.24: Known models vs. points from Figure 2.23.

Unfortunately, we do not know what theories lie on the upper part of this region. Moreover, there was an attempt to plot a known deformation, the $T\bar{T}$ deformation: however, instead of lying only on the boundary, it pierced the inner region. Thus, we have decided not to plot it altogether.

As a bonus, we can also study the space of parameters $S(2)$ vs. $S^{(2)}(2)$ vs. $S^{(4)}(2)$: for each $S(2)$, there is a maximum/minimum value that $S^{(2)}(2)$ can take; spanning the values between these points, one can now maximize/minimize $S^{(4)}(2)$, obtaining what we call the $S^{(4)}(2)$ *pancake*. This procedure results in Figure 2.25

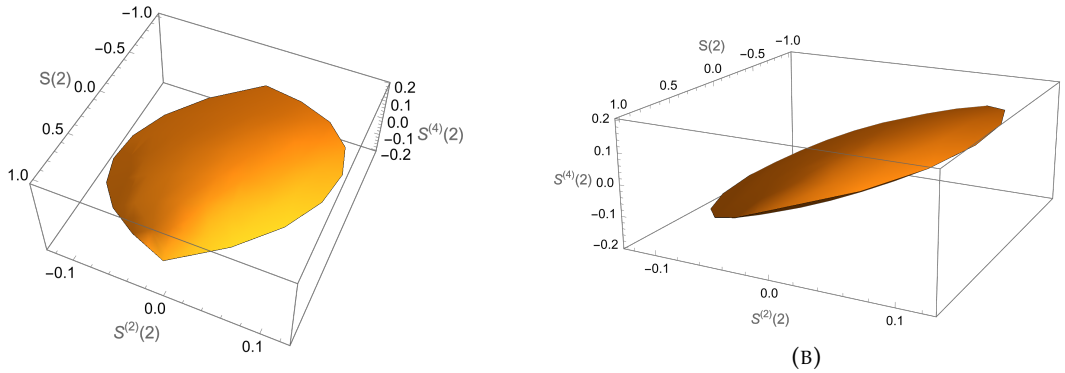

(A) (B)

FIGURE 2.25: Result of maximizing and minimizing $S^{(4)}(2)$ in the allowed region for $S(2)$ and $S^{(2)}(2)$.

2.2 Dual approach

So far, only the primal approach was invoked whenever optimization routines took place. In subsection 2.1.1, however, another was mentioned: the dual approach. It is the aim of this section to explore this formalism and understand its advantages when compared with the primal method. All of the results can be found in [31, 32], which will be closely followed.

2.2.1 Dual philosophy

In the cases thus far seen, the primal strategy seemed to yield accurate and stable results - for suitable choices of N_{max}. Even in these cases, increasing this parameter beyond the optimal parameter results in instabilities. With these instabilities, our target variables do not improve monotonically, as expected, with the increase in the parameter space. Be as it may, it is not always the case: when carried out in higher dimensions, the same optimization problem analysed in past sections yields unstable results for certain regions of m_1^2, [19] (the instability issue is also observed in other contexts, [33]). This raises several questions, to name a few: how can one improve the results? Is the data ever going to converge? For the first case, it may just be a matter of choosing an adequate Ansatz, which is ofttimes complex; regarding the second case, it is not very clear.

To solve some of these issues, the dual problem is introduced: instead of building the space of the allowed S-matrices, we can rule out unphysical theories and carve out the appropriate S-matrix region. This strategy was proposed back in the 70's, so it comes as no surprise that, with technological advances, it is brought to life once more. Hence, we can

approach the boundaries of the S-matrices space from two sides - with both approaches combined - and constrain the true sought after value. To make matters clearer, we start by reviewing the primal approach systematically.

Let us consider the same problem as before: in a 2D theory with a single stable particle of mass m and a bound-state m_1, what is the maximum value of the cubic coupling g_1 consistent with $2 \to 2$ scattering amplitude $T(s)$ and the usual axioms? Schematically, this corresponds to the optimization problem

$$\underset{\{T(s),\, g_1^2\}}{\text{maximize}} \quad g_1^2 \tag{2.36}$$

subject to the constraints

$$\mathcal{A}(s) \equiv T(s) - \left(T_\infty - \frac{g_1^2}{s - m_1^2} + \int_{4m^2}^{\infty} \frac{dz}{\pi} \frac{\text{Im}\, T(z)}{s - z + i0^+} + (s \leftrightarrow 4m^2 - s) \right) = 0, \quad s \geq 4m^2 \tag{2.37}$$

$$\mathcal{U}(s) \equiv 2\ \text{Im}\, T(s) - \frac{|T(s)|^2}{2\sqrt{s(s-4m^2)}} \geq 0, \quad s \geq 4m^2 \tag{2.38}$$

where the same conventions as in subsection 2.1.3 were used, and the maximization is over the space of amplitudes $T(s)$ and couplings g_1 (which are the symmetric of the residues of $T(s)$ at $s = m_1^2$). These constraints are already known to us: Equation 2.37 imposes, simultaneously, crossing symmetry and an analytical structure - poles correspond to bound-states, whereas cuts correspond to multi-particle, physical regions of scattering; Equation 2.38 is just unitarity written as a function of $T(s)$ instead of $S(s)$. $T(s)$ is said to be feasible if it satisfies both equations.

Constraints 2.37 and 2.38 are affine and convex, respectively. Moreover, the quantity which is being maximized is a linear map in the space of analytical functions; thus, this optimization problem is an *infinite dimensional convex optimization*, which can be solved analytically using the Maximus Modulus Principle ([3, 26]) or with the primal approach.

Anyhow, as previously stated, the last strategy suffers from some problems. In this case, there are two shortcomings that particularly stand out. On the one hand, as discussed, it may be complicated to come up with a proper Ansatz: some may converge faster than others, but there is no a priori technique to figure this out. On the other hand, one may need to impose further constraints or variables - be it higher point unitarity constraints or higher point amplitudes. This seemingly inoffensive action may cause some undesirable effects: a previously allowed solution of the original problem of parameters may be excluded from the final set of solutions in the extended space. As in conformal

bootstrap, it would be more favourable if bounds on more general spaces remained valid upon imposing the full set of QFT constraints. In the end, it turns out that the dual formulation solves both shortcomings. As such, we present the simple example of [32].

Let us consider the Lagrangian density

$$\mathcal{L}(T,\omega,\lambda) = g_1^2 + \int_{4m^2}^{\infty} ds\ \omega(s)\mathcal{A}(s) + \lambda(s)\mathcal{U}(s) \tag{2.39}$$

where $\lambda(s) \geq 0$ and $\omega(s)$ are the *dual variables* to $\{T(s), g_1^2\}$, and define the dual function

$$d(\omega,\lambda) = \sup_{\{T,g_1^2\}} \mathcal{L}(T,\omega,\lambda) \tag{2.40}$$

It is important to note that the supremum is taken over the unconstrained space of amplitudes $T(s)$. With this new object, some observations can be made. Firstly, we note that since

$$\inf_{\{\lambda\geq 0,\omega\}} \mathcal{L}(T,\omega,\lambda) = \begin{cases} g_1^2 & \text{, if } T \text{ is feasible} \\ -\infty & \text{, otherwise} \end{cases} \tag{2.41}$$

then it is true that

$$g_{1,*}^2 = \sup_{\{T,g_1^2\}} \left[\inf_{\{\lambda\geq 0,\omega\}} \mathcal{L}(T,\omega,\lambda) \right] \tag{2.42}$$

since, ideally, $\mathcal{A}(s) = 0$ and $\mathcal{U}(s) \geq 0$. With this is mind, Equation 2.40 implies that

$$\begin{aligned} d(\omega,\lambda) = \sup_{\{T,g_1^2\}} \mathcal{L}(T,\omega,\lambda) &\geq \inf_{\{\omega,\lambda\}} \left[\sup_{\{T,g_1^2\}} \mathcal{L}(T,\omega,\lambda) \right] \\ &\geq \sup_{\{T,g_1^2\}} \left[\inf_{\{\omega,\lambda\}} \mathcal{L}(T,\omega,\lambda) \right] \overset{2.42}{=} g_{1,*}^2 \,, \end{aligned} \tag{2.43}$$

where the *Max-min* inequality was used. This inequality is often referred to as the *Weak Duality*, which differs from the *Strong Duality* by the inequality sign. This partially solves the first of the presented shortcomings: by exploring the space of parameters $\{\omega, \lambda\}$ it is possible to exclude some regions and put bounds on the maximum value allowed for the primal solution. Thus, it serves as an indicator of how well a particular Ansatz may be performing. The equivalent to the primal approach is, then,

$$\underset{\{\lambda(s),\omega(s)\}}{\text{minimize}} \quad d(\omega,\lambda) \tag{2.44}$$

subject to the constraint

$$\lambda(s) \geq 0 \tag{2.45}$$

What we have been describing so far is a procedure commonly used in optimization problems in Mathematics; however, in this context, there are other assumptions which can further simplify the problem at hand. To begin with, the analyticity of amplitude $T(s)$ can be captured by the dual variable $\omega(s)$ by simply defining a *dual scattering function*, $W(s)$, odd under crossing and whose absorptive part corresponds to $\omega(s)$ [32]:

$$W(s) \equiv -\frac{1}{\pi}\int_{4m^2}^{\infty} dz\, \omega(z)\left(\frac{1}{s-z+i0^+}-\frac{1}{s-4+z+i0^+}\right), \quad \operatorname{Im} W(s)=\omega(s) \tag{2.46}$$

In Appendix A, it is shown how $W(s)$ emerges naturally from 2.39 and the Sokhotski–Plemelj theorem. It is also shown that Equation 2.39 reads

$$\mathcal{L}(T,\omega,\lambda) = g_1^2\left[1+\pi \operatorname{Re} W(m_1^2)\right] + \int_{4m^2}^{\infty} ds \operatorname{Im}\left[W(s)T(s)\right] + \lambda(s)\mathcal{U}(s) \tag{2.47}$$

It is clear from this expression that $\mathcal{L}(T,\omega,\lambda)$ is now local in T, which previously was not the case. This will become important in the next step, which will enable us to perform both the maximization over T and the minimization over λ simultaneously (cf. Equations 2.40 and 2.44). Firstly, though, one should note that, because $\mathcal{L}$ is linear in g_1^2,

$$d(W,\lambda) = +\infty \qquad \text{unless} \qquad \operatorname{Re} W(m_1^2) = -\frac{1}{\pi} \tag{2.48}$$

Since that the optimization problem is undefined unless the constraint 2.48 is satisfied, we restrict ourselves to the space of $W(s)$ which satisfies it. Secondly, due to locality, one can take the Euler-Lagrange equations of 2.47 (treating $\operatorname{Re} T(s)$ and $\operatorname{Im} T(s)$ as independent variables, which is valid in this context) varying $T(s)$ to show that

$$T_c(s) = \left[\frac{\operatorname{Im} W(s)}{\lambda(s)} + i\left(2+\frac{\operatorname{Re} W(s)}{\lambda(s)}\right)\right]\frac{1}{2\rho_{11}^2(s)} \tag{2.49}$$

where $\rho_{11}^{-2}(s) \equiv 2\sqrt{s(s-4m^2)}$ (this solution can be shown to correspond to a maximum, so long as $\lambda > 0$). Substituting Equation 2.49 and assuming that Equation 2.48 is satisfied, $d(W,\lambda)$ should read

$$d(W,\lambda) = \int_{4m^2}^{\infty} ds\left[\frac{|W(s)|^2}{4\lambda(s)} + \operatorname{Re} W(s) + \lambda(s)\right]\frac{1}{\rho_{11}^2(s)} \tag{2.50}$$

Now, all that is left is to minimize in the dual variable space of parameters $\{\lambda(s), W(s)\}$. If $D(W) \equiv \inf_{\{\lambda\}} d(W, \lambda)$, then

$$D(W) = \int_{4m^2}^{\infty} ds \, \left[|W(s)| + \mathrm{Re}\, W(s)\right] \frac{1}{\rho_{11}^2(s)} \tag{2.51}$$

since the positive solution $\lambda(s) = \frac{|W(s)|}{2}$ was used. This means that Equation 2.49 yields

$$T_c(s) = \frac{i}{\rho_{11}^2(s)} \left(1 + \frac{W^*(s)}{|W(s)|}\right) \tag{2.52}$$

which will be later verified in the plots.

Thus, the dual optimization problem simplifies to

$$\underset{\{W(s)\}}{\text{minimize}} \quad D(W) = \int_{4m^2}^{\infty} ds \, \left[|W(s)| + \mathrm{Re}\, W(s)\right] \frac{1}{\rho_{11}^2(s)} \tag{2.53}$$

subject to the condition that

$$W(m_1^2) = -\frac{1}{\pi} \tag{2.54}$$

The described problem can be solved numerically, similarly as the primal problem, using functions such as `FindMinimum` of `Mathematica` instead of `FindMaximum`. However, to proceed, we must suggest a truncated Ansatz. Using, for example, the same foliation ρ as before,

$$\rho(s) = \frac{\sqrt{2m^2} - \sqrt{4m^2 - s}}{\sqrt{2m^2} + \sqrt{4m^2 - s}} \tag{2.55}$$

and the Ansatz suggested in [32],

$$W(s) = \frac{1}{s(4m^2 - s)} \sum_{n=1}^{N_{max}} a_n (\rho(s)^n - \rho(t)^n) \tag{2.56}$$

one is able to carry out the maximization of g_1^2 (actually, the minimization of $D(W)$) in the space of a_n's. In the next subsection, we proceed to do so - and the results will agree perfectly with the predictions.

2.2.2 Maximization of the cubic coupling

In the previous section, the dual approach was introduced as well as a possible numerical pseudo-algorithm to implement it. The context is the following: consider the 2D scattering of identical particles of mass m, whose mass spectrum allows for a bound-state of mass m_1^2 and whose coupling to the lightest particle of the theory is g_1^2. The objective is to maximize said quantity. According to preceding calculations, it corresponds simply

to minimizing the functional 2.53 subject to the dual constraint 2.54. At best, we expect the solution to agree with the sine-Gordon QTF (cf. subsection 2.1.6), in which case the absolute value of the S-matrix should saturate unitarity.

Figure 2.26 shows the result of carrying out the optimization. Numerically speaking, we used $N_{max} = 5$ for the cutoff and Lagrange interpolation to determine the integral (since the referred integral depends on unknowns, no tool was available to determine it promptly); the interpolation made use of 150 points on a Chebyshev grid*, determined with high precision. Regarding the `FindMinimum` function, the standard parameters yielded accurate results, so no further changes were due.

As expected, the dual function does an incredible job at finding the maximum value for the desired coupling. Moreover, even with a substantially large set of positions to maximize in, the algorithm took around 1,5 minutes to finish, which is considerably fast (the ρ algorithm was appreciably slower even with a smaller size of samples, for example; is may be as fast as with using the dispersion Ansatz, with the added bonus of always being rigorous).

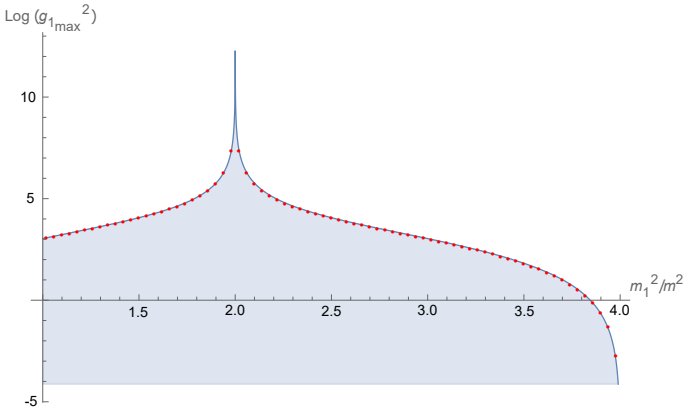

FIGURE 2.26: Result of maximizing the cubic coupling g_1^2 between the masses m and m_1, for the S-matrix element of the scattering of two m particles with only one bound-state. In red, we present the numerical data; the curve which they rest upon is the residue of the sine-Gordon S-matrix element. The blue shaded region consists of the allowed space of solutions consistent with our assumptions.

Another aspect which we commented on were the S-matrix components of each solution vs. the sine-Gordon model. To that end, Figure 2.27 is presented. Once more, one can notice a remarkable agreement between the numerical data and the exact solution.

Lastly, it remains to be checked if, in fact, the algorithm has already converged or if one needs to adjust some parameters. Figure 2.28 clearly proves that, even for N_{max} as

*Roots of the Chebyshev polynomials of the first kind. Given by $x_k = \cos\left(\frac{2k-1}{2n}\pi\right)$, $k = 1, ..., n$.

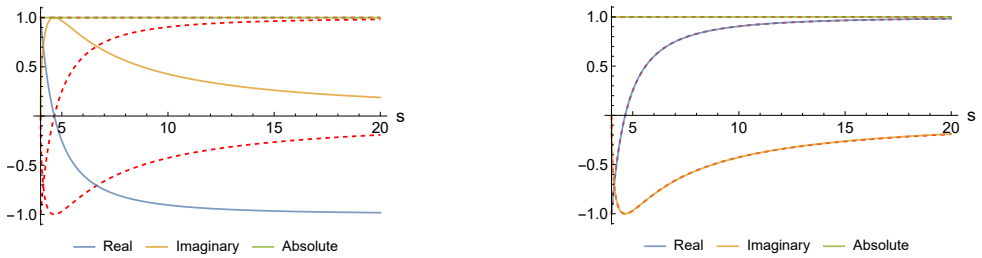

(A) $m_1 = m$ (B) $m_1 = \sqrt{3}$

FIGURE 2.27: S-matrix components vs. sine-Gordon for (A) $m_1 = m$ and (B) $m_1 = \sqrt{3}m$. The same phenomenon as in Figure 2.9 occurs with the dual approach. These plots were obtained according to Equation 2.52.

low as 5, the algorithm has attained its optimal value, rendering all of the above analysis valid.

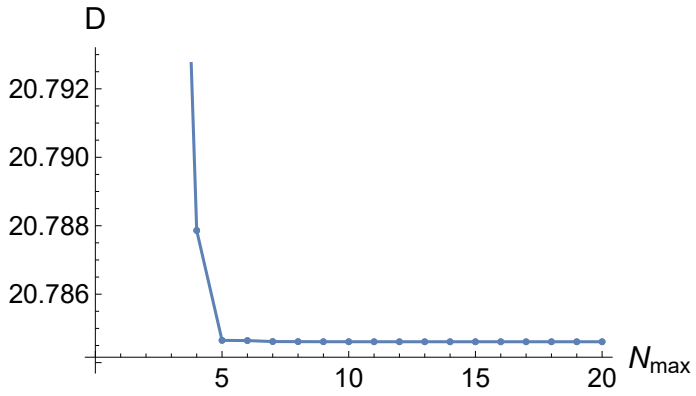

FIGURE 2.28: Convergence of the dual objective, D, as a function of N_{max} and for $m_1 = \sqrt{3}m$. For $N_{max} = 5$, D seems to reach its minimum optimal value. Since higher N_{max} would only prove computationally heavier, the former value was chosen.

With this method, it should be possible to reproduce the two and three b.s. case numerically. However, this proved to be harder than expected, and thus it is not presented.

Regarding the quartic coupling ($S(2)$ while $g_i^2 = 0$, i.e., no b.s.), a study was carried out in order to generalize the procedure of subsection 2.2.1 for when $g_i^2 = 0$ and $S(2)$ is the new objective. Despite our best efforts, it was impossible to obtain the analytical value.

Hereupon, we reach the end of the study in 2D. The next natural step is to generalize most (if not all) the previous results for higher dimensions, specifically for 4D. However simple it may seem to add extra dimensions, the reality is that it will be necessary to review the base assumptions of unitarity and crossing, which, in higher dimensions, take a rather overwhelming form if not treated carefully.

Chapter 3

4D Scattering: massive scalar particles

3.1 Introduction to higher dimensions

In the two dimensional case, two aspects made the bootstrap formalism rather accessible and straightforward: the fact that there was only one independent Mandelstam variable (s was the common choice) and the useful coincidence that the connected part had the same support as the disconnected part. Both played a vital role in simplifying unitarity and crossing symmetry requirements alike.

Unfortunately, such ease is not to be expected for higher dimensions: in 4D, for example, the number of independent Mandelstam variables is two rather than one. This means, for instance, that scattering angles are relevant, immediately destroying the same-support argument. However, it is not the most concerning issue: unitarity, which so far was described by the simple Equation 2.5, takes a more complex form, which is not easily solvable, at least as it is. It turns out that this is a long solved issue in the literature [1, 11], and still commonly used [19]: one must consider a *partial-wave expansion* of the amplitude.

Before diving right into the mathematical aspects, it may be fruitful to understand the physical intuition behind the partial-wave approach. All throughout this chapter, scalar, spinless particles will be considered: only the relative orbital momentum between both particles (we will simply study the $2 \to 2$ scattering) matters. Since the collision between the particles happens with no external influence (i.e., closed system), total angular momentum is a conserved quantity: thus, it is convenient to consider the projection of

the scattering amplitude for each angular-momentum state separately. However, the initial state is usually a superposition of many possible angular-momentum eigenstates, and therefore it makes more sense (and is actually necessary) to considered the total scattering amplitude as a sum over all the composing partial-waves amplitudes.

Let us recall some important results developed in Chapter 1. Therein, the scattering angle is written in Equation 1.23 as

$$x = \cos(\theta) = 1 + \frac{2t}{s-4} = -1 - \frac{2u}{s-4} \tag{3.1}$$

and the amplitude $T(s,t)$ is expanded as in Equation 1.26

$$T(s,t) = \sum_{\ell=0}^{\infty} n_\ell^{(d)} f_\ell(s) P_\ell^{(d)}(\cos(\theta)) \tag{3.2}$$

where $f_\ell(s)$ are the partial-wave coefficients, the sum runs over even ℓ (odd ℓ yield 0), $n_\ell^{(d+1)}$ are normalization factors in Equation 1.27. According to Equation 1.28,

$$f_\ell(s) = \frac{\mathcal{N}_d}{2} \int_{-1}^{1} dx \, (1-x^2)^{\frac{d-3}{2}} P_\ell^{(d)}(x) \, T(s, t(x)) \tag{3.3}$$

This leads to the most important result, Equation 1.30

$$S_\ell(s) = 1 + i \frac{(s-4)^{\frac{d-2}{2}}}{\sqrt{s}} \frac{\mathcal{N}_d}{2} \int_{-1}^{1} dx \, (1-x^2)^{\frac{d-3}{2}} P_\ell^{(d)}(x) \, T(s, t(x)) \tag{3.4}$$

Lastly, there are a couple of conditions further assumed for the amplitude function $T(s,t,u)$:

- **Crossing Symmetry:** for the scattering of identical particles,

$$T(s,t) = T(t,s) = T(u,t) \tag{3.5}$$

  The first equality can be obtained from the analysis of the LSZ method [18, 34, 35]; the second, $t \leftrightarrow u$, originates from Bose symmetry.

- **Real and Extended Analyticity:** regarding real analyticity, we assume that

$$T(s^*, t^*) = T^*(s,t) \tag{3.6}$$

  All the analyticity results which shall be considered can be revised in section 1.2.1. When it comes to extended analyticity, it is important to stress that it is yet to be rigorously and axiomatically proven. However, there is a great agreement between

the results with extended analyticity and those obtained (without it) in older literature. That being said, it consists in the assumption that $T(s,t)$ is an analytic function for complex s and t, except for potential poles in $0 < s < 4m^2$ and a cut starting at $s = 4m^2$, as well as the image of said singularities under crossing.

In other words, it is considered that the S-matrix has the exact singularities predicted by unitarity and that is is analytic everywhere else as a complex function of two variables, s and t.

- **Unitarity:** From $\hat{S}^\dagger \hat{S} = \hat{1}$ we conclude that:

$$\begin{aligned} 1 &= \langle i|S^\dagger \hat{S}|i\rangle \\ &= \sum_m \langle i|S^\dagger|m\rangle\langle m|\hat{S}|i\rangle \\ &= \sum_{\ell,\,\text{even}} S_\ell^*(s) S_\ell(s) \\ &= |S_\ell^{2\to 2}(s)|^2 + \sum_{\ell>2,\,\text{even}} |S_\ell^{2\to n}(s)|^2 \\ \Leftrightarrow |S_\ell^{2\to 2}(s)|^2 &= 1 - \sum_{\ell>2,\,\text{even}} |S_\ell^{2\to n}(s)|^2 \\ \Leftrightarrow |S_\ell^{2\to 2}(s)|^2 &\leq 1 \end{aligned} \tag{3.7}$$

where the partial-wave projection was used from the second to third lines. Hence, using the notation of Equation 1.30, elastic unitarity yields the condition that

$$|S_\ell(s)|^2 \leq 1 \tag{3.8}$$

for $s \geq 4m^2$ and even ℓ. Considering that in $\mathbb{Z}_2$ even theories four-particle production occurs for $s \geq 16m^2$, then it is clear that Equation 3.8 is actually saturated in that region.

With the formalism out of the way, it is time to apply the S-matrix bootstrap program and put bounds on interesting quantities. Consequently, numerical considerations must be taken and an Ansatz will be needed. Such is the work carried out in the next section. All of the proceeding sections will be carried out in a 4 dimensional spacetime ($d = 3$).

3.2 Search for a numerical Ansatz

This problem seems all too familiar to us. Back in subsection 2.1.5, we were tasked with finding an Ansatz for $T(s)$, which in the end resulted in taking the extended function $T(s,t)$ and using the maps in 2.17. Unsurprisingly, the same map still applies to the problem at hand, so one had better review it. Let $m^2 = 1$.

Firstly, the condition that $s+t+u=4$ is relaxed, which consists in the extension of $T(s,t)$ to $T(s,t,u)$ as a function of three independent variables. Similarly as in subsection 2.1.5, we proceed with using the map

$$s \mapsto \rho_s = \frac{\sqrt{4m^2 - s_0} - \sqrt{4m^2 - s}}{\sqrt{4m^2 - s_0} + \sqrt{4m^2 - s}}, \qquad s = \frac{s_0(1-\rho_s)^2 + 16m^2\rho_s}{(1+\rho_s)^2} \tag{3.9}$$

(exactly the same as the aforementioned equation). The slight nuance regarding previous sections is that $s_0 = 4/3$, which corresponds to the crossing symmetric point $s = t = u = 4/3$ when $\rho_s = \rho_t = \rho_u = 0$ (recall that $d = 3$). With this map, we go from $(s,t,u) \mapsto (\rho_s, \rho_t, \rho_u)$. The final region to consider is that made up of three independent maps, ρ_s, ρ_t and ρ_u, all of which map the "x"-plane apart from the cut starting at $x > 4$ to the inside its respective unit disk: thus, all the cuts remain outside each of the unit disk. Said region must be a conjugation of the three separate ones, which form the Δ^3 polydisk defined by $|\rho_s| < 1 \cup |\rho_t| < 1 \cup |\rho_u| < 1$. Lastly, only the poles corresponding to bound states remain. Similarly to subsection 2.1.5 we can then write the natural Ansatz

$$T(s,t,u) = -\frac{g_1^2}{\rho(s) - \rho(m_1^2)} - \frac{g_1^2}{\rho(t) - \rho(m_1^2)} - \frac{g_1^2}{\rho(u) - \rho(m_1^2)} + \sum_{a,b,c=0} \alpha_{abc}\, \rho_s^a \rho_t^b \rho_u^c \tag{3.10}$$

where the triple ρ series is convergent inside the polydisk and m_1 is the bound-state whose interaction strength to the lightest particle is given by the coupling g_1^2. The following step is to impose the rest of the constraints considered in the previous section. When imposing crossing symmetry, one must ensure that the coefficients are symmetric in their indices. Furthermore, one must restrict the final solution to the region $s+t+u=4$, which has the effect that Equation 3.10 automatically obeys to the analytic and crossing symmetric structure previously imposed.

As with all numerical approaches, Equation 3.10 must be truncated. Following [19], the chosen truncation scheme is such that $a+b+c \leq N_{max}$; further restricting to the region $s+t+u=4$, has, in practice, the known effect of reducing the number of degrees of freedom in the Ansatz. Using the logic of the symmetric polynomials used in subsection

2.1.5 with the new equation

$$\rho_s^2\rho_t^2\rho_u + \rho_s^2\rho_u^2\rho_t + \rho_t^2\rho_u^2 + (\text{lower degree terms}) = 0 \tag{3.11}$$

one can set to 0 some coefficients, as is presented in Figure 3.1.

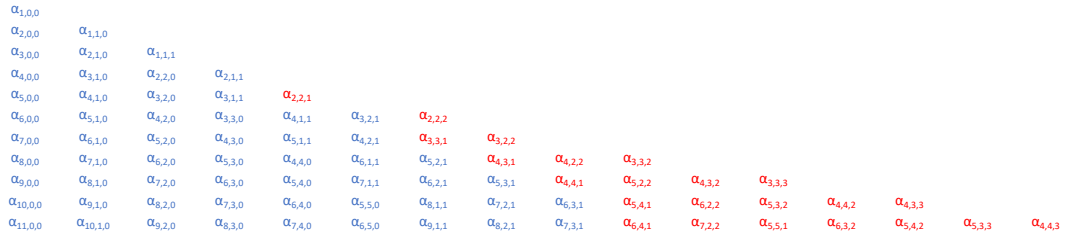

FIGURE 3.1: Independent coefficients (in blue) of the Ansatz 3.10. The coefficients in red are set to 0. At each level (N starts at 1), the number of terms which survive is equal to the total number of symmetric polynomials in three variables, of degree N, minus the total number of constraints for each case, which is the total number of polynomials of degree (N- 5): $\left\lfloor \frac{(N+3)^2+6}{12} \right\rfloor - \left\lfloor \frac{(N-2)^2+6}{12} \right\rfloor$. Adapted from [19].

All that remains are the coefficients α_{abc} which, together with g_1^2, make up for a space of parameters in which one can optimize certain quantities numerically. As in previous cases, we wish to push N_{max} as high possible, for only then can we truly determine an accurate bound for the objective at hand.

That being said, we proceed to the optimization program. In the next section, we try to bound the familiar term g_1^2 subject to unitarity and crossing symmetry constraints.

3.3 Maximization of the cubic coupling

Before delving too deep in the optimization scheme, we had better simplify some of the more general expressions introduced in section 3.1, since we wish to focus on 4D scattering ($d = 3$). For $d = 3$, Equation 1.30 reads

$$\begin{aligned} S_\ell(s) &\equiv 1 + i\frac{(s-4)^{\frac{d-2}{2}}}{\sqrt{s}} f_\ell(s) \\ &\overset{d=3}{=} 1 + i\sqrt{\frac{s-4}{s}}\frac{\mathcal{N}_3}{2}\int_{-1}^{1} dx\, P_\ell^{(3)}(x) T(s,t(x)) \\ &= 1 + \frac{i}{32\pi}\sqrt{\frac{s-4}{s}}\int_{-1}^{1} dx\, P_\ell(x) T(s,t(x)) \end{aligned} \tag{3.12}$$

When imposing unitarity, then, Equation 3.12 must be evaluated according to Equation 3.8 for a chosen s-grid and a selection of ℓs.

The objective of this section is to determine the maximum value of g_1^2 in Equation 3.10, as a function of m_1^2, allowed by unitarity and using said equation as the Ansatz. All the elements point to using the same maximization scheme as before, i.e., using `Mathematica`'s built-in function `FindMaximum`. However, this proved more difficult than anticipated: for one, the integral in Equation 3.12 needed to be determined either analytically or numerical with very high accuracy and precision; then, unitarity should be evaluated in a series of s-grid points and for various ℓs. To solve part of the issues, we evaluated said integrals, for 200 uniformly distributed ρ-grid points (which was translated into an s-grid using Equation 2.17), numerically with `NIntegrate` and with 200 effective digits in `WorkingPrecision`. However, upon imposing the constraints for $\ell \geq \ell_{max} = 20$, we came to the conclusion that `FindMaximum` was not suitable for the work at hand, be it for how it is implemented or for the fact that it was rather slow.

So as to solve this last issue, a very common optimization program was used instead: the SDP approach, a mathematical procedure which deals with semidefinite positive matrices and affine constraints. These types of problems have seen some implementations, which the SDPB software is an example of. The SDPB program [4, 36] is a rather known optimization routine used in CFT bootstrap, but with implementations in the S-matrix bootstrap field [19, 37, 38] (to name a few). The only inconvenience of using said program is the fact that constraints need to be put into a positive semidefinite matrix form, which means that one should do the same with 3.12. In essence, such matrix must have non-negative eigenvalues, among some common aspects. Fortunately, it can be achieved using the matrix inequality (Appendix F of [19])

$$\begin{pmatrix} 1 - \frac{\operatorname{Im} a}{2} & \operatorname{Re} a \\ \operatorname{Re} a & 2 \operatorname{Im} a \end{pmatrix} \succeq 0 \tag{3.13}$$

where $a \equiv \sqrt{\frac{s-4}{s}} f_\ell(s)$. This matrix inequality simultaneously imposes that $\operatorname{Im} a \leq 2$, $\operatorname{Im} a \geq 0$ and that $2 \operatorname{Im} a \geq \operatorname{Im}^2 a + \operatorname{Re}^2 a$. All of these conditions are neatly satisfied, as it is explained in detail in Appendix B.1.

Proceeding with the optimization as proposed, Figure 3.2 was obtained. These plots reveal "new" information which we will comment upon next; a more intricate and detailed analysis of the numerical aspects of this maximization routine can be found in [19].

First and foremost, there is a striking resemblance between Figure 3.2 and that of the maximization of the cubic coupling for lower dimensions. However, there are crucial

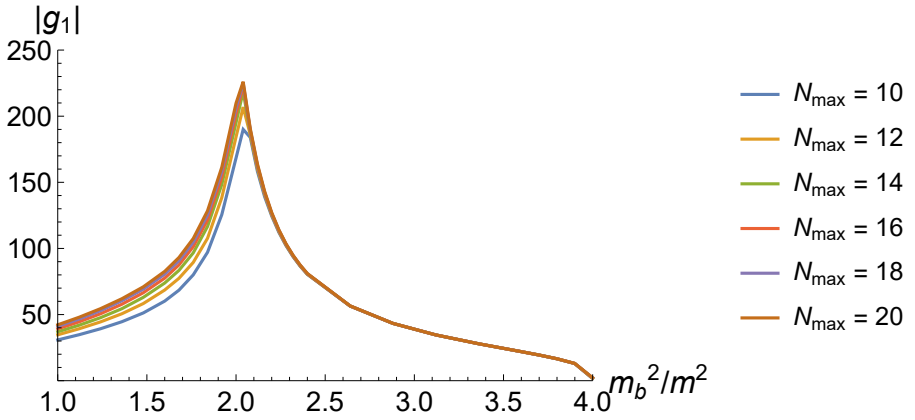

FIGURE 3.2: Maximization of g_1^2 as a function of m_1^2/m^2, in 4D, for various numerical cutoffs N_{max}. Unitarity was imposed along a uniform ρ-grid of 200 values, for $\ell \leq \ell_{max} = 20$.

details which differ in both cases. The most obvious feature is the contrasting behaviour of the convergence with N_{max} before and after the peak. For $m_1^2 > 2m^2$, $|g_1|$ seems to attain an optimal and stable behaviour with the increase of N_{max}, whereas it keeps growing for $m_1^2 < 2m^2$. There does not seem to be an obvious reason for this disparity, rather than the fact that it may have to do with some of the discussed shortcomings of the primal method.

Secondly, there is a crest for $m_1^2 \approx 2m^2$, a behaviour previously observed in 2D. Regarding the latter, the peak was the result of the collision of the s- and t- poles for $m_1^2 = 2m^2$, which left g_1^2 virtually unbounded and resulted in a divergence. However, it is not the case for 4D: by extrapolation (using, for example, the function `Fit` in `Mathematica`) it is possible to show that the peak stabilizes to a finite value rather than infinite. This is better understood when taking into account that constraints stemming from Equation 3.12 are being considered: $T(s, t(x))$ has, naturally, both a s- and t- pole for each bound-state; however, the latter is being integrated against Legendre polynomials (while the former is not), which means that its "strength" (which previously was $\propto (t - m_1^2)^{-1}$) decreases. In the end, both singularities have different "strengths", which does not result in cancellation and, thus, g_1^2 can still be bounded.

According to [19], near $m_1^2 \sim 4m^2$, g_1^2 must behave like $g_1^2 \sim 256\pi\sqrt{2 - m_1/m}$, which can be shown following the argument in [19]. Near $s = 4m^2$, we can think of the scattering process as the scattering of a particle of mass m which interacts with a similar one by the virtual exchanged particle of mass $m_b = 2m - \epsilon$, where ϵ is seen as a small binding energy

parameter. In this region [19]

$$M_{\text{pole}} = \frac{m^{5-d}g^2}{s-m_b^2} \sim \frac{m^{5-d}g^2/\epsilon}{4m(E/\epsilon+1)} \tag{3.14}$$

where E is the kinetic energy of the system in the centre of mass, which is taken to be small - just as ϵ. For $S_0(s)$ (s partial wave) it is shown that [19]

$$2^{3-d}m(m\epsilon)^{1-d/2}S_0^{\text{pole}}(E/\epsilon) \sim \frac{2^{1-2d}\pi^{1-d/2}}{\Gamma(d/2)}\frac{m^{5-d}g^2/\epsilon}{4m(E/\epsilon+1)} \tag{3.15}$$

where we focused on the $s=(2m^2-\epsilon)^2$ pole region. Thus, the non-relativistic version of the residue reads

$$g^2 \to 2^{4+d}\pi^{d/2-1}\Gamma(d/2)g_{\text{NR}}^2(\epsilon/m)^{2-d/2} \tag{3.16}$$

For $d=3$, one can show [19] that it should happen that $g_{\text{NR}}^2 < 2^2$. Thus,

$$g_{3+1}^2 \leq 2^8\pi\sqrt{\epsilon-m} = 256\pi\sqrt{2-m_b/m} \tag{3.17}$$

as proposed.

To check this claim, we went ahead and did the same optimization process as for other masses. However, this seemingly simple assignment turned out to be more arduous than expected, since the algorithm had a hard time converging to the expected solution: with the increase in N_{max}, there was still improvement in the target variable, for all of the tested parameters. The problem may have to do with singularities at the boundary which are not being accounted for (later introduced as *threshold singularity*), which are a greatly impediment for the fast convergence of the algorithm. To tackle this issue, it was cleverly suggested in [19] that the center of the $s \mapsto \rho_s$ map was changed, in that the bound-state always maps to the center of the ρ disk. Re-calculating the predetermined integrals of the partial-wave amplitudes so that they took this into account, we were successful in showing a great agreement between the numerical data and the analytical solution, as observed in Figure 3.3. Incredibly, for parameters as low as $N_{max}=2$ and $\ell_{max}=4$, an astonishing agreement is already visible, corroborating both the analytical result and the modification of the algorithm.

With this figure, we end the analysis of the cubic coupling maximization in 4D. In the preceding section, we shift our focus to another interesting target variable: the quartic coupling.

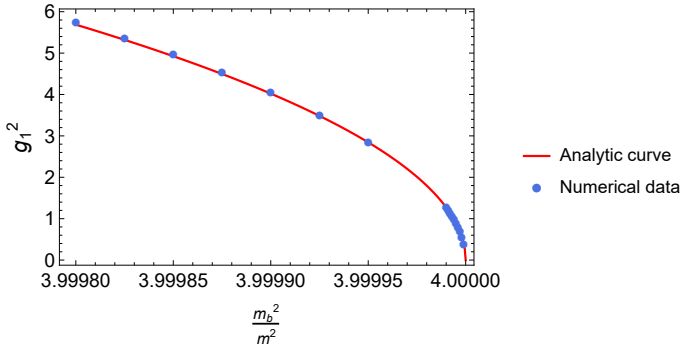

FIGURE 3.3: Maximization of g_1^2 as a function of m_1^2/m^2 near $4m^2$ vs. the analytical result $g_1^2 \sim 256\pi\sqrt{2 - m_1/m}$. For the plot, $N_{max} = 2$ and $\ell_{max} = 4$ were used.

3.4 Quartic coupling

3.4.1 Maximization

Our second and final target variable is commonly known as *quartic coupling* and, historically, it has been attributed to the coupling strength of the $\pi^0\pi^0$ scattering [39]. Mathematically, it conventionally corresponds to the value of the amplitude $T(s,t,u)$ (with no bound-states) at the crossing symmetric point $s = t = u = 4/3$ ($m_\pi = 1$), apart from a normalization constant stemming from our notation,

$$\lambda \equiv \frac{1}{32\pi} T\left(\frac{4}{3}, \frac{4}{3}, \frac{4}{3}\right) \tag{3.18}$$

The constraints on this coupling have been suffering constant changes since the 60's [19, 39–43], where [19] achieves the best results so far. In order to bracket the numerical solution, we consider the results from [39], obtained only axiomatically by Lopez and Mennessier, which impose that $-8.2 < \lambda < 2.75$. On the other hand, previous analytical works (using slightly different methods) [42] determine a lower but still rigorous bound on the amplitude, $\lambda < 2.62$, effectively introducing a region in which we must search the upper bound solution in, $\lambda \in [2.62, 2.75]$. Since these results were obtained from axiomatic conditions such as analyticity (not extended), crossing and unitarity, we do not expect to find a quartic coupling greater than what has been already found. It that is the case, then we know something went wrong.

Regarding the numerical routine, the Ansatz 3.10 can still be used, remembering that there are no bound-states and, therefore, g_1^2 should be set automatically to 0. We proceed with maximizing the new objective λ, subject to the unitarity condition 3.8.

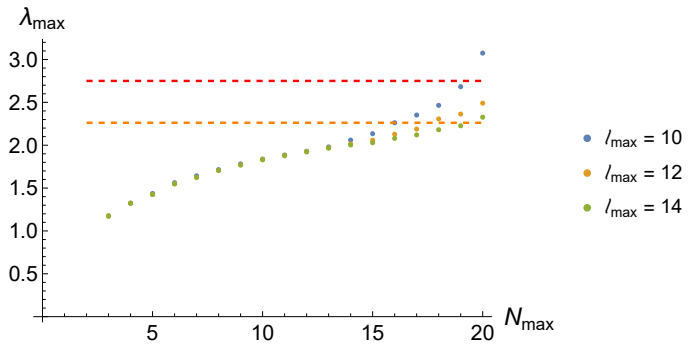

FIGURE 3.4: Maximization of λ as a function of N_{max}. Even for N_{max} as high as 20 and $\ell_{max} = 14$, the quartic coupling does not converge. The dashed lines illustrate the bounds $\lambda = 2.62$ (orange) and $\lambda = 2.75$ (red) found in [42] and [39], respectively.

The result of carrying out this process results in Figure 3.4, which clearly shows that the objective is far from converging to an optimal value. On the account of the fact that the ρ expansion is analytic inside the unit disk, the previous result suggest the presence of a singularity right in (or near) the circumference. In fact, according to [44], if $T(s,t)$ is to be maximized inside the Mandelstam triangle, it is necessary for its value to be maximal at the physical energy threshold, $s = 4m^2$. Such behaviour is reproduced by imposing a threshold "bound-state", as if it were a pole. In practical terms, these statements imply that a new term of the form

$$\alpha\left(\frac{1}{\rho_s - 1} + \frac{1}{\rho_t - 1} + \frac{1}{\rho_u - 1}\right) \tag{3.19}$$

should be added to the Ansatz in order the amplitude at $T\left(\frac{4}{3}, \frac{4}{3}, \frac{4}{3}\right)$. With the addition of this new term, the maximization routine takes place in the extended space $\{\alpha, \{\alpha_{abc}\}\}$, which should be taken into account when using SDPB. One way to check whether α attains a correct value after the optimization is to impose that [19]

$$|S_0(s)| < 1 \implies \text{Re}\, S_0(s) < 1 \tag{3.20}$$

In Appendix C, we show that this condition results in the much more simple requirement that

$$-32\sqrt{6}\pi \leq \alpha \leq 0. \tag{3.21}$$

Other partial-waves impose conditions which do not conflict with Equation 3.21. Thus, upon executing the optimization routine, one will probe whether α satisfies such inequalities. Numerically, unitarity is imposed on a uniform ρ grid of 200 points.

Figure 3.5 clearly shows that introducing the threshold pole greatly expedites the convergence of λ. The values that λ takes in the plateau, as a function of ℓ_{max}, are represented in Table 3.1: the results correspond to the mean taken over points with $N_{max} = 7$ until $N_{max} = 11$ (inner points in the plateau), while the error corresponds to the standard deviation of such points.

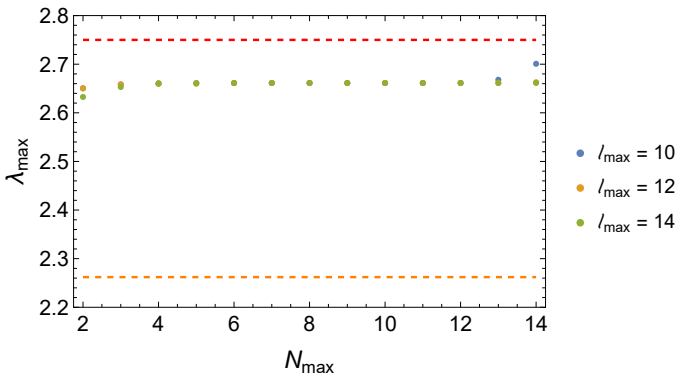

FIGURE 3.5: Maximization of λ as a function of N_{max}, for the modified Ansatz. Numerical data are presented by points; the red and green dashed lines represent the analytic boundaries. The quartic coupling stabilizes for $N_{max} \geq 6$, independently of ℓ_{max}. For $N_{max} \geq 13$, the plateau is lost again (there needs to be a balance between N_{max} and ℓ_{max} which need to happen for the algorithm to work; such balance is lost when N_{max} is greater than ℓ_{max}).

	$\ell_{max} = 10$	$\ell_{max} = 12$	$\ell_{max} = 14$
λ	2.661317 ± 0.000006	2.661316 ± 0.000006	2.661314 ± 0.000008

TABLE 3.1: Values of λ at the plateau. Each value corresponds to the mean of the values from $N_{max} = 7$ to $N_{max} = 11$, whereas the error is the standard deviation of such points.

Regarding the value of λ, it is clear from both the table and the figure that it falls in the interval $[2.62, 2.75]$, as predicted. Finally, we analyse the behaviour of the threshold pole coefficient, α, which is represented in Figure 3.6. As N_{max} increases, α saturates the lower bound previously imposed when analysing unitarity, $-32\pi\sqrt{6}$. If, however, the lower bound is saturated, it means that $S_0(s)$ (at the threshold) should saturate unitarity as well! In order to check if this is true, we plot the components of the S_0 partial-wave, which results in Figure 3.7. In fact, according to Figure 3.7 (B), it seems that unitarity is saturated for almost every value of s: upon a closer inspection of 3.7 (A), we conclude that this is only true in the limit where ℓ_{max} and N_{max} are high. The crucial aspect is that the region where unitarity is not saturated is pushed further into the high energies realm, which seems to be the case. Some of our results presented slight but measurable differences in regards to the original ones from [19] due to the numerical computation of

the integrals. Even though, for our purposes, such results suffice, precise measurements should only be obtained if the integrals are determined analytically.

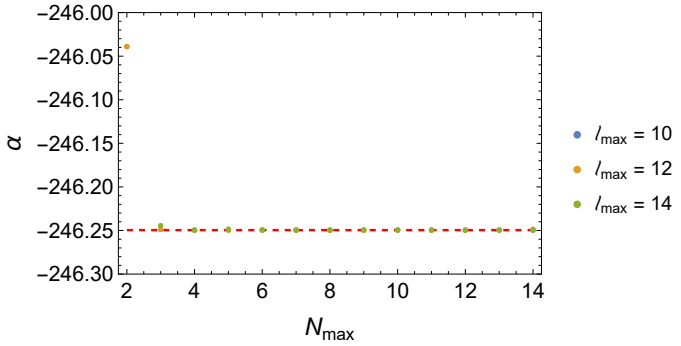

FIGURE 3.6: Evolution of the threshold pole coefficient as a function of N_{max} and ℓ_{max}. The dots correspond to numerical data, while the red dashed line is the lowest allowed value for α. For $N_{max} \geq 4$, this coefficient attains a constant value which saturates the lower theoretical bound. This plateau seems to be independent of ℓ_{max}.

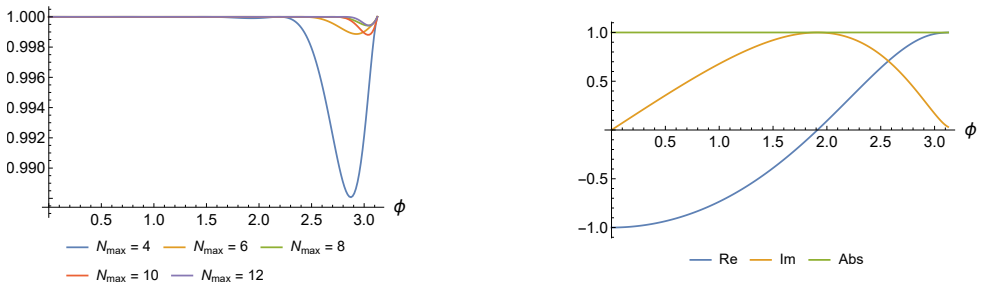

(A) (B)

FIGURE 3.7: (A) The absolute value of S_0 for several N_{max} vs. (B) the S-matrix components of S_0 for $N_{max} = 12$, as function of ϕ (such that $\rho = e^{i\times\phi}$).

Lastly, we would like to show that using such a small number of partial-waves yields an accurate result, in massive theories, when compared to massless theories where the partial waves go as far as $\ell_{max} = 90$ or even $\ell_{max} = 220$ [45, 46]. That being said, let us recall the Yukawa model for interaction. For nonrelativistic scattering, the S-matrix elements can be written in terms of the Yukawa potential function [47],

$$\langle p'|iT|p\rangle = -i\tilde{V}(\mathbf{q})(2\pi)\delta(E_{\mathbf{p}'} - E_{\mathbf{p}}), \quad \mathbf{q} = \mathbf{p}' - \mathbf{p} \tag{3.22}$$

where

$$\tilde{V}(\mathbf{q}) = \frac{1}{V}\int d^3x\, V(\mathbf{r})e^{-i\mathbf{q}\cdot\mathbf{r}} = \langle \mathbf{p}'|V(\mathbf{r})|\mathbf{p}\rangle \tag{3.23}$$

Since

$$\tilde{V}(\mathbf{q}) = -\frac{g^2}{|\mathbf{q}|^2 + m_\phi^2} \tag{3.24}$$

for a ϕ fermion field, then

$$V(r) = -\frac{g^2}{4\pi}\frac{1}{r}e^{-m_\phi r} \tag{3.25}$$

When the fermion is a spinless scalar, one can think of the angular momentum as the sole momentum relevant to the system. In the classical limit, $\vec{l} = \vec{r} \times \vec{p}$, which means $\ell = b \times p$, where b is the impact parameter between both particles. Using this result, we can re-write Equation 3.25 as

$$\begin{aligned} V(r) &= -\frac{g^2}{4\pi}\frac{1}{r}e^{-m_\phi r} \\ &\approx -\frac{g^2}{4\pi}\frac{1}{r}e^{-m_\phi \frac{\ell}{E_p}} \end{aligned} \tag{3.26}$$

which means that the potential decays with ℓ. Thus, for increasing ℓ, the S-matrix element should become increasingly irrelevant. In other words, only low spin partial-waves contribute should contribute to the expansion! For $\ell = 12$, the imaginary part of the partial-wave component S_{12} is practically negligible, as can be checked in Figure 3.8

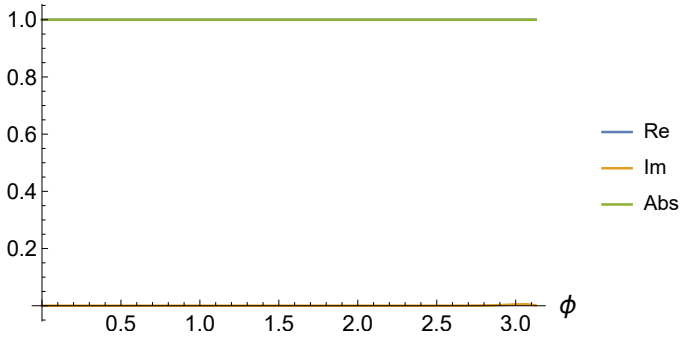

FIGURE 3.8: Components of the S-matrix partial-wave S_{12}. The real part saturates unitarity, while the imaginary part is zero for all $\rho = e^{i\times\phi}$.

With these comments, we close the subsection on the maximization of the quartic coupling. In regards to the minimum of the quartic coupling, there are still analytical results which can be verified. Thus, it would be interesting to check whether, numerically, this bounds are satisfied and if a better one can be found. Such will be the task of the next and final subsection of 4D elastic scattering.

3.4.2 Minimization

Instead of maximizing λ, we wish to find its lower bound. However, the SDPB program maximizes objectives; hence, one should be careful and set the objective to $-\lambda$ and plot whichever result obtained and multiply it by (-1).

One must exert some caution: the objective to maximize is $\propto -T\left(\frac{4}{3},\frac{4}{3},\frac{4}{3}\right)$, which, using the threshold pole term, results in

$$\begin{aligned} -T\left(\frac{4}{3},\frac{4}{3},\frac{4}{3}\right) &= 3\alpha - \sum_{a,b,c=0} \alpha_{abc}\,\rho_s^a \rho_t^b \rho_u^c \Big|_{s=\frac{4}{3},\,t=\frac{4}{3},\,u=\frac{4}{3}} \\ &= 3\alpha - \alpha_{000} \end{aligned} \tag{3.27}$$

To achieve the highest possible value would mean to force $\alpha > 0$, which is impossible due to Equation 3.21. Hence, such term should be discarded.

As it is, the algorithm does not converge well, as is clear from Figure 3.9, even for higher spin partial-waves. The solution would be to identify relevant singular behaviours slowing down the convergence. However, up until now and to our knowledge, no such behaviour was found. Even if the values seem far from reaching a plateau, so far they seem to be right within the expected lower bound.

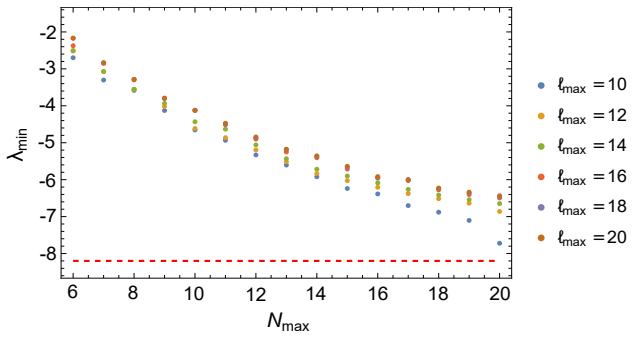

FIGURE 3.9: Minimization of λ as a function of N_{max}. The red dashed line corresponds to the analytic lower bound, -8.2. Convergence seems difficult even for higher spin partial-waves.

This ends the study of the scattering of massive, spinless particles in 2D and 4D. Throughout the previous chapters, no particle production was considered. What would change in all the preceding results if, say, some inelastic profile was considered? This is the premise of the following chapters, where various original results will be presented.

Chapter 4

Inelastic scattering: massive scalar particles

4.1 2D Inelastic scattering, primal

4.1.1 Introduction and numerical Ansatz

So far, we have been avoiding particle production. This has the more immediate consequence that unitarity is simply written as $|S(s)|^2 \leq 1$ or $|S_\ell(s)|^2 \leq 1$, for 2D and 4D respectively. If allowing for particle production, the previous expressions still apply, but we can do better: stronger conditions must be imposed. It can be done in a plethora of ways, c.f. Equation 3.7, in particular it may as well be probed by $2 \to n$ (in particular $2 \to 4$) amplitude functions, which is usually harder to analyse. The objective of his section is to implement such conditions by hand, imposing specific inelastic profiles, which is a more direct approach. As far as we know, this is the first time such approaches are being presented.

To start our journey into inelasticity, we specialize in the 2D scattering of massive, spinless and identical particles of mass m. This scattering allows for the creation of bound-states of mass m_i $\{m < m_1 < ... < m_N\}$ and particle production for $s > 16m^2$, assuming that the lightest particles are $\mathbb{Z}_2$ odd. Without loss of generality, $m = 1$.

The S-matrix describing this process must be crossing symmetric, as usual

$$S(s) = S(4 - s) \tag{4.1}$$

It is still possible to define $S(s) = 1 + i\frac{T(s)}{2\sqrt{s(s-4m^2)}}$, which means that unitarity takes the form

$$|S(s)|^2 \leq \beta(s), \quad \beta(s) \geq 0; \qquad \beta(s) = \begin{cases} 1, & 4 \leq s \leq 16 \\ \text{profile(s)} & s > 16 \end{cases} \tag{4.2}$$

where the profile is yet to be chosen. Other aspects pertaining to real analiticity and the analytical structure of the amplitude function remain unaltered from subsection 2.1.2, and thus an Ansatz can start to be envisioned.

Proven to be more versatile, the double ρ expansion Ansatz 2.18 shall be used, here for reference

$$S(s,t) = -J_\rho \times \left[\frac{g_\rho^2}{\rho(s) - \rho(m_1^2)} + \frac{g_\rho^2}{\rho(t) - \rho(m_1^2)}\right] + \sum_{a,b=0}^{\infty} c_{ab}\ \rho_s^a \rho_t^b \tag{4.3}$$

where

$$s \mapsto \rho_s = \frac{\sqrt{4 - s_0} - \sqrt{4 - s}}{\sqrt{4 - s_0} + \sqrt{4 - s}}, \qquad s = \frac{s_0(1-\rho_s)^2 + 16\rho_s}{(1+\rho_s)^2} \tag{4.4}$$

and $s_0 = 2$. At the same time, we impose a numerical cutoff $a \leq N_{max}$ and $b \leq N_{max}$. Furthermore, unitarity is evaluated at the grid $s(n)_i = 4 + 100 \times \left(\frac{i}{n}\right)^2$, $i \in \{1, 2, ..., n\}$ for $n = 100$ points.

Throughout this chapter, only two $\beta(s)$ profiles will be considered:

$$\beta_1(s) = \begin{cases} 1, & 4 \leq s \leq 16 \\ 1 - \alpha & s > 16 \end{cases} \tag{4.5}$$

and

$$\beta_2(s)^* = \begin{cases} 1, & 4 \leq s \leq 16 \\ e^{-\sqrt{s-16}\times\alpha} & s > 16 \end{cases} \tag{4.6}$$

where $0 < \alpha \leq 1$ is a constant. While the first profile is a bit more pedagogical than physical, the second one tries to recreate the creation of a black holes by means of scattering of particles (in this case, a toy model is being considered, since gravitons are massless particles with spin).

Before proceeding with the numerical analysis, there is the question of the analytical solution that need to be addressed. For that matter, [3, 26, 48] provide several ways of

*This profile, with the square root, would actually corresponds to the 3D case. In 4D, the exponential profile linear in the energy s is troublesome, seeing as the analytical expression is not well defined. The 2D profile is ill-defined.

checking out our solutions, of which [48] is the one which suits us best:

$$S(s) = S_{\text{elastic}}(s)\, e^{-\int_4^\infty \frac{ds'}{2\pi i} \log(\beta(s)) \sqrt{\frac{s(s-4)}{s'(s'-4)}} \left(\frac{1}{s'-s} + \frac{1}{s'-(4-s)}\right)} \tag{4.7}$$

and $|S_{\text{elastic}}(s)| = 1$ is a purely elastic S-matrix which is the product of CDD factors, as seen in subsection 2.1.6.

With this, we are prepared to start producing results.

4.1.2 Maximization of the cubic coupling

The maximization routine is extremely similar to that of the elastic 2D case. First, a study of the convergence of g_1^2 with N_{max} was made, in order to determine what the best parameters were. At the same time, convergence plots were made for various quantities such that Re $S(6)$, Re $S(14)$, Re $S(17)$ and Re $S(30)$, so as to understand if the S-matrix components converged as well. What was concluded was that while the coupling converged pretty well and corresponded to the analytical value, the components struggled to stabilize. Nonetheless, the best parameters found in these conditions were $N_{max} = 5$ for both profiles $\beta_1(s)$ and $\beta_2(s)$.

Instead of the usual logarithmic plot of g_1^2 vs m_1^2, the relative error between the analytical and the numerical solutions is of more use, since the change in the curves for different values of α is rather imperceptible. Figures 4.1 and 4.2 provide some insightful key features which may be worth exploring.

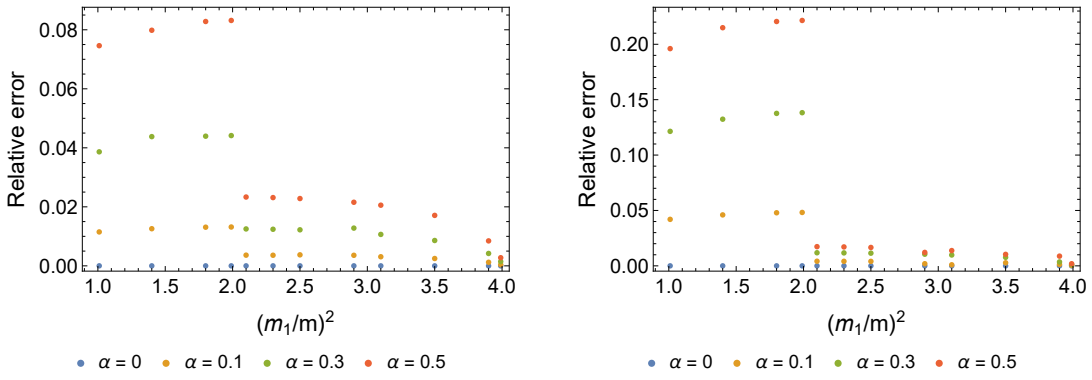

(A) (B)

FIGURE 4.1: Relative error of the numerical data vs. the analytical solution 4.7, for the (A) β_1 profile and (B) β_2 profile. In both cases, $N_{max} = 5$.

The main feature that stands out in Figure 4.1 is the striking difference in the convergence for $m_1^2 < 2$ and $m_1^2 > 2$: in the former case, convergence seems tougher. Although

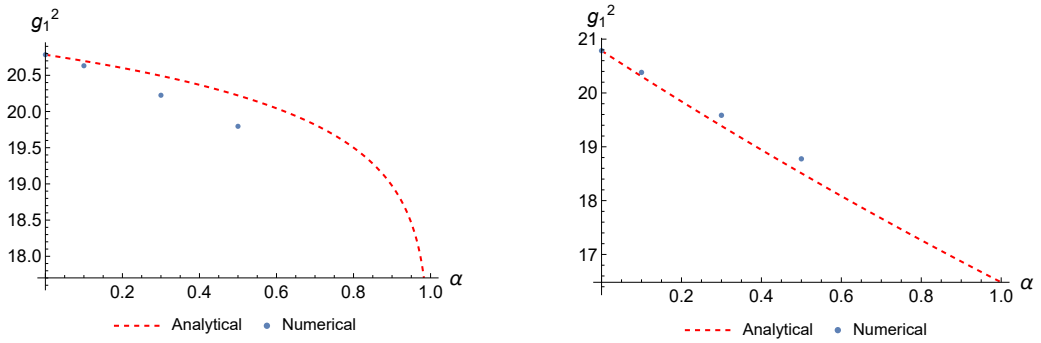

(A) (B)

FIGURE 4.2: Direct comparison between (A) profile β_1 or (B) profile β_2 and the analytical results. The bound-state mass is fixed, $m_1^2 = 3$.

we have not yet understood why this is the case, some investigation showed that it is found in other contexts [19, 33], as well as in section 3.3 in this dissertation.

Another key detail is the fact that, according to both figures, the increase in α results in the increase of the relative error. Intuitively, this may be attributed to the fact that the discontinuity in $s = 16$ is stronger the higher the value of α is: in turn, it is expected that a simple Ansatz with no singular behaviour in that region has an increasing difficulty in converging.

Lastly, the relative errors seem higher in profile β_2 rather than in β_1. In fact, in Figure 4.2, numerical data is above the analytical, which leads us to believe that either the algorithm is highly unstable or that the chosen Ansatz is not the most appropriate one for the problem at hand.

In order to corroborate the last point, we propose to plot the S-matrix components for, for instance, $\alpha = 0.5$. Usually, one would not show such inaccurate and unstable plots, but this time it may be beneficial in order to understand how improve the Ansatz. To that matter, Figure 4.3 shows the comparison between the numerical S-matrix components and the analytical ones. An obvious issue is that, even though the cubic coupling may have converged already, the S-matrix components are still very far from stabilizing. Moreover, one of the more important features is missing in both plots: the discontinuities in the $s = 16m^2$ region.

These comments close our brief study of the maximization of the cubic coupling subject to inelasticity. As anticipated, the Ansatz did not perform well: it was expected, since it does not have the appropriate discontinuities at $s = 16m^2$. This was predominantly visible in the S-matrix components, where there it is clear that said region is the more

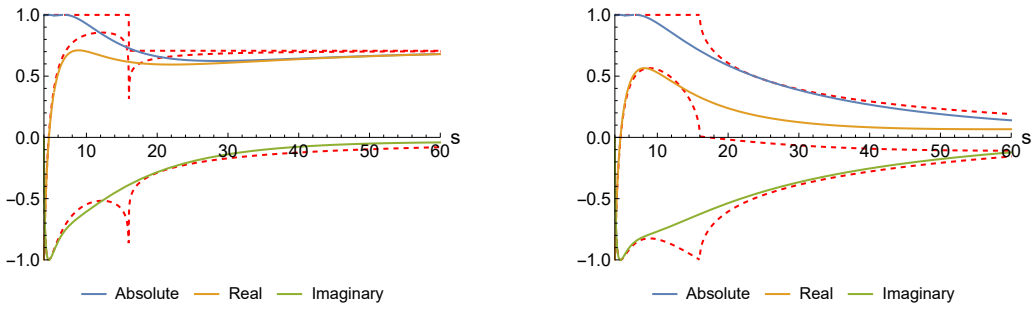

(A) (B)

FIGURE 4.3: S-matrix components for the inelastic profiles (A) β_1 and (B) β_2, when $\alpha = 0.5$ and $N_{max} = 5$ (best parameter) vs. the analytical results in red dashes lines.

problematic for the algorithm. However, before trying to solve this issue, we probe how far this simple Ansatz can go by exploring, for instance, max $S(2)$ and max $S(2)$ vs. α.

4.1.3 $S(2)$ vs. α

The aim of this section is to understand how $S(2)$ behaves when α is changed, for the case when $g_1^2 = 0$. For $\alpha = 0$, we must get that $S_{max}(2) = +1$ whereas $S_{min}(2) = -1$, as seen previously on Figure 2.19.

This is a rather straightforward optimization problem, with the only change that the new objective is to maximize and minimize $S(2)$. In order to do so, `FindMinimum` and `FindMaximum` from `Mathematica` are used, which results in Figures 4.4 and 4.5

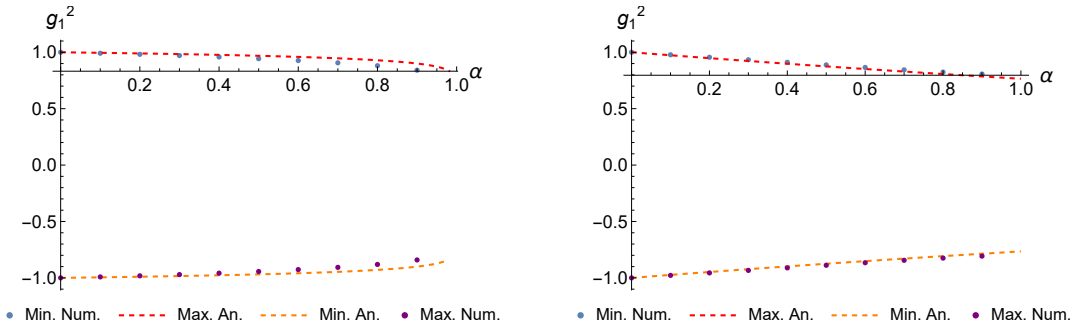

(A) (B)

FIGURE 4.4: max $S(2)$ and min $S(2)$ vs. α vs. the analytical solution 4.7 (red dashed lines), for the (A) β_1 profile and (B) β_2 profile. In both cases, $N_{max} = 5$.

For small values of α, the numerical data closely follow the trend set by the analytical solution. For the profile β_1, however, increasing α results in successively larger disparities when compared with theoretical results, which can be clearly checked in Figure 4.5 (A). On the contrary, in the second case, the discrepancies remain almost negligible (cfe. Figure

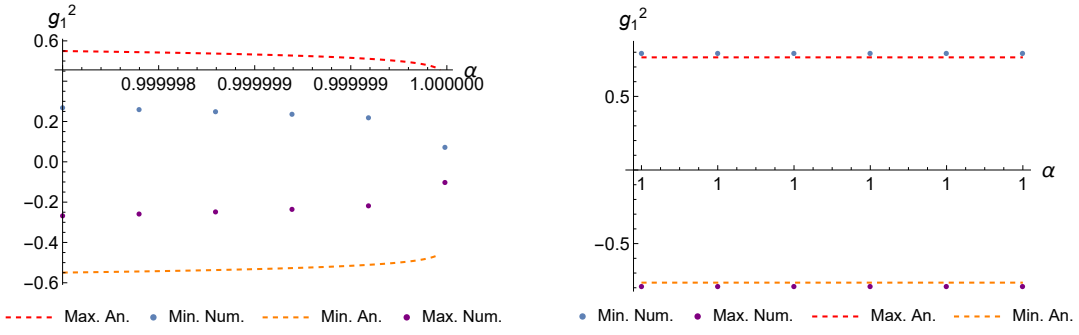

(A) (B)

FIGURE 4.5: $\max S(2)$ and $\min S(2)$ vs. α vs. the analytical solution 4.7 (red dashed lines), for the (A) β_1 profile and (B) β_2 profile and near $\alpha = 1$. In both cases, $N_{max} = 5$.

4.5 (B)). In the limit where $\alpha \to 1$, $\beta_1 \to 0$ and $S(2) \to 0$. On the other hand, $\beta_2 \to 1$ implies that $S(2) \to 0.76521$, approximately. The numerical data seems to agree with such values, which can be easily confirmed by taking the value of the last evaluated point in both numerical curves (maximum and minimum curves).

It is fairly clear by now that our results suffer from setbacks due to the Ansatz 4.3. All things considered, in the next section we try to adapt this Ansatz to the new behaviours, in search of better agreements between our data and the proposed solutions.

4.1.4 Ansatz modification: ρ_{16} addition

As the title suggests, the simplest approach one can take to introduce discontinuities is to expand the basis used in the Ansatz formulation, so as to capture the singular behaviour. In this case, we aim to reproduce a sharp discontinuity at $s = 16m^2$, precisely, without compromising analyticity. This last requirement is harder to fulfil, which is why we must recall the analytical structure so far imposed. Let $m^2 = 1$.

When describing the analyticity of the amplitude function, extended analyticity was considered. In this regard, only simple poles - corresponding to bound-states - and cuts - corresponding to the physical energy region - were considered. Since the discontinuities are located in the region $s > 4m^2$, it seems more natural to look for terms which introduce cuts. Since we wish to impose the singularity at $s = 16m^2$, the obvious choice is to modify the definition of ρ_s so the cut starts at said position instead of $s = 4m^2$: this is what was named the ρ_{16} term, completely new to the literature. In practice, several such terms will be considered similarly to the $\rho_s \times \rho_t$ expansion previously made.

To start with, we construct the explicit form of ρ_{16}. The requirements are that it introduces a cut in the s- and t-plane for $s > 16$ and $t > 16$ and, by choice, that it is 0 when $s = 2 = t$. The last requirement will become clear shortly. Both conditions are met by the map

$$\rho_{16,s}(s) \equiv \frac{\sqrt{16 - s_0} - \sqrt{16 - s}}{\sqrt{16 - s_0} + \sqrt{16 - s}}, \qquad s = \frac{2(1 + 30\rho_{16,s} + \rho_{16,s}^2)}{(1 + \rho_{16,s})^2} \tag{4.8}$$

with $s_0 = 2$. It can be checked that s maps to a unit disk, where $s = 2$ corresponds to $\rho = 0$, as demanded.

Thus, our new Ansatz should read

$$S(s,t) = -J_\rho \times \left[\frac{g_\rho^2}{\rho(s) - \rho(m_1^2)} + \frac{g_\rho^2}{\rho(t) - \rho(m_1^2)} \right] + \sum_{a,b=0}^{\infty} c_{ab}\ \rho_s^a \rho_t^b + \sum_{a,b=0}^{\infty} d_{ab}\ \rho_{16,s}^a \rho_{16,t}^b \text{*} \tag{4.9}$$

However, there are still terms which are redundant, since $S(s,t)$ must still satisfy crossing symmetry. This symmetry is imposed directly in the coefficients d_{ab}, such that $d_{ab} = d_{ba}$. In turn, it means that some coefficients can be set to 0, like in subsection 2.1.5. It is now clear why we imposed that $s_0 = 2$ in Equation 4.8: using the inverse map, $s(\rho_{16,s})$ it can be checked that $s + t = 4$ ($u = 0$ in 2D) corresponds to

$$\rho_{16,s} + \rho_{16,t} + 4\rho_{16,s}\rho_{16,t} + \rho_{16,s}^2\rho_{16,t} + \rho_{16,s}\rho_{16,t}^2 = 0 \tag{4.10}$$

which is mathematically equivalent to Equation 2.19. This means that the coefficients therein eliminated are can be discarded as well here. Apart from this, no other mathematical consideration needs to be done. Regarding the numerical aspect, the usual problem of the maximization of the cubic coupling subject to unitarity and crossing symmetry is considered. To do so, we impose two numerical cutoffs, N_{max}^c and N_{max}^d, which correspond to the terms with c_{ab} and d_{ab} coefficients, respectively. Unitarity is imposed for $n = 50$ points using the grid $s(n)_i = 4 + 100 \times \left(\frac{i}{n}\right)^2$, $i \in \{1, 2, ..., n\}$ and only the profile β_1 is considered.

Upon using `Mathematica`'s `FindMaximum` tool with `InteriorPoint` as the search `Method`, for 2000 `MaxIterations`, we proceeded with the study of the best parameters of convergence, starting with N_{max}^c near the best value for the case when N_{max}^c did not exist. As such, for $N_{max}^c = 5$, $N_{max}^d = 2$ was found to be the best parameter, choosing $d_{00} = 0$. Apart from being redundant, seeing as c_{00} is a constant as well, when included, the d_{00}

*Strictly speaking, when these sums are infinite, the c_{ab} and d_{ab} coefficients are not independent: ρ_{16} can be expressed as a sum of infinite ρ terms. Since, numerically, cutoffs are introduced in both sums, this ambiguity disappears.

term greatly destabilized the final results. This choice of parameters yielded Figures 4.6 and 4.7. Astonishingly, for the β_1 profile, the relative error noticed small yet noticeable improvement! With such an improvement in the target variable, one would anticipate some progress in the S-matrix components. To check so, the S-matrix components - for the same set o parameters as before - are plotted in Figure 4.8. Even though the high energy behaviour leaves much to be desired, the discontinuity seems better described than before - a clear progress.

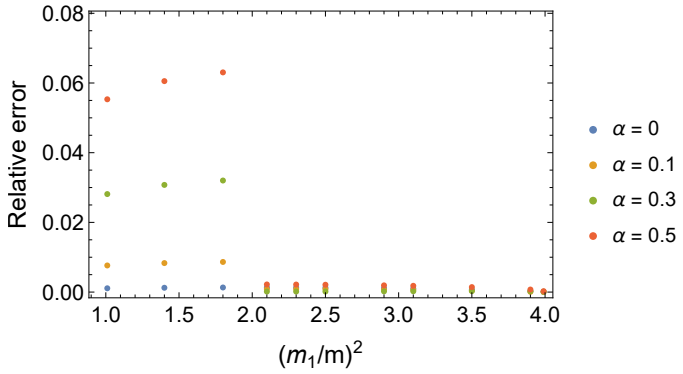

FIGURE 4.6: Relative error of the numerical data vs. the analytical solution 4.7, for the β_1 profile. Here, the parameters used were $N^c_{max} = 5$ and $N^d_{max} = 2$.

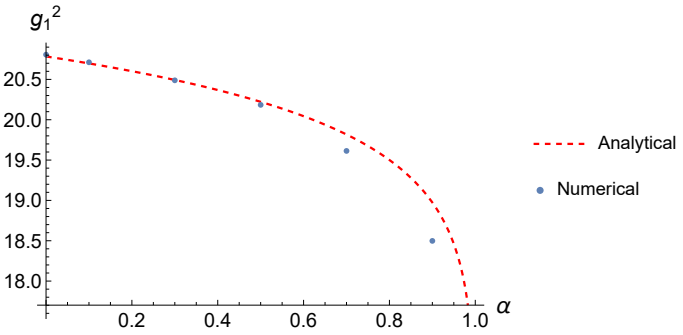

FIGURE 4.7: Direct comparison between the profile β_1 and the analytical results. The bound-state mass is fixed, $m_1^2 = 3$, $N^c_{max} = 5$ and $N^d_{max} = 2$.

We end this section with some comments. Most of the results obtained previously used an optimization tool which, in all fairness, is like a "black box", in that we do not fully understand, from the mathematical point of view, what is happening during the optimization process. That is perhaps one of the main reasons why the primal method, as was done here, is not adequate for the task at hand. In the future, we would certainly like to carry out this section using the SDPB approach: it is expected that the results see a great improvement over those in this section.

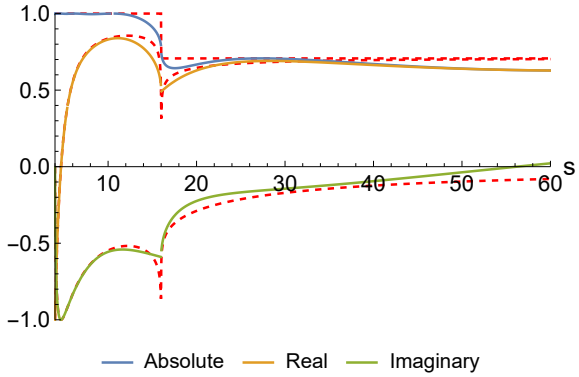

FIGURE 4.8: S-matrix components for the inelastic profile β_1 and with the new Ansatz 4.9. In red are the components of the analytical solution. Here, the parameters used were $m_1^2 = 3$, $N_{max}^c = 5$ and $N_{max}^d = 2$ and $\alpha = 0.5$.

However, this is not the end of the line. There is still another method one can use: the dual approach. In the next section, we explore this well-known method.

4.2 2D Inelastic scattering, dual

The previous section focused on building up a theory from the ground, using axiomatic constraints and, eventually, different Ansatz which provided for a better space of functionals and, consequently, a better solution. However, we already used another method which ruled out potential functions: the dual approach. It may be more fruitful to carry out that same approach in this case, were an adequate Ansatz for the primal method was hard to find.

Although this formalism is more intricate and complicated than the primal method, it was already carried out once in section 2.2 with great success. Hence, we try to follow the same steps therein taken. Firstly, we recall that unitarity takes the form of Equation 4.2. Thus, the primal optimization problem is

$$\underset{\{T(s),\, g_1^2\}}{\text{maximize}} \quad g_1^2 \tag{4.11}$$

subject to the constraints

$$\mathcal{A}(s) \equiv T(s) - \left(T_\infty - \frac{g_1^2}{s - m_1^2} + \int_{4m^2}^{\infty} \frac{dz}{\pi} \frac{\operatorname{Im} T(z)}{s - z + i0^+} + (s \leftrightarrow 4m^2 - s) \right) = 0, \quad s \geq 4m^2 \tag{4.12}$$

and the new unitarity condition, which is showed in Appendix D to be

$$\mathcal{U}(s) \equiv 2\sqrt{s(s-4)}\,\big(1 - \beta(s)\big) + 2 \operatorname{Im} T(s) - \frac{1}{2\sqrt{s(s-4)}} |T(s)|^2 \geq 0 \tag{4.13}$$

The second step is to build the Lagrangian density $\mathcal{L}(T, \omega, \lambda)$,

$$\mathcal{L}(T, \omega, \lambda) = g_1^2 + \int_{4m^2}^{\infty} ds\, \omega(s) \mathcal{A}(s) + \lambda(s) \mathcal{U}(s) \tag{4.14}$$

where $\lambda \geq 0$. Using the Weak Duality principle and the same definition for $W(s)$, which does not depend on the form of the unitarity condition, we arrive at the expression

$$\mathcal{L}(T, \omega, \lambda) = \int_{4m^2}^{\infty} ds \operatorname{Im}\big[W(s) T(s)\big] + \lambda(s) \mathcal{U}(s) \tag{4.15}$$

provided that $\operatorname{Re} W(m_1^2) = -\frac{1}{\pi}$. Taking the remaining steps as was done in the aforementioned section, we show in Appendix D that the correct dual optimization problem is

$$\underset{\{W(s)\}}{\text{minimize}} \quad D(W) = \int_{4m^2}^{\infty} ds\, \big[|W(s)|\beta(s) + \operatorname{Re} W(s)\big] \frac{1}{\rho_{11}^2(s)} \tag{4.16}$$

subject to the condition that

$$W(m_1^2) = -\frac{1}{\pi} \tag{4.17}$$

where $\beta(s)$ are the profiles used in subsection 4.1.1.

Lastly, it is necessary to propose an Ansatz to carry out numerical procedures. `FindMinimum` can still be used, as well as the $\rho(s)$ foliation

$$\rho(s) = \frac{\sqrt{2m^2} - \sqrt{4m^2 - s}}{\sqrt{2m^2} + \sqrt{4m^2 - s}} \tag{4.18}$$

and the same Ansatz as before

$$W(s) = \frac{1}{s(4m^2 - s)} \sum_{n=1}^{N_{max}} a_n(\rho(s)^n - \rho(t)^n) \tag{4.19}$$

where N_{max} is the numerical cutoff. The fact that the same Ansatz was used even though the S-matrix are not the same as before may seem a bit strange. However, the dual objective function encodes a discontinuity through $\beta(s)$, which takes care of said problem. Moreover, the results we are about to show corroborate that the Ansatz is appropriate.

Before proceeding with the final results, it is necessary to perform a convergence study. We found out that the study of the convergence of D with N_{max} sufficed, which is plotted in Figures 4.9 and 4.10, for both profiles and different values of α.

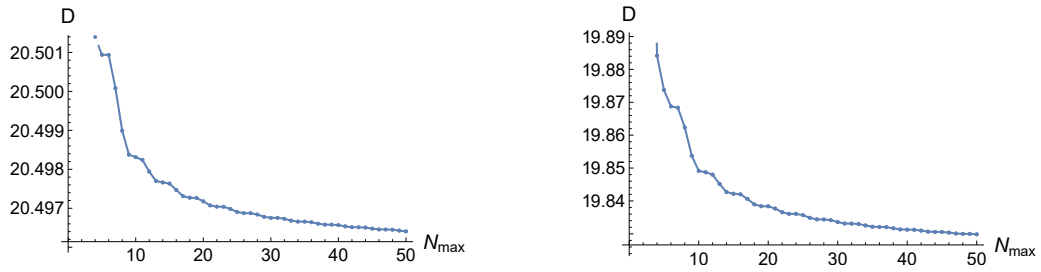

(A) (B)

FIGURE 4.9: Convergence of D vs N_{max}, for the β_1 profile and (A) $\alpha = 0.3$ or (B) $\alpha = 0.7$.

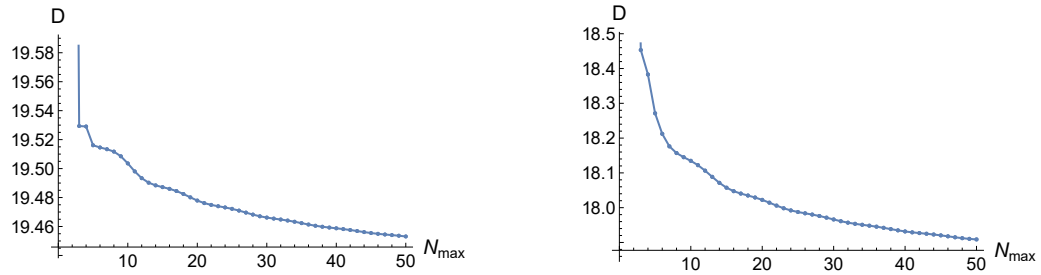

(A) (B)

FIGURE 4.10: Convergence of D vs N_{max}, for the β_2 profile and (A) $\alpha = 0.3$ or (B) $\alpha = 0.7$.

It is painfully evident that the dual objective is still far from converging. In fact, it was verified that it only fully converged for $\alpha = 0$, which is the maximization problem of of section 2.2. However, all of the curves appear to tend to a finite value, which could justify extrapolation. Based on this, we proceeded in two manners: both `Fit` and `NonlinearModelFit` are used to fit the data for an array of $\alpha \in \{0.3, 0.5, 0.7\}$, for both profiles β_1 and β_2. To this estimates we add an error which is determined in a similar fashion to what is done in Appendix H of [45]: let

$$\left(\chi^{(n)}\right)^2 = \frac{1}{m}\sum_{j=1}^{m}\left(\text{fit}^{(n)}(\text{estimate}_j) - \text{data point}_j\right)^2 \tag{4.20}$$

where m is the number of points used for each fit and $\text{fit}^{(n)}$ corresponds to a determined fit, for fixed α. Since `Fit` and `NonlinearModelFit` yielded similar results, we proceeded with using only the latter with a basis $\{\{a + b/x\}, \{a + b/x + c/x^2\}, \{a + b/x + c/x^2 + d/x^3\}, \{a + b/x + c/x^2 + d/x^3 + e/x^4\}, \{a + b/x^\beta\}\}$. Considering that

$$\sigma_{\text{estimate}} = \frac{\sum_n a^{(n)} / \left(\chi^{(n)}\right)^2}{\sum_n 1/\left(\chi^{(n)}\right)^2} \tag{4.21}$$

and

$$\sigma^2 = \frac{\sum_n \left(a^{(n)} - \sigma_{\text{estimate}}\right)^2 / \left(\chi^{(n)}\right)^2}{\sum_n 1/\left(\chi^{(n)}\right)^2} \tag{4.22}$$

where in both equations $a^{(n)}$ is the value of the parameter a for each of the fits $f^{(n)}$. All in all, the final values are presented in the Table 4.1,

	$\alpha = 0.3$	$\alpha = 0.5$	$\alpha = 0.7$
β_1	20.4959 ± 0.0002	20.2267 ± 0.0005	19.8230 ± 0.0016
β_2	19.42 ± 0.01	18.57 ± 0.03	17.79 ± 0.02

TABLE 4.1: Results of conducting the extrapolation method for both profiles.

Graphically, Figure 4.11 shows the comparison between the numerical data, with the corresponding error bars, and the analytical values. Moreover, Figure 4.12 shows, for both profiles, a more comprehensive understanding of where the extrapolation result falls, when compared to the analytical one, for $\alpha = 0.5$, as an example.

At this point, only the figures similar to 4.6 and 4.8 are missing. To solve this, we start by presenting Figure 4.13

Compared with Figure 4.6, Figure 4.13 (A) seems to perform considerably better, which was to be expected considering that the dual approach seems fairly more stable.

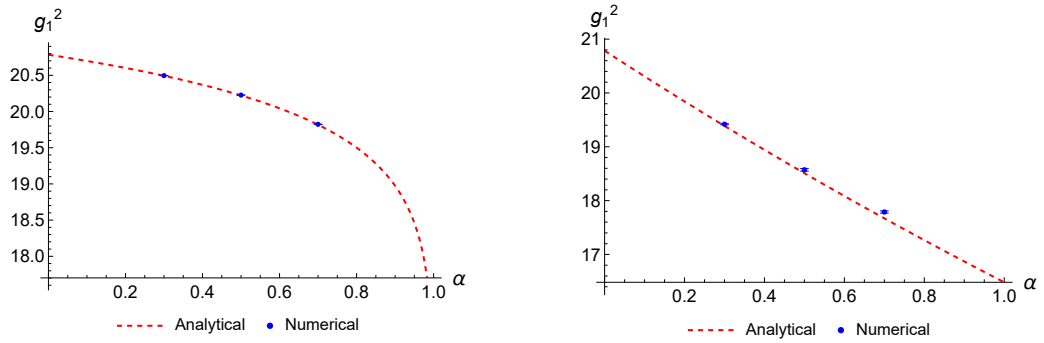

(A) (B)

FIGURE 4.11: Comparison between the analytical via Equation 4.7 vs. the data in Table 4.1 for (A) β_1 and (B) β_2.

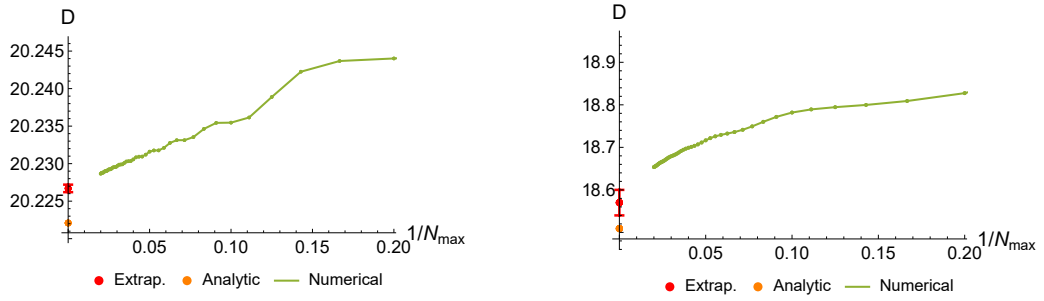

(A) (B)

FIGURE 4.12: $1/N_{max}$ vs. D, with the analytical and extrapolation values for profiles (A) β_1 and (B) β_2, when $\alpha = 0.5$.

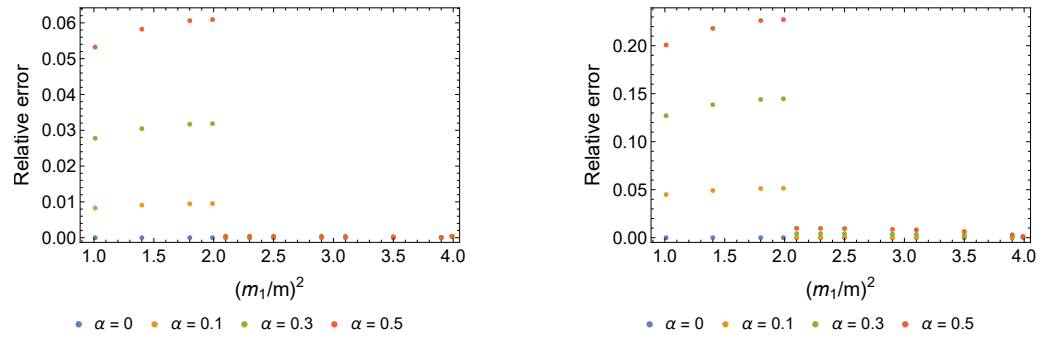

(A) (B)

FIGURE 4.13: Relative error of the numerical data vs. the analytical solution, for the (A) β_1 profile and (B) β_2 profile. In both cases, $N_{max} = 40$.

Lastly, we plot the S-matrix components for fixed m_1^2. To do so, we propose the modification to Equation 2.52, which should take the form

$$T_c^*(s) = \frac{i}{\rho_{11}^2(s)}\left(1 + \frac{W^*(s)}{|W(s)|}\sqrt{\beta(s)}\right) \tag{4.23}$$

With this, Figure 4.14 is presented. Although some oscillations still occur, the overall

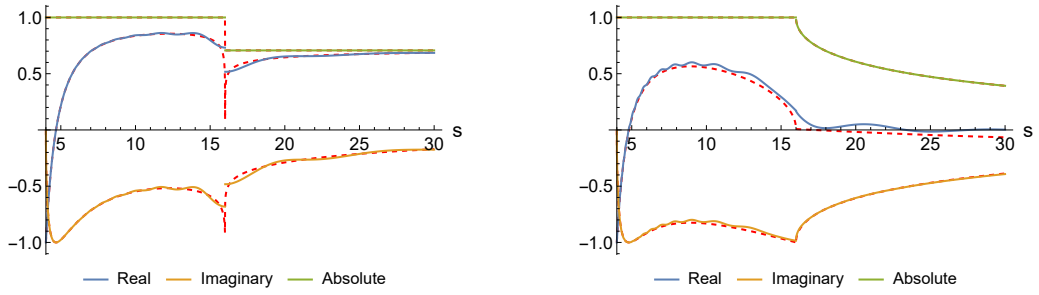

(A) (B)

FIGURE 4.14: S-matrix components for the inelastic profile (A) β_1 and (B) β_2 for the dual approach vs. the analytical components, red dashed curves. $m_1^2 = 3$, $N_{max} = 40$ and $\alpha = 0.5$ were used.

result is much better than those obtained from the primal approach, even with the ρ_{16} addition. Thus, both the dual and the primal approach seem to close the duality gap, hence yielding similar results. However, we can with confidence conclude that the dual approach is much more robust.

Unfortunately, the dual for the $S(2)$ maximization/minimization problem could not be found, hence the best results we have to show are those of the primal method. With this last comment we close the exploration of inelasticity in 2D, and proceed with the natural generalization for 4D.

4.3 4D Inelastic scattering, primal

As the title suggests, the aim of this section is to delve into the realm of 4D inelastic scattering. Much like the previous sections, particle production will be implemented directly using some profiles, but, since SDPB is used, these new unitarity constraints must be cast in a more elaborate manner, as opposed to simple inequalities. In this section, $m = 1$.

4.3.1 4D inelasticity formulation, SDP maximization of the quartic coupling

At a first glance, using `Mathematica`'s tools - `FindMaximum` and `FindMinimum` - seems the most direct method, which would eliminate the need for more intricate ways of imposing inelasticity as in the SDP approach. However, this comes with a great downfall: the fact that computation take enormous amounts of time to run, which is impractical in

the context of this dissertation. Furthermore, we are subject to a "black box", whose optimization procedures we cannot fully understand nor control. For these reasons, it is well worth our time to develop the SDPB program for our purposes.

That being said, there is still the question of how to impose inelasticity. In the optics of this dissertation, two distinct paths will be taken, either using the *optical theorem* or by imposing inelasticity directly on the partial waves - in a similar spirit to Appendix B.1.

Starting by the usual axioms, we focus on the maximization/minimization of the quartic coupling for the scattering of massive, spinless and identical particles in 4D. All of what was introduced in section 3.1 still applies in this case, in particular crossing symmetry, real and extended analyticity and (part of) the unitarity conditions, as well as the Ansatz adopted. As such, the usual expansion is considered, with the new condition that there are no bound-states,

$$T(s,t,u) = \alpha\left(\frac{1}{\rho_s - 1} + \frac{1}{\rho_t - 1} + \frac{1}{\rho_u - 1}\right) + \sum_{a,b,c=0} \alpha_{abc}\, \rho_s^a \rho_t^b \rho_u^c \tag{4.24}$$

and

$$s \mapsto \rho_s = \frac{\sqrt{4 - s_0} - \sqrt{4 - s}}{\sqrt{4 - s_0} + \sqrt{4 - s}}, \qquad s = \frac{s_0(1-\rho_s)^2 + 16\rho_s}{(1+\rho_s)^2} \tag{4.25}$$

The $s + t + u = 4$ condition eliminates part of the redundancy just as it did previously. Thus, the only palpable difference is in the extra or new unitarity conditions which we proceed to analyse.

We focus solely on describing and presenting the results, and only after will the estimates for the values of the optimization process will be presented, in a dedicated subsection - subsection 4.3.1.6.

4.3.1.1 Positivity

Although not quite an inelasticity one, the first natural condition that occurred to us was the weaker condition of *positivity*, which stems from the optical theorem. According to [2, 49], said theorem can be cast in the form

$$\operatorname{Im} T(s,0) = \sqrt{s(s-4)}\,\sigma_{total} \tag{4.26}$$

where σ_{total} is the total cross-section. Positivity is just the observation that Equation 4.26 satisfies $\text{Im}\, T(s,0) > 0$, which is can be written as the positive semidefinite condition

$$\begin{pmatrix} \text{Im}\, T(s,0) & 0 \\ 0 & 1 \end{pmatrix} \succeq 0 \tag{4.27}$$

So, the constraints consist in the usual unitarity conditions $|S_\ell(s)| \leq 1$ - as per demonstrated in Appendix B.1 - for even ℓ up to ℓ_{max} and a uniform ρ grid, plus the positivity condition 4.27.

Using the SDPB program, Figure 4.15 was determined, for the maximization of the quartic coupling $T\left(\frac{4}{3}, \frac{4}{3}, \frac{4}{3}\right)$. Firstly, the plateau of convergence originally observed in section 3.4 is still present; moreover, at first sight, it appears to stabilize at the same value. Most importantly, though, is the fact that, by introducing the positivity condition, the plateau is maintained for higher values of N_{max}! In addition, this feature is present regardless the value of ℓ_{max}.

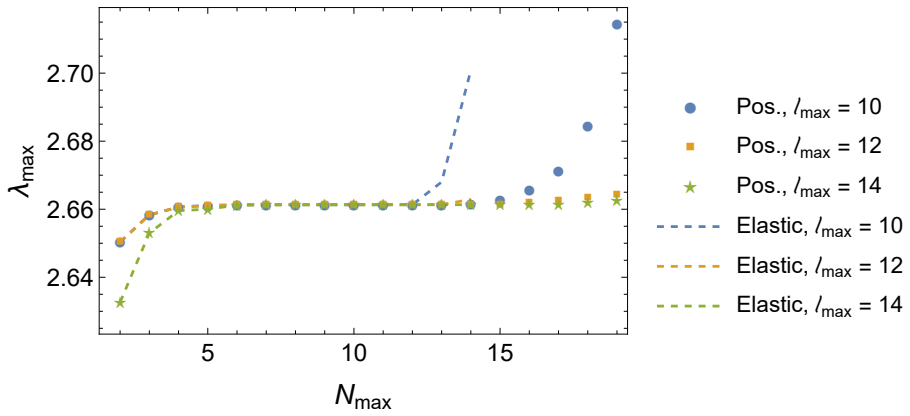

FIGURE 4.15: Maximization of the quartic coupling subject to unitarity conditions 3.13 and 4.27, for several ℓ_{max}. The discrete data (Pos.) correspond to the numerical data, while the dashed curves (Elastic) represent the solution to the same problem without positivity 4.27.

In regards to the minimization procedure, no changes were observed at all. Thus, we will refrain from analysing this objective from now on.

Even though no changes in the value of the plateau have been observed, it is still insightful to discover that positivity works towards stabilizing the algorithm. In practice, stronger conditions than the previous one shall be imposed in upcoming subsections, so there will be no need to make use of these results. So as to observe some measurable difference in the value of the plateau, we proceed with a subtle modification of the unitarity conditions.

4.3.1.2 Lower bound on cross-section

In practice, Equation 4.26 cannot be cast as an SDPB condition, since it is not an inequality. However, let us go back to section 3.1. According to Equation 1.26, the amplitude function admits the partial-wave expansion (for d = 3)

$$T(s,t) = \sum_{\ell=0}^{\infty} 16\pi(2\ell+1)P_\ell(\cos(\theta)) \tag{4.28}$$

where the appropriate normalization has been taken and $P_\ell(x)$ are the Legendre polynomials. Thus, it trivially follows that

$$\text{Im}\, T(s,0) = \sum_{\ell=0}^{\infty} 16\pi(2\ell+1)\text{Im}\, f_\ell(s) \tag{4.29}$$

The "trick" which shall be employed, and which gives name to this section, is to bound Im $f_\ell(s)$ and substitute in Equation 4.29, identifying the right hand side term as an effective "$\sqrt{s(s-4)}\sigma_{total}$". Before doing so, it will be helpful to recall what was done in Appendix B.1. Therein, it was shown that

$$\frac{|a(s)|^2}{2} \leq \text{Im}\, a(s) \leq 2 \tag{4.30}$$

where $a \equiv \sqrt{\frac{s-4}{s}} f_\ell(s)$. The first step is to generalize this result when $|S_\ell(s)|^2 \leq \beta(s)$ instead of $|S_\ell(s)|^2 \leq 1$, which is done in Appendix B.2. The main result is that Equation 4.30 neatly generalizes to

$$\frac{1-\beta(s)}{2} + \frac{|a(s)|^2}{2} \leq \text{Im}\, a(s) \leq 1 + \sqrt{\beta(s)} \tag{4.31}$$

Equation 4.31 puts a lower bound on Im $a(s)$, which we can use to our advantage so as to modify 4.29. Hence,

$$\begin{aligned}
\text{Im}\, T(s,0) &= \sum_{\ell=0}^{\infty} 16\pi(2\ell+1)\text{Im}\, f_\ell(s) \\
&\geq \sum_{\ell=0}^{\infty} 16\pi(2\ell+1)\left[\sqrt{\frac{s}{s-4}}\frac{1-\beta(s)}{2} + \frac{s-4}{s}\frac{|f_\ell(s)|^2}{2}\right] \\
&\geq \sum_{\ell=0}^{\infty} 16\pi(2\ell+1)\left[\sqrt{\frac{s}{s-4}}\frac{1-\beta(s)}{2}\right] \\
&\approx \text{"}\sqrt{s(s-4)}\sigma_{total}\text{"}
\end{aligned} \tag{4.32}$$

Finally, only establishing the appropriate PSD constraint from the previous expression is left. That is easily achieved by the condition

$$\begin{pmatrix} \mathrm{Im}\, T(s,0) - \text{"}\sqrt{s(s-4)}\sigma_{total}\text{"} & 0 \\ 0 & 1 \end{pmatrix} \succeq 0 \tag{4.33}$$

which we used together with the the unitarity conditions for each $S_\ell(s)$.

In this dissertation, two profiles have been considered:

$$\beta_1(s) = \begin{cases} \alpha, & \ell = 0 \wedge s \geq 16 \\ 1, & \ell > 0 \wedge s \geq 16 \end{cases} \tag{4.34}$$

and

$$\beta_2(s) = \begin{cases} \alpha, & (\ell = 0 \vee \ell = 2) \wedge s \geq 16 \\ 1, & \ell > 2 \wedge s \geq 16 \end{cases} \tag{4.35}$$

which greatly simplify the sum in 4.32. In practice, these profiles try to restrict unitarity for either the s partial-wave - profile $\beta_1(s)$ - or both s and p partial-wave - profile $\beta_2(s)$. With these profiles in mind, the maximization of the quartic coupling was carried out. The results are in Figures 4.16 and 4.17, for different choices of α and for both profiles.

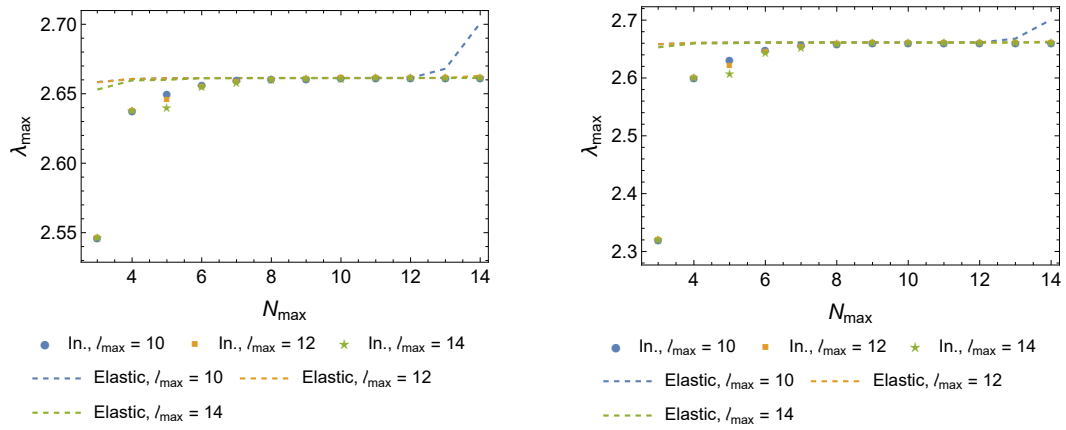

(A) (B)

FIGURE 4.16: Result of maximizing the quartic coupling subject to the new constraint 4.33, for profile $\beta_1(s)$ and (A) $\alpha = 0.8$ and (B) $\alpha = 0.5$. The dashed lines correspond to the solution with unitarity only.

While the data does not see many a difference in Figure 4.16, there is a rather measurable difference for Figure 4.17. In both cases, the algorithm forms a plateau on a certain

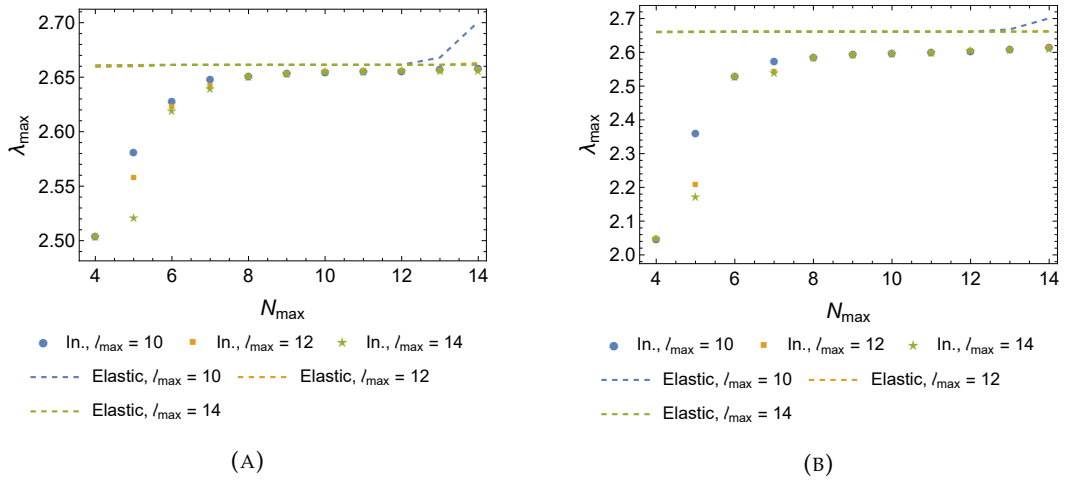

(A) (B)

FIGURE 4.17: Result of maximizing the quartic coupling subject to the new constraint 4.33, for profile $\beta_2(s)$ and (A) $\alpha = 0.8$ and (B) $\alpha = 0.5$. The dashed lines correspond to the solution with unitarity only.

region around $N_{max} = 9$. The contrasting behaviour between both cases is quite understandable: while in the first case the right hand side is of the form

$$16\pi \times 1 \times \sqrt{\frac{s}{s-4}}\frac{1-\beta_1(s)}{2} \tag{4.36}$$

the second case yields

$$16\pi \times 6 \times \sqrt{\frac{s}{s-4}}\frac{1-\beta_2(s)}{2} \tag{4.37}$$

In other words, $\frac{1-\beta(s)}{2} \sim \gamma(s)$, where $0 \leq \gamma(s) \leq 0.5$ which sets a low lower bound for $\mathrm{Im}\, T(s,0)$. However, the latter case is distinct: $6 \times \frac{1-\beta(s)}{2} \sim 6 \times \gamma(s)$, and the new effective *running parameter* $6\,\gamma(s)$ sets higher lower bounds for the imaginary part. For instance, $\beta(s) = \beta_2(s)$ and $\alpha = 0.5$ implies that $6\,\gamma(s) = 1.5$, which can never be imposed by any value of α for $\beta_1(s)$. The results are practically similar to those of the elastic case: this is mainly due to the fact that the quadratic term, which is greater than the remaining one, is being discarded, and as such weaker bounds than those of the elastic case are being imposed.

That being said, there is not much left to analyse. Thus, we proceed with expanding this section to imposing real bounds directly on the total cross-section, obtained analytically by Roy and Martin.

4.3.1.3 Introducing a lower bound on the total cross-section

Instead of going through the process of finding a lower bound for the imaginary part of the amplitude function (in the forward limit) using Equation 4.32, it should be possible

to simply impose a lower bound on σ_{total} in Equation 4.26. In this spirit, we searched known results in the literature and found an interesting result in [50] which states that, for pion-pion scattering, the inelastic part of the cross-section asymptotically satisfies

$$\sigma_{inel}(s) > \frac{\text{const}}{s^{5/2}} \text{Exp}\left[-\frac{\sqrt{s}}{4}(N+5/2)\ln s\right] \equiv \sigma_{RM} \tag{4.38}$$

where $N = 2$ and c is a parameter we will vary between 0 and 1.

Since $\sigma_{total}(s) = \sigma_{elastic}(s) + \sigma_{inelastic}(s) \geq \sigma_{inelastic}(s) > \sigma_{RM}$, Equation 4.26 yields

$$\text{Im}\, T(s,0) = \sqrt{s(s-4)}\,\sigma_{total} > \sqrt{s(s-4)}\,\sigma_{RM} \tag{4.39}$$

The constraint 4.39 has a trivial PSD matrix representation, which is similar to 4.33

$$\begin{pmatrix} \text{Im}\, T(s,0) - \sqrt{s(s-4)}\,\sigma_{RM} & 0 \\ 0 & 1 \end{pmatrix} \succeq 0 \tag{4.40}$$

In practice, we shall impose said profile for $s > 16m^2$, even though it is only valid for large s. As will be seen, however, it has little to no effect on the final result.

Once more, we proceed with the same SDPB program optimization, which results in almost no effect on the original plateau, as reported by Figure 4.18 In fact, the new

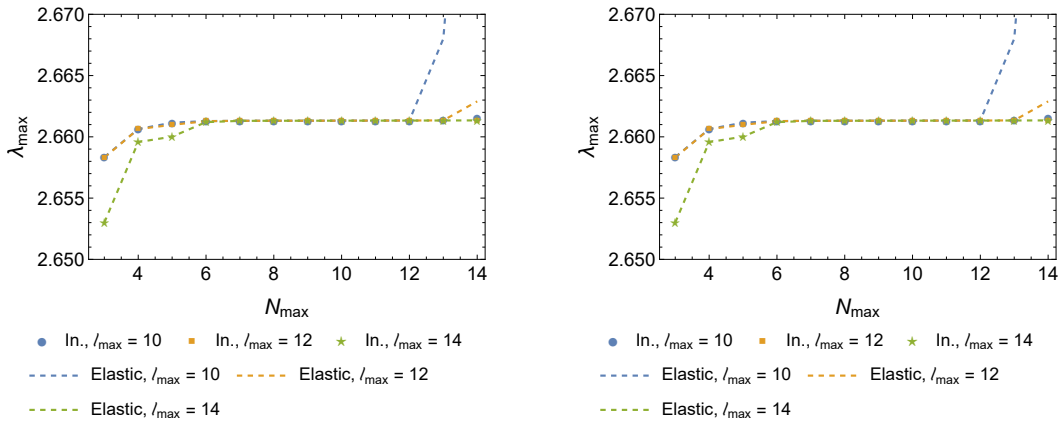

(A) (B)

FIGURE 4.18: Result of maximizing the quartic coupling subject to the new constraint 4.40, for profile 4.38 and (A) $c = 0.5$ and (B) $c = 1$. The dashed lines correspond to the solution with unitarity only.

condition is so weak that changing the value of c from 0.5 to 1 has practically no effect whatsoever, apart from extending the length of the plateau - like introducing positivity did. For this reason, combined with the fact that in the upcoming sections it is showed that the value of the plateau is the same as the original one, we have decided to pursue no

further studies using this method. In hindsight, this was anticipated, since the RM profile is exponentially suppressed and is only asymptotic.

Nonetheless, it is not the last approach of imposing particle production we wish to explore. There is one other that, perhaps, has the most impact of all of the strategies analysed yet: imposing inelasticity directly on the partial-wave amplitudes.

4.3.1.4 Imposing bounds on f_ℓ

Rather than restricting the imaginary part of the amplitude function, one could directly impose constraints on the partial-wave amplitudes. Although both methods seem analogous, there is, intuitively, a fundamental difference that is to be expected. To better understand it, recall that

$$\text{Im}\, T(s,0) = \sum_{\ell=0}^{\infty} 16\pi(2\ell+1)\text{Im}\, f_\ell(s) \tag{4.41}$$

When bounding the imaginary part, effectively a linear combination of the partial-wave amplitudes is being restricted: either one component only, or various spin amplitudes at the same time. Moreover, the quadratic term is not being considered, and thus sub-optimal bounds are being imposed since the elastic component is totally ignored. In turn, the algorithm is optimizing the final solution as it sees fit, not necessarily restricting the lower spin amplitudes, for instance. As concluded in previous sections - section 3.4, specifically - the lower spin amplitudes have a greater impact on the final result. Hence, it would make sense that directly restricting them causes a greater effect on the quartic coupling.

So as to implement this, we make use of the generalized inequalities derived in previous sections, in particular

$$\frac{1-\beta(s)}{2} + \frac{|a(s)|^2}{2} \leq \text{Im}\, a(s) \leq 1 + \sqrt{\beta(s)} \tag{4.42}$$

As shown in Appendix B.2, this can be translated to the PSD condition

$$\begin{pmatrix} 1 - \frac{\text{Im}\, a}{1+\sqrt{\beta(s)}} & \text{Re}\, a \\ \text{Re}\, a & \beta(s) - 1 + \left(1+\sqrt{\beta(s)}\right)\text{Im}\, a \end{pmatrix} \succeq 0 \tag{4.43}$$

which we impose for both $\beta_1(s)$ and $\beta_2(s)$ profiles.

While the optimization for $\beta_1(s)$ yielded satisfying results - cf. Figure 4.19 - the same can not be said about β_2: it is clear from Figure 4.20 that the results are extremely unstable

- this is expected, since the Ansatz does not account for new discontinuities. This issue is similar to that of subsection 4.1.2; when $\alpha = 0.5$, in these conditions, the SDPB program throws errors which state a mathematical impossibility of solving the problem given the constraints. Later, we will show that the expansion of the allowed space of functions - i.e., the addition of new terms to the Ansatz - partially solves this problem. As such, we suspect that this might be the main issue causing the errors.

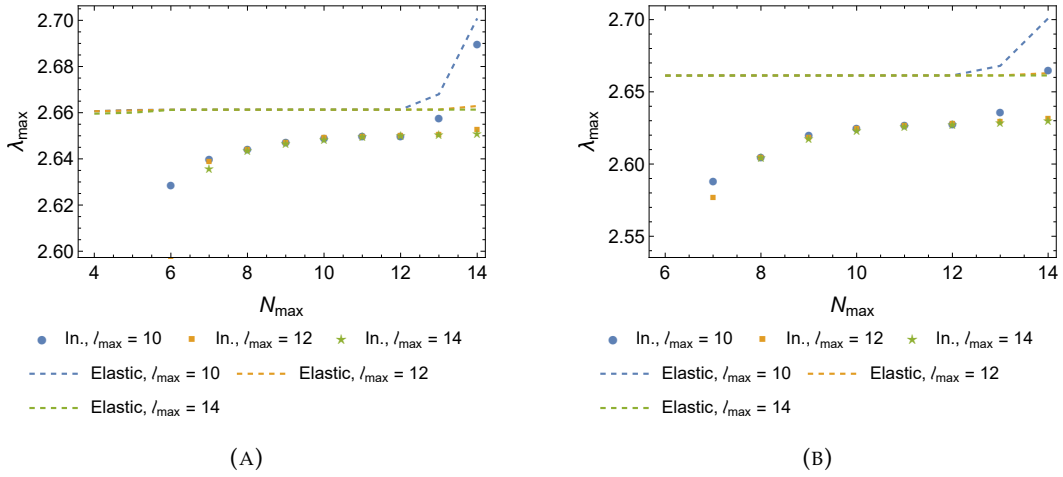

(A) (B)

FIGURE 4.19: Result of maximizing the quartic coupling subject to 4.43, for profile $\beta_1(s)$ and (A) $\alpha = 0.8$ and (B) $\alpha = 0.5$. The dashed lines correspond to the solution with unitarity only.

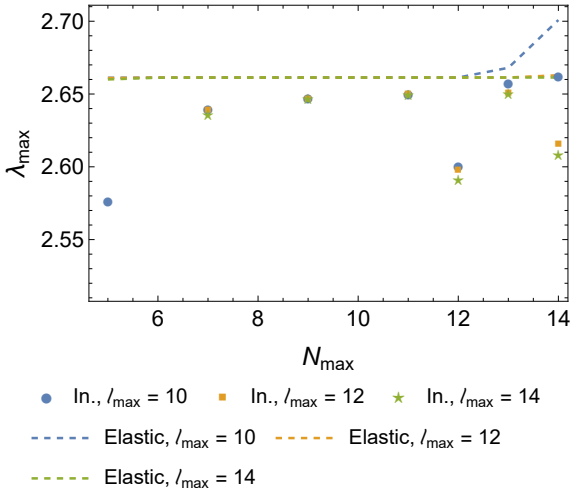

FIGURE 4.20: Result of maximizing the quartic coupling subject to 4.43, for profile $\beta_2(s)$ and $\alpha = 0.8$. The dashed lines correspond to the solution with unitarity only. The holes at odd N_{max} correspond to solutions with SDPB errors.

For $\beta_1(s)$, the solution displays a shorter plateau below the previous, elastic value. Furthermore, by eye, it seems that said plateau is even lower when comparing with subsection 4.3.1.2: our expectations were met!

4.3.1.5 Introducing ρ_{16} terms

The discontinuities introduced for $s > 16m^2$ are not naturally reproduced by the Ansatz 4.24. So as to take into account the inelastic profiles, in subsection 4.1.4 we proposed that the Ansatz was slightly modified: hence the addition of the ρ_{16} terms.

In this subsection, we propose a similar strategy. Thus, Equation 4.24 becomes

$$\begin{aligned} T(s,t,u) = \alpha \left(\frac{1}{\rho_s - 1} + \frac{1}{\rho_t - 1} + \frac{1}{\rho_u - 1} \right) + \sum_{a,b,c=0} \alpha_{abc}\, \rho_s^a \rho_t^b \rho_u^c \\ + \sum_{a,b,c=0} \beta_{abc}\, \rho_{16,s}^a \rho_{16,t}^b \rho_{16,u}^c \end{aligned} \tag{4.44}$$

where

$$\rho_{16,s}(s) \equiv \frac{\sqrt{16 - s_0} - \sqrt{16 - s}}{\sqrt{16 - s_0} + \sqrt{16 - s}} \tag{4.45}$$

In this case, $s_0 = 4/3$ and the inverse map is not particularly important, since the integrals regarding $S_\ell(s)$ are evaluated at the original ρ grid (the s grid is determined by its original inverse map). Computationally speaking, the Ansatz must be truncated; being as general as possible, two independent cutoffs are considered: N_{max} for the ρ terms and $N_{max,16}$ for the ρ_{16} ones.

That being said, a simple step function will be considered for the inelastic profile ($m = 1$),

$$\beta(s) = \begin{cases} \alpha, & \ell = 0 \wedge s \geq 16 \\ 1, & \ell > 0 \wedge s \geq 16 \end{cases} \tag{4.46}$$

which can be imposed by the PSD condition 4.43.

Apart from the usual requirement that N_{max} be less or as large as ℓ_{max}, we suspect that $N_{max,16} + N_{max}$ should not be too large compared to ℓ_{max}. Thus, we carried out a study in the three-dimensional parameter space of the variables $\{\alpha, \rho, \rho_{16}\}$. In order to simplify said study, the maximization of the quartic coupling is treated.

Firstly, we fixed $N_{max} = 14$ and tried $\alpha = 0.8$ and $\alpha = 0.2$. From previous experiences, the second value should pose more difficulties than the first one, considering that it translates into a stronger discontinuity. The results are presented in Figures 4.21 and 4.22. For $\ell_{max} = 14$, in both cases, there seems to be a clear plateau for values of $N_{max,16}$ around $N_{max,16} = 5$. This is an improvement to the 2D case, since for even a low value of α the algorithm converges.

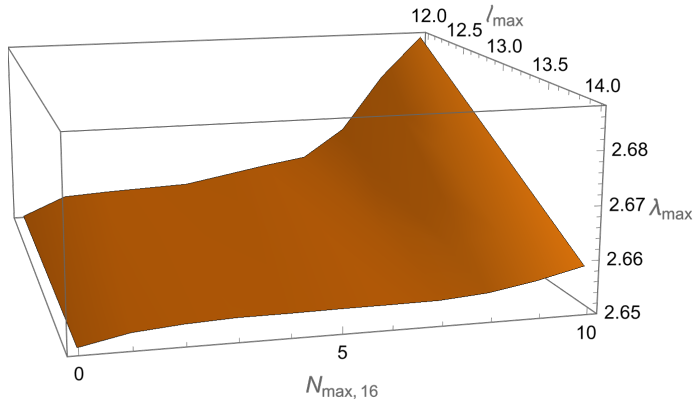

FIGURE 4.21: Result of maximizing the quartic coupling subject to 4.43, for profile $\beta(s)$ and $\alpha = 0.8$. For $\ell_{max} = 14$, there seems to be a plateau for values of $N_{max,16}$ around $N_{max,16} = 5$.

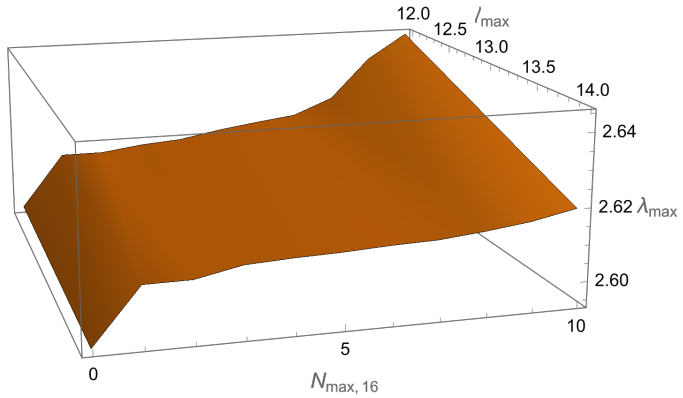

FIGURE 4.22: Result of maximizing the quartic coupling subject to 4.43, for profile $\beta(s)$ and $\alpha = 0.2$. For $\ell_{max} = 14$, there seems to be a plateau for values of $N_{max,16}$ around $N_{max,16} = 5$.

Figures 4.23 and 4.24 can attest to these improvements at the S-matrix components level. The ρ_{16} terms have astonishingly positive effects in this aspect: for $N_{max,16}$ in the vicinity of the plateau, for both cases, the S-matrix components better describe the discontinuity than for the case $N_{max,16} = 0$.

The best values of N_{max} and ℓ_{max} are 14 and 14, giving the region where the plateau seems more stable. For these values, Figures 4.25 and 4.26 show the plateaus. Even though they seem unstable, it must be noted that the difference between neighbouring points is in the third decimal place, which is quite more that what we wish to achieve.

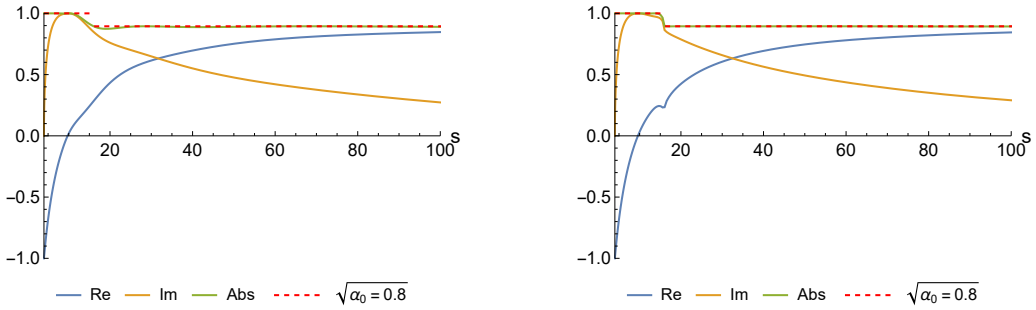

(A) (B)

FIGURE 4.23: Result of maximizing the quartic coupling subject to 4.43, for profile $\beta(s)$ and (A) $\alpha = 0.8$ with $N_{max,16} = 0$ and (B) $\alpha = 0.8$ with $N_{max,16} = 5$.

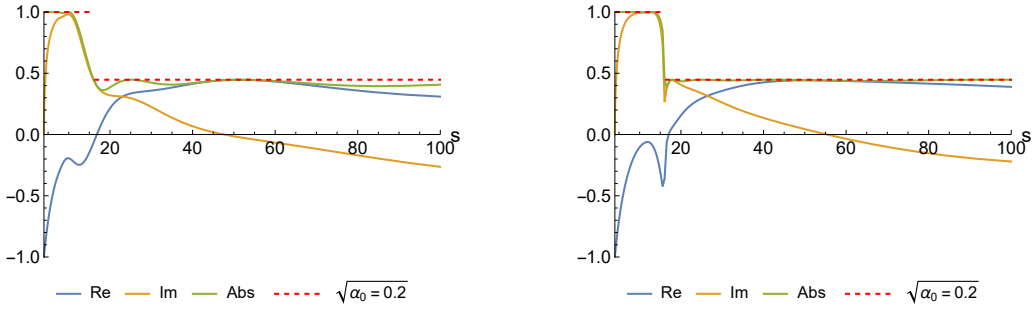

(A) (B)

FIGURE 4.24: Result of maximizing the quartic coupling subject to 4.43, for profile $\beta(s)$, $N_{max} = 14$, $\ell_{max} = 14$ and (A) $\alpha = 0.2$ with $N_{max,16} = 0$ and (B) $\alpha = 0.2$ with $N_{max,16} = 9$.

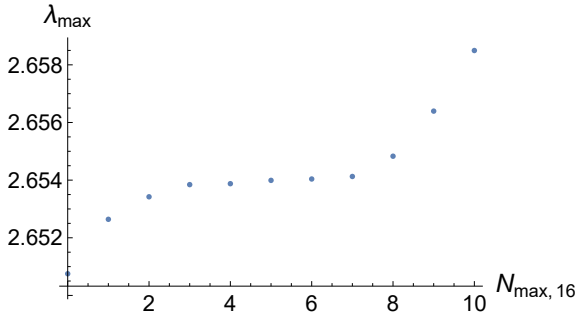

FIGURE 4.25: Result of maximizing the quartic coupling subject to 4.43, for profile $\beta(s)$ and $\alpha = 0.8$, $\ell_{max} = 14$ and $N_{max} = 14$.

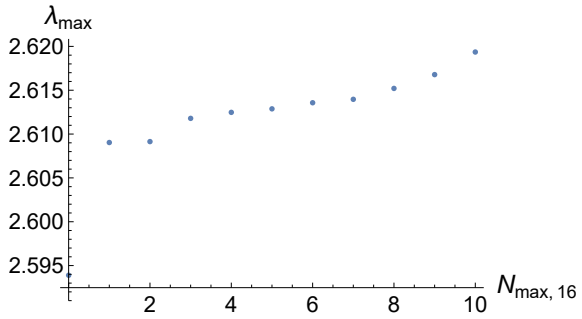

FIGURE 4.26: Result of maximizing the quartic coupling subject to 4.43, for profile $\beta(s)$ and $\alpha = 0.2$ and $\ell_{max} = 14$ and $N_{max} = 14$.

More important is to push α as low as possible. In that spirit, the lowest value we have studied is $\alpha = 0.01$. For said value, Figures 4.27, 4.28 and 4.29 show the quartic coupling optimization as well as the S-matrix components. Due to the complexity of space of parameters, only the $N_{max} = 10$ case was studied. However, it shows promise: we expect that, increasing $\{N_{max}, N_{max,16}, \ell_{max}\}$, more stable results can be achieved.

The restriction of the partial-wave amplitudes and the ρ_{16} term close the subsection on 4D inelasticity methodology and optimization strategies. So as to better understand what resulted from each approach, we condensed all the results in the upcoming short but informative subsection.

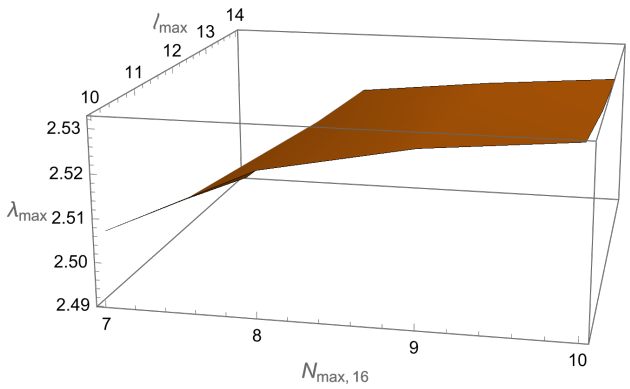

FIGURE 4.27: Result of maximizing the quartic coupling subject to 4.43, for profile $\beta(s)$ and $\alpha = 0.01$.

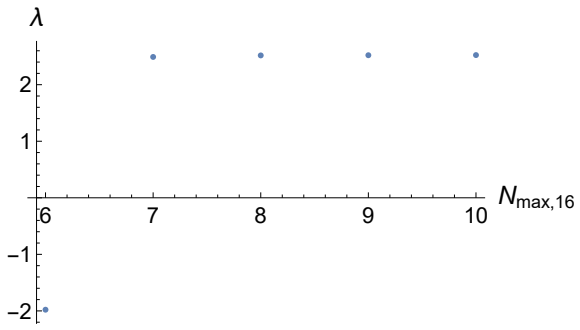

FIGURE 4.28: Result of maximizing the quartic coupling subject to 4.43, for profile $\beta(s)$ and $\alpha = 0.01$, fixed $N_{max} = 10$ and $\ell_{max} = 14$.

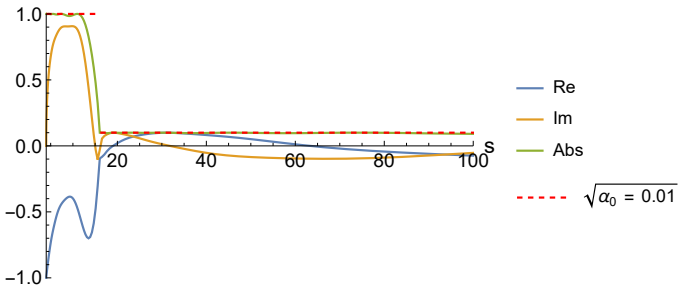

FIGURE 4.29: Result of maximizing the quartic coupling subject to 4.43, for profile $\beta(s)$ and $\alpha = 0.01$ with $N_{max,16} = 10$, $N_{max} = 10$ and $\ell_{max} = 14$.

4.3.1.6 Comparison between the different approaches

As the title suggests, this section is aimed at reviewing and summarizing the main results of each approach to inelasticity. By results we mean the value that the quartic coupling takes at the plateau, which is determined by considering the mean value of λ in such region. Seeing that the length of the plateau varies from method to method, a specialized interval of N_{max} must be chosen accordingly. Each choice is taken based on the values showed previously, and no others. As for the uncertainty in each value, the standard deviation of the used points was selected.

Table 4.2 is rich and full of numeric information that previously was only available by eye. Before commenting on the results, we leave a list of N_{max} used in each case:

- **Original:** $N_{max} \in \{7, ..., 11\}$;
- **Positivity:** $N_{max} \in \{7, ..., 12\}$;
- **"σ_{total}", $\beta_1(s)$ and $\alpha = 0.8$:** $N_{max} \in \{9, ..., 12\}$;
- **"σ_{total}", $\beta_1(s)$ and $\alpha = 0.5$:** $N_{max} \in \{9, ..., 12\}$;

	$\ell_{max} = 10$	$\ell_{max} = 12$	$\ell_{max} = 14$
Original	2.661317 ± 0.000006	2.661316 ± 0.000006	2.661314 ± 0.000008
Positivity	2.661320 ± 0.000009	2.661319 ± 0.000007	2.661316 ± 0.000009
"σ_{total}", $\beta_1(s)$ and $\alpha = 0.8$	2.6612 ± 0.0001	2.6611 ± 0.0002	2.6611 ± 0.0002
"σ_{total}", $\beta_1(s)$ and $\alpha = 0.5$	2.6608 ± 0.0003	2.6607 ± 0.0003	2.6606 ± 0.0004
"σ_{total}", $\beta_2(s)$ and $\alpha = 0.8$	2.655 ± 0.001	2.655 ± 0.001	2.655 ± 0.001
"σ_{total}", $\beta_2(s)$ and $\alpha = 0.5$	2.599 ± 0.005	2.598 ± 0.005	2.598 ± 0.005
RM, $c = 0.5$	2.661317 ± 0.00006	2.661316 ± 0.00006	2.661314 ± 0.00008
RM, $c = 1.0$	2.661317 ± 0.00006	2.661316 ± 0.00006	2.661314 ± 0.00008
f_ℓ, $\beta_1(s)$ and $\alpha = 0.8$	2.6497 ± 0.0004	2.6496 ± 0.0005	2.6492 ± 0.0009
f_ℓ, $\beta_1(s)$ and $\alpha = 0.5$	2.627 ± 0.001	2.626 ± 0.002	2.625 ± 0.002
f_ℓ, ρ_{16} and $\alpha = 0.8$	– – – – – – – – – –	– – – – – – – – – –	$2.65397573 \pm 0.00000001$
f_ℓ, ρ_{16} and $\alpha = 0.2$	– – – – – – – – – –	– – – – – – – – – –	2.6129348 ± 0.0000007
f_ℓ, ρ_{16} and $\alpha = 0.01$	– – – – – – – – – –	– – – – – – – – – –	2.5133 ± 0.0002

TABLE 4.2: Value of λ at the plateau for several approaches.

- **"σ_{total}", $\beta_2(s)$ and $\alpha = 0.8$:** $N_{max} \in \{9, ..., 12\}$;
- **"σ_{total}", $\beta_2(s)$ and $\alpha = 0.8$:** $N_{max} \in \{9, ..., 12\}$;
- **RM, $c = 0.5$:** $N_{max} \in \{7, ..., 11\}$;
- **RM, $c = 1$:** $N_{max} \in \{7, ..., 11\}$;
- **f_ℓ, $\beta_1(s)$ and $\alpha = 0.8$:** $N_{max} \in \{10, ..., 12\}$;
- **f_ℓ, $\beta_1(s)$ and $\alpha = 0.5$:** $N_{max} \in \{10, ..., 12\}$;
- **f_ℓ, ρ_{16} and $\alpha = 0.8$:** $N_{max,16} \in \{3, ..., 7\}$ ($N_{max} = 14$, $\ell_{max} = 14$);

- f_ℓ, ρ_{16} **and** $\alpha = 0.2$**:** $N_{max,16} \in \{3, ..., 7\}$ ($N_{max} = 14$, $\ell_{max} = 14$);
- f_ℓ, ρ_{16} **and** $\alpha = 0.01$**:** $N_{max,16} \in \{7, ..., 10\}$ ($N_{max} = 10$, $\ell_{max} = 14$);

First and foremost, imposing the Roy and Martin lower bound for the inelastic part of the total cross-section was utterly ineffective: the values are equal to the original ones.

On the other hand, every other method resulted in a small (yet noticeable) decrease in the value of the quartic coupling: just as expected! For the first four profiles, decreasing the value of α has a tendency for decreasing the value of λ. Moreover, using $\beta_2(s)$ instead o $\beta_1(s)$ results in a more acute reduction from the original value (the difference between the data for these profiles is $\approx 0.2\% - 2.3\%$).

Finally, when comparing the same profile, it is evident that imposing constraints directly on the partial-waves has a greater effect than introducing a pseudo total cross-section, just as anticipated.

For now, the main focus of our analysis was the quartic coupling, being the target variable. However, looking back, there is still yet another object which can be studied: $\text{Im}\, T(s, 0)$. Since most of the constraints were imposed directly on this quantity, it would be interesting to see how it compares to the numerical results.

4.3.2 Analysis of Im $T(s, 0)$

Even though the main focus of the previous subsection was the quartic coupling, considering the introduction of new constraints related either to the optical theorem or the partial-wave amplitudes, there are still insightful results that may have been overlooked. Be it directly or indirectly, the previously mentioned constraints relate to the optical theorem equation

$$\text{Im}\, T(s, 0) = \sqrt{s(s-4)}\, \sigma_{total} \tag{4.47}$$

or

$$\text{Im}\, T(s, 0) = \sum_{\ell=0}^{\infty} 16\pi(2\ell + 1)\text{Im}\, f_\ell(s) \tag{4.48}$$

Upon imposing lower bounds to the right hand side of either equations, one is met with an inequality which states that $\text{Im}\, T(s, 0) - \text{RHS} \geq 0$. In particular, we are interested in the question "does this inequality ever saturate the lower bound?", which we try to analyse in this subsection.

At the start of this study is an important issue which has not been addressed yet: whenever each constraint is imposed, is the inelastic, elastic or total cross-section being

given? Fortunately for us, in [2] an explicit expression for the $2 \to 2$ contribution is obtained, which reads

$$\begin{aligned} T_s(s) &\geq \frac{(s-4)^{\frac{d-3}{2}}}{8(4\pi)^{d-2}\sqrt{s}} \int_{-1}^{1} dz' \int_{-1}^{1} dz'' \, \mathcal{P}_d(1,z',z'') T^{(+)}(s,t(z')) T^{(-)}(s,t(z'')) \\ &\overset{d\to 3}{=} \sqrt{\frac{s-4}{s}} \frac{1}{8\times 16\pi^2} \int_{-1}^{1} dz' \int_{-1}^{1} dz'' \, 2\pi\delta(z'-z'') T^{(+)}(s,t(z')) T^{(-)}(s,t(z'')) \\ &= \frac{1}{64\pi}\sqrt{\frac{s-4}{s}} \int_{-1}^{1} dz \left| T^{(+)}(s,t(z)) \right|^2 \end{aligned} \tag{4.49}$$

where (B.7) in [2] was used and

$$T^{(\pm)} \equiv \lim_{\epsilon\to 0} T(s \pm i\epsilon, t), \qquad T_s(s,t) = \text{Disc}_s \, T(s,t) \equiv \text{Im}\, T(s,0) \tag{4.50}$$

Thus, plotting the expression above - which we dub elastic expression - against the solution for $\text{Im}\, T(s,0)$ and the lower bound which was used, it should be possible to compare and make the appropriate comments. Furthermore, in some cases, positivity as well as the sum the elastic expression and the RHS of the optical theorem will be plotted. The reason for doing this will become clear later.

As examples, only two profiles were selected: "σ_{total}", $\beta_1(s)$ and $\alpha = 0.8$ and f_ℓ, $\beta_1(s)$ and $\alpha = 0.8$. All the other plots can be obtained in a similar fashion.

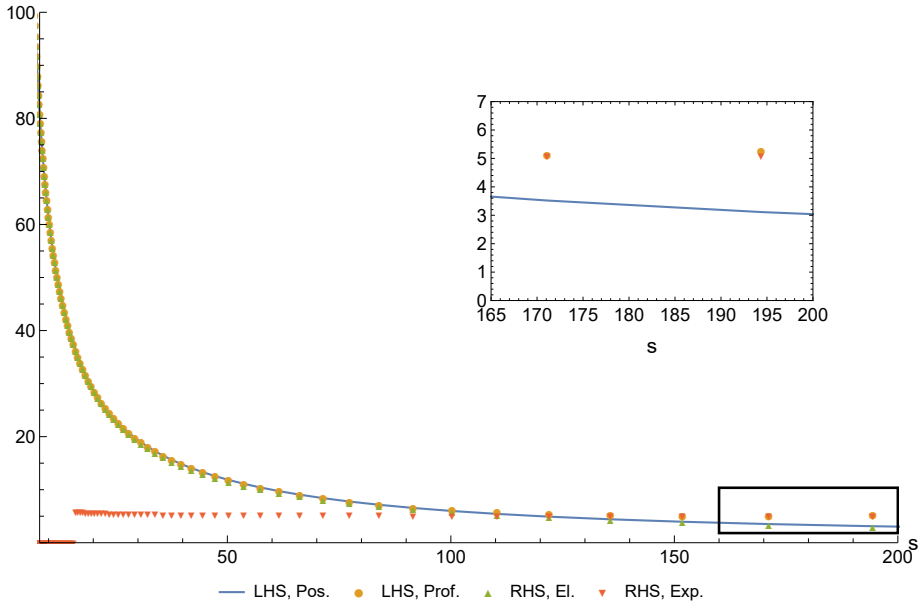

FIGURE 4.30: Comparison between the solution with positivity, *LHS, Positivity* (*LHS, Pos.*), the LHS of the optical theorem for the RHS "σ_{total}", $\beta_1(s)$ and $\alpha = 0.8$, *LHS, Profile* (*LHS, Prof.*), the *RHS, Elastic* (*RHS, El.*) and RHS "σ_{total}", $\beta_1(s)$ and $\alpha = 0.8$, *RHS, Expression* (*RHS, Exp.*).

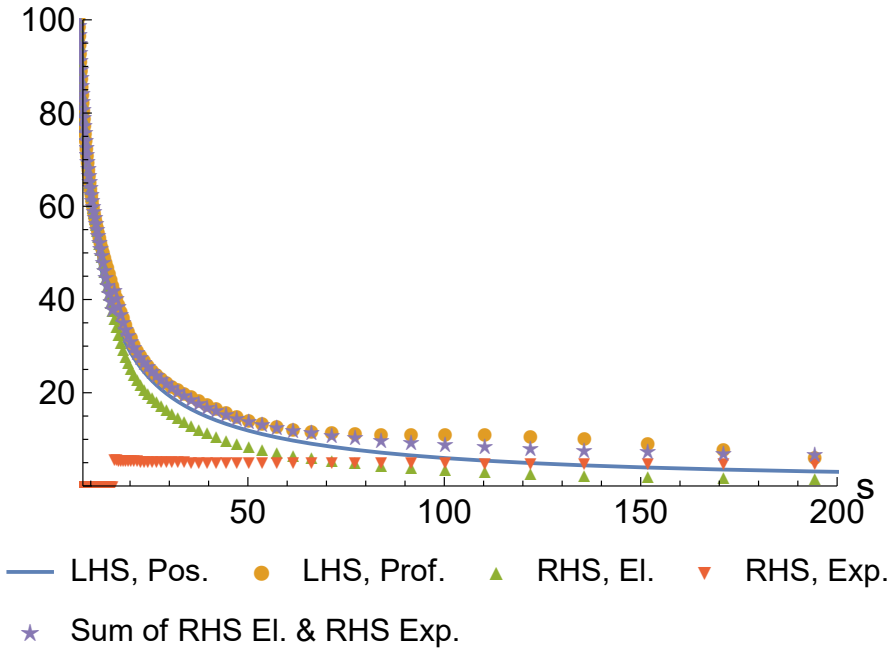

FIGURE 4.31: Comparison between the solution with positivity, *LHS, Positivity* (*LHS, Pos.*), the LHS of the optical theorem for f_ℓ, $\beta_1(s)$ and $\alpha = 0.8$, *LHS, Profile* (*LHS, Prof.*), the *RHS, Elastic* (*RHS, El.*), the RHS f_ℓ, $\beta_1(s)$ and $\alpha = 0.8$, *RHS, Expression* (*RHS, Exp.*), and the sum.

There are quite some details worth exploring in both Figures 4.30 and 4.31 ($N_{max} = 14$ and $\ell_{max} = 14$). First, let us make clear what the *RHS, Exp.* is for both cases. For Figure 4.30, expression 4.36 was used, whereas in the second case the same expression was used as well! This results from expanding the amplitude function in terms of partial-wave amplitudes and ignoring the quadratic term in the lower inequality of 4.31.

That being said, we start by analysing Figure 4.30. For all energies, it can be checked that *RHS, El.* closely follows the *LHS, Prof.* solution: thus, it can be said that the positivity solution naturally saturates the elastic bound, even though it was not imposed. As such, we anticipate that any given "inelasticity" - which we do not know if it contains some elasticity - will only have a measurable effect if it is stronger than the elastic condition. For low to medium energies, $0 < s < 100$ ($m^2 = 1$), *LHS, Prof.* agrees with *LHS, Pos.*, which means that our solution saturates elasticity even though expression 4.36, weaker than elasticity (*RHS, El.*), is imposed. When *RHS, Exp.* intercepts *LHS, Pos.*, this is not the case: *RHS, Exp.* becomes comparable and greater than *RHS, El.*, at which point *LHS, Prof.* starts following the former rather than the latter. Furthermore, as anticipated, *RHS, Exp.* has any influence on $\mathrm{Im}\, T(s,0)$ when it surpasses the elasticity condition.

On the other hand, there is Figure 4.31, which requires a different analysis from the previous one. Interestingly enough, *LHS, Pos.* no longer seems to agree with *RHS, El.*, which means that there is something fundamentally different between this case of study and the previous one. Moreover, *LHS, Prof.* does not agree with either *LHS, Pos.* or *RHS, Exp.*, but rather with the sum *RHS, El.* and *RHS, Exp.*. Even though *RHS, Exp.* was used as reference, Im f_ℓ has, in fact, another lower bound set by 4.31; this lower bound corresponds to part of *RHS, Exp.* plus a quadratic term we have discarded. However, the quadratic term is simply the elastic contribution! Hence, when taking both into account - their sum - we obtain a profile which follows *LHS, Prof.* almost perfectly*.

To sum up: while in Figure 4.30 Im $T(s,0)$ is dominated by the elastic regime until intermediate energies and inelastic regime at high energies, in Figure 4.31 the same quantity is always dominated by the sum of the inelastic and elastic terms.

It is with these remarks that we complete our study of the introduction of inelasticity in the context of the maximization of the quartic coupling. Regarding inelasticity, per se, there have not been any further studies by our part. However, there is yet a final topic we would like to discuss, which originated from the analysis of Im $T(s,0)$. The main question we can ask about this object is "For each s, what is the maximum that Im $T(s,0)$ can attain?". As we will see in the next section, there are reasons for said quantity not to be bounded.

4.3.3 Maximization of Im $T(s,0)$

The final subsection of this chapter concerns the maximization of the imaginary part of the amplitude, in the forward limit. As discussed previously, this idea stemmed from the observation that, instead of studying said object as a consequence of maximizing the quartic coupling, one could directly maximize Im $T(s,0)$. Unbeknown to us, a somewhat similar approach had already been taken [51]. Nonetheless, this was only found out later, and thus our conclusions and results will be presented.†

*In some regions, the points do not quite agree exactly. However, upon plotting these graphs, we came to the conclusion that then N_{max} was increased, *LHS, Prof.* decreased for high energies. Thus, we suspect that numerical imprecisions may be at play. For $\ell_{max} = 14 = N_{max}$, also, λ is barely on the plateau.

†A special mention to Andrea Guerrieri, João Penedones and Pedro Vieira must be made, for only after discussing with them were our arguments better organized.

The idea is elementary: to given the Ansatz for $T(s,t)$ and maximize $\operatorname{Im} T(s,0)$. In the same spirit as Equation 4.24, we started by considering

$$T(s,t,u) = \alpha\left(\frac{1}{\rho_s - 1} + \frac{1}{\rho_t - 1} + \frac{1}{\rho_u - 1}\right) + \sum_{a,b,c=0} \alpha_{abc}\, \rho_s^a \rho_t^b \rho_u^c \tag{4.51}$$

However, this does not yield that great a result. Thus, we think of terms that can be added: whichever they may be, they must not break crossing-symmetry nor unitarity, and analytically with the structure of the S-matrix. To that end, we added two terms:

$$\begin{aligned} T(s,t,u) = {} & \alpha_1 \sqrt{s^2+t^2+u^2} + \alpha_2 \left(\sqrt{s^2+t^2+u^2}\right)^2 + \alpha\left(\frac{1}{\rho_s - 1} + \frac{1}{\rho_t - 1} + \frac{1}{\rho_u - 1}\right) \\ & + \sum_{a,b,c=0} \alpha_{abc}\, \rho_s^a \rho_t^b \rho_u^c \end{aligned} \tag{4.52}$$

The result of maximizing the target objective resulted in Figure 4.32. The additional plotted line corresponds to the Froissart bound, which states that, at high energies,

$$\sigma_{total}(s) \underset{s\to\infty}{\geq} \text{const.} \log^2 s \tag{4.53}$$

where σ_{total} is the total cross-section. Firstly, we see that, at high energies, this bound seems to be bellow the numerical data: it is only complied with asymptotically. The overall algorithm does not seem to converge, at least for medium/high energies. We suspect that relevant terms must be missing, which could trigger the same fast convergence as the threshold pole did.

So as to partially circumvent this issue, we propose another method: instead of maximizing the total amplitude, we make use of the expansion in Equation 4.48. Since each $f_\ell(s)$ must be bounded, it must be easier to expand $T(s,0)$ and successively adding higher spin terms. Unfortunately, as it can be easily checked, the results were similar to those of Figure 4.32.

Since two different approaches failed in determining satisfying results, the problem must lie in the setup itself. For one, the Ansatz 4.52 contains terms which violate unitarity. More specifically, the square root functions violate unitarity asymptotically, when $s \to \infty$: it is easily checked by writing out the $S_0(s)$ component. The reason we did not encounter any problem with this earlier was the fact that unitarity was being imposed on a finite-valued grid, which did not consider asymptotic values.

On the other hand, there is a much deeper reason for expecting the maximization of

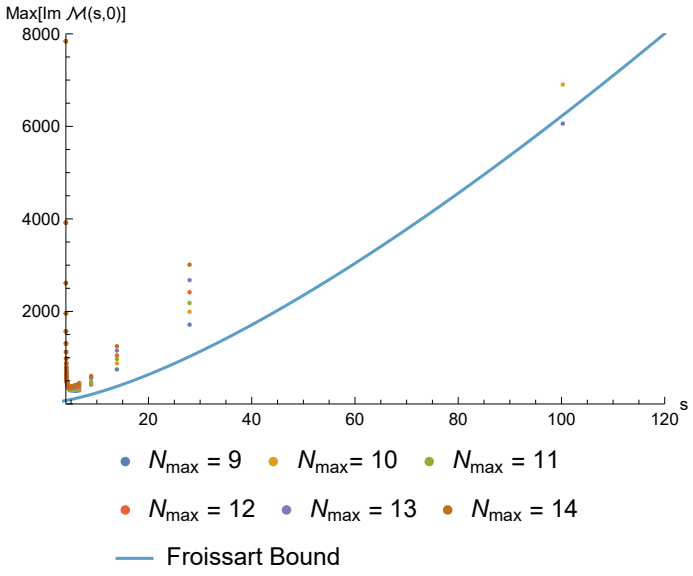

FIGURE 4.32: Comparison between the numerical data for the maximization of Im $T(s,0)$ for $\ell_{max} = 14$ vs. the Froissart bound.

Im $T(s,0)$ to be troublesome. This quantity is intimately related to the total cross-section of the scattering process, which can be clearly unbounded. In order to see this, it suffices to think of the Relativistic Breit–Wigner formula: for a sufficiently short-lived resonance, the cross-section is proportional to the resonance width times a Dirac-delta distribution. Thus, in hindsight, it should never have been a feasible bounded quantity.

Chapter 5

Conclusions and Further Work

In this last chapter we provide a concise summary of the results of the thesis, as well as some comments. Finally, we discuss future directions that may be taken following this work, in addition to several other topics that might have been studied.

We started off by understanding the relevance of the S-matrix Bootstrap, in comparison with other QFT approaches. Having introduced the S-matrix, naturally its properties were discussed, in particular Analyticity, Crossing-symmetry and Unitarity, followed by the Dispersion Relations and the Partial-wave Expansion, which was of the utmost importance for Chapters 3 and 4. These sections provided us with the necessary machinery for tackling all problems that followed.

Having discussed and analysed the entrails of the fundamental properties of the S-matrix, Chapter 2 begun by introducing to the idea of the primal approach to the Bootstrap, which is complementary to the later discussed approach of the dual. Firstly, we understood the reasoning behind this approach, and started by applying it to a simple setup in a 2D Lorentzian space. The QFT entailed the scattering of identical, massive, scalar and neutral particles, which allowed for a bound state of mass $m_b \geq m$. By applying the discretized version of the dispersion relations to a specific analytic structure of the S-matrix, we proceeded with the maximization of the cubic coupling of the lightest particles to the bound state, having found almost perfect agreement with the profile of the sine-Gordon S-matrix. Following this approach was another, which made use of maps from the s-plane to the unit disk: it allowed for a more precise method, where the numerical cutoff was the only numerical approximation. Thus, having discussed both techniques, a generalization was made, so as to include two and three bound-states. Using the developed methods, we were able to find great compatibility between the obtained data and the analytic results.

Due to the fact that the case where the cubic coupling is null is also feasible, we immersed ourselves in the study of EFTs. As shown in Chapter 2, these special theories relate to this case in the sense that both can be represented by Taylor expansions at different points (energies). The most intuitive quantities to study are the $S(2)$ vs. $S^{(2)}(2)$, the first two coefficients in the expansion. The point $s = 2m^2$ was chosen due to being crossing invariant. In the end, we obtained a closed space, which can be neatly compared to data from the paper [28], by simply taking a change of variables. The most interesting part is that some known theories such as the Free boson and Free Majorana fermion were identified to lie on the cusps of the determined curves. We proceeded with extending the space of variables to include $S^{(4)}(2)$, and plotted the obtained results which we dubbed "$S^{(4)}(2)$ pancake".

Finally, we presented the dual philosophy, and applied it to the same optimization challenge previously stated. The results were as precise as before, but the given method actually converged better, numerically speaking, than the primal approach.

Having developed some intuition and familiarity with the Bootstrap techniques, we enter Chapter 3, were the same QFT is considered in higher dimensions. The main challenge of this chapter was the complete shift in the paradigm, in that partial-wave expansions were a must in order to impose unitarity, which otherwise posed terrible problems. In doing so, we adopted another framework: the use of SDPB [4] in order to solve the numerical optimization problems. A similar Ansatz to Chapter 2 was used, and results similar to the followed papers were obtained. In particular, we proceeded with the maximization of the cubic coupling, as well of the quartic coupling, an historically relevant quantity.

Thus enters the holy grail of this thesis: Chapter 4. The introduction of particle production - commonly referred to as inelasticity - begun with the 2D case, with the modification of the unitarity conditions. By introducing a specific set of inelastic profiles, we determined measurable changes to the perfectly elastic case. Two different Ansätze were established, yielding different results. So as improve the primal method, we expanded the original Ansatz to include the ρ_{16} terms, a new set of maps that imposed cuts at $s = 16m^2$, which resulted in some improvements. However, they were completely overshadowed by the dual approach, generalized to include inelasticity.

Naturally, we progressed to higher dimensions, in particular 4D. Some generalizations

to the provided methods were made, so as to still make use of the SDPB program. However, imposing inelasticity in higher dimensions proved a different beast than in lower dimensions, since several approaches came to mind. In this thesis, we have decided to impose bounds on the partial waves, f_ℓ, as well as on the imaginary part of the amplitude in the forward limit, $\text{Im}\, T(s,0)$. Both yielded different results, which is natural: we expect that directly restricting the partial-waves results in stricter results than giving both the Ansatz and SDPB more freedom.

Once more, this called for the introduction of ρ_{16} terms. In this case in particular, the usage of said variables proved invaluable in the enhancement of previous data, since we were able to push inelasticity considerably further. It is our opinion that additional study must be made regarding these new variables: it seems as though we are in the right track to find the maximally optimal values for inelasticity. In theory, we must first understand what other terms, compatible with unitarity, should be introduced.

The last two subsections that make up the main body of the thesis consist in explorations that came up during the analysis of the obtained data. Firstly, we wished to check whether the optical theorem was being satisfied, when the corresponding constraints were imposed. The results depend on whether the constraints are directly applied to the partial-waves or as a total crossing section, having different interpretations in each case. Finally, we proposed the study of the maximization of $\text{Im}\, T(s,0)$, as it seemed, at the time, a good physical observation tied to the total cross-section. However, said study did not yield relevant data: turns out that this quantity may be highly unstable to the introduction of resonances.*

As we see it, this thesis serves a stepping stone to a much wider and interesting field of research that is the inelastic scattering. As a first step, it would maybe prove more fruitful to come up with complementary terms apart from ρ_{16}, as mentioned above. Other than this, it may be interesting to search for new ways of imposing the inelastic conditions, by including higher point scattering functions of the form $n \to m$, $n \in \{2,3,...\}$, $m \in \{2,3,...\}$. For example, let us consider the setup of a QFT with two particles, A and B, $\mathbb{Z}_2$ even and odd, respectively. For a $\mathbb{Z}_2$ preserving interaction, we can actually consider two possible couplings: g_{AAA} and g_{BBA}, which can be maximized studying the scattering processes $AA \to BB$, $AB \to AB$, $BB \to BB$ and $AA \to AA$. In maximizing both couplings, we can actually get a 2D closed space. In particular, we come to the conclusion

*Moreover, it had already been carried out by a different team of investigators, as we later found out.

that, for instance, $AA \to ?$ is not a completely elastic process, as there are production of BB pairs. Thus, we can try to inject the information about this additional particle production of said pairs in the elastic scattering maximization of the single correlator $AA \to AA$, as an inelastic profile, and check whether the same bounds as the mutliparticle system are obtained.*

*We must thank Andrea Guerrieri for this wonderful idea and its subsequent discussion.

Appendix A

Dual from dispersion relations

In section 2.2, the Lagrangian 2.47 is presented, without proof. However, it has a quite clear origin in the dispersion relations. In what follows, we impose subtractions to allow for a general behaviour compatible with the Froissart-Gribov bound.

Setting the external particle mass to $m = 1$, we apply Cauchy's integral formula

$$T(s) - T(2) = \frac{1}{2\pi i}\int_{C_\epsilon(s)} dz\, \frac{T(z)}{z-s} - \frac{1}{2\pi i}\int_{C_\epsilon(s)} dz\, \frac{T(z)}{z-2} \tag{A.1}$$

where $C_\epsilon(s)$ is a circular contour of radius ϵ around s. Considering that $T(s)$ has poles for $s \in [0,4]$ and cuts for $s \geq 4$ and $s \leq 0$, let us show what happens for $T(s)$, starting by the physical region:

$$\begin{aligned} T(s) &= \frac{1}{2\pi i}\int_{C_\epsilon(s)} dz\, \frac{T(z)}{z-s} \\ &= \frac{1}{2\pi i}\left[\int_{-\infty}^{0} dz\, \frac{T(z+i0^+)}{z-s+i0^+} + \int_{0}^{-\infty} dz\, \frac{T(z-i0^+)}{z-s-i0^+}\right. \\ &\left. + \int_{+\infty}^{4} dz\, \frac{T(z-i0^+)}{z-s-i0^+} + \int_{4}^{+\infty} dz\, \frac{T(z+i0^+)}{z-s+i0^+}\right] \end{aligned} \tag{A.2}$$

Using the change of coordinates $z = 4 - z$ for the first two terms and crossing symmetry property,

$$\begin{aligned}
T(s) &= \frac{1}{2\pi i}\left[\int_4^{+\infty} dz\, \frac{T(4-z+i0^+)}{4-z-s+i0^+} + \int_{+\infty}^{4} dz\, \frac{T(4-z-i0^+)}{4-z-s-i0^+}\right. \\
&\left. + \int_{+\infty}^{4} dz\, \frac{T(z-i0^+)}{z-s-i0^+} + \int_{+\infty}^{4} dz\, \frac{T(z+i0^+)}{z-s+i0^+}\right] \\
&= \frac{1}{2\pi i}\left[\int_4^{+\infty} dz\, \frac{T(z-i0^+)}{4-z-s+i0^+} + \int_4^{+\infty} dz\, \frac{T(z+i0^+)}{4-z-s-i0^+}\right. \\
&\left. + \int_{+\infty}^{4} dz\, \frac{T(z-i0^+)}{z-s-i0^+} + \int_4^{+\infty} dz\, \frac{T(z+i0^+)}{z-s+i0^+}\right] \\
&= \frac{1}{2\pi i}\left[-2i\int_4^{+\infty} dz\, \frac{\operatorname{Im} T(z)}{4-z-s} + 2i\int_4^{+\infty} dz\, \frac{\operatorname{Im} T(z)}{z-s}\right] \\
&= \frac{1}{\pi}\int_4^{+\infty} dz \operatorname{Im} T(z)\left[\frac{1}{z-s} + \frac{1}{z-t(s)}\right]
\end{aligned} \tag{A.3}$$

where $\operatorname{Im} T(z) \equiv \frac{1}{2i}\left(T(z+i0^+) - T(z-i0^+)\right) = \frac{1}{2i}\left(T(z+i0^+) - T^*(z+i0^+)\right)$, using real analiticity of $T(z)$ (note that, in this case, $z \in \mathbb{R}$). Doing exactly the same for $T(2)$ and subtracting $T(s) - T(2)$,

$$\begin{aligned}
T(s) - T(2) &= \frac{1}{\pi}\int_4^{\infty} dz \operatorname{Im} T(z)\left[\frac{1}{z-s} - \frac{1}{z-2} + \frac{1}{z-t(s)} - \frac{1}{z-t(2)}\right] \\
&= \frac{1}{\pi}\int_4^{\infty} dz \operatorname{Im} T(z)\left[\frac{s-2}{(z-2)(z-s)} + \frac{t(s)-t(2)}{(z-2)(z-s)}\right] \\
&= \frac{1}{\pi}\int_4^{\infty} dz \operatorname{Im} T(z)\left[\frac{1}{z+s-4} + \frac{1}{z-s} - \frac{2}{z-2}\right]
\end{aligned} \tag{A.4}$$

All that remains are the integrals whose curves are surrounding the poles at $0 < s < 4$. Thus,

$$\begin{aligned}
T(s) &= -\frac{1}{2\pi i}\sum_i \int_{C_\epsilon(m_i^2)} dz\, \frac{T(z)}{z-s} \\
&= -\sum_i \operatorname*{Res}_{z=m_i^2} T(z) \times \left[\frac{1}{m_i^2 - s} - \frac{1}{4 - m_i^2 - s}\right] \\
&= \sum_i g_i^2 \times \left[\frac{1}{m_i^2 - s} - \frac{1}{t(m_i^2) - s}\right]
\end{aligned} \tag{A.5}$$

where the Residue Theorem and the fact that *s*- and *t*-channel poles have symmetric residues were used. Therefore,

$$\begin{aligned}
T(s) - T(2) &= \sum_i g_i^2 \times \left[\frac{1}{m_i^2 - s} - \frac{1}{m_i^2 - 2} - \frac{1}{t(m_i^2) - s} + \frac{1}{t(m_i^2) - 2}\right] \\
&= \sum_i g_i^2 \times \left[\frac{1}{m_i^2 - s} + \frac{1}{s + m_i^2 - 4} - \frac{2}{m_i^2 - 2}\right]
\end{aligned} \tag{A.6}$$

All in all,

$$\begin{aligned} 0 = \mathcal{A}(s) \equiv T(s) - T(2) - \sum_i g_i^2 \times \left[\frac{1}{m_i^2 - s} + \frac{1}{s + m_i^2 - 4} - \frac{2}{m_i^2 - 2}\right] \\ - \frac{1}{\pi}\int_4^\infty dz \,\mathrm{Im}\, T(z) \left[\frac{1}{z + s - 4} + \frac{1}{z - s} - \frac{2}{z - 2}\right] \end{aligned} \tag{A.7}$$

In the end, $\omega(s)$ must be integrated against $\mathcal{A}(s)$ (cf. Equation 2.39). However, there is a new primal variable that needs to be taken into account, $T(2)$, which, integrated against $\omega(s)$, yields the term $T(2) \times \int_4^\infty ds\, \omega(s)$. When taking the supremum in the space of $\{T(s), T(2), g_1^2\}$, it must be ensured that there are no divergences; then, $\int_4^\infty ds\, \omega(s) = 0$. Assuming that the integrals in s and z can be exchanged,

$$\begin{aligned} \int_4^\infty ds\, \omega(s) \left[\frac{1}{z + s - 4} + \frac{1}{z - s} - \frac{2}{z - 2}\right] &= \int_4^\infty ds\, \omega(s) \left[\frac{1}{z + s - 4} + \frac{1}{z - s}\right] \\ &= -\int_4^\infty ds\, \omega(s) \left[\frac{1}{s - z} - \frac{1}{s - t(z)}\right] \end{aligned} \tag{A.8}$$

Before proceeding, some details should be discussed. In the previous expression, s should be understood as $s = s + i0^+$, so as to make it very clear which ramification is being considered. Therefore, the integral can be thought of running exlcusively on the real axis. With this in mind, the previous expressions yields

$$\begin{aligned} &\int_4^\infty ds\, \omega(s) \left[\frac{1}{z + s - 4} + \frac{1}{z - s}\right] = \int_4^\infty ds\, \omega(s) \left[\frac{1}{z + s + i0^+ - 4} + \frac{1}{z - s - i0^+}\right] \\ &= \int_4^\infty ds\, \omega(s) \left[i\pi\delta(z - s) + \mathcal{P}\left[\frac{1}{s - z}\right] - i\pi\delta(s - t(z)) + \mathcal{P}\left[\frac{1}{z + s - 4}\right]\right] \\ &= i\pi\omega(s) + \int_4^\infty ds\, \omega(s) \left[\frac{1}{z - s} + \frac{1}{z + s - 4}\right] \\ &= i\pi\omega(s) - \int_4^\infty ds\, \omega(s) \left[\frac{1}{s - z} - \frac{1}{s - t(z)}\right] \\ &\equiv i\pi\omega(s) - \pi \mathrm{Re}\, W(s) \end{aligned} \tag{A.9}$$

This result can be obtained using the Sokhotski–Plemelj theorem, considering that $\omega(s)$ has support for $s \geq 4$ and defining an anti-crossing symmetric function $W(z)$, holomorphic in the complex plane without unitarity cuts,

$$\mathrm{Re}\, W(z) \equiv \frac{1}{\pi}\int_4^\infty ds\, \mathrm{Im}\, W(s) \left[\frac{1}{s - z} - \frac{1}{s - t(z)}\right] \tag{A.10}$$

such that $\operatorname{Im} W(s) = \omega(s)$ for $s \geq 4$. With this definition, Equation A.7 can be simplified to give

$$\begin{aligned}\int_4^\infty ds\,\omega(s)\mathcal{A}(s) &= \int_4^\infty ds\,\omega(s)\,T(s) + \int_4^\infty ds\,\operatorname{Im} T(s) \times \operatorname{Re} W(s) \\ &\quad - i\int_4^\infty ds\,\omega(s)\operatorname{Im} T(s) + \pi\sum_i g_i^2 \operatorname{Re} W(m_i^2) \\ &= \int_4^\infty ds\,\operatorname{Re} T(s) \times \operatorname{Im} W(s) + \int_4^\infty ds\,\operatorname{Im} T(s) \times \operatorname{Re} W(s) \\ &\quad + \pi\sum_i g_i^2 \operatorname{Re} W(m_i^2) \\ &= \int_4^\infty ds\,\operatorname{Im}\left[T(s)W(s)\right] + \pi\sum_i g_i^2 \operatorname{Re} W(m_i^2)\end{aligned} \tag{A.11}$$

At last, to make contact with Equation 2.46, we use the Sokhotski–Plemelj theorem to show that it is the same as Equation A.10:

$$\begin{aligned}W(s) &\equiv -\frac{1}{\pi}\int_{4m^2}^\infty dz\,\omega(z)\left(\frac{1}{s-z+i0^+} - \frac{1}{s-4+z+i0^+}\right) \\ &= -\frac{1}{\pi}\int_{4m^2}^\infty dz\,\omega(z)\left(-i\pi\delta(s-z) + \mathcal{P}\left[\frac{1}{s-z}\right] + i\pi\delta(s-4+z) - \mathcal{P}\left[\frac{1}{s-4+z}\right]\right) \\ &= i\left(\omega(s) + \omega(4-s)\right) + \frac{1}{\pi}\int_{4m^2}^\infty dz\,\omega(z)\left(\frac{1}{s-z} - \frac{1}{s-4+z}\right) \\ &= i\omega(s) + \frac{1}{\pi}\int_{4m^2}^\infty dz\,\omega(z)\left(\frac{1}{s-z} - \frac{1}{s-t(z)}\right)\end{aligned} \tag{A.12}$$

where we imposed that $\omega(s)$ has support only for $s \geq 4$. It is now straightforward to check that

$$\operatorname{Im} W(s) = \omega(s), \quad \operatorname{Re} W(s) = \frac{1}{\pi}\int_{4m^2}^\infty dz\,\omega(z)\left(\frac{1}{s-z} - \frac{1}{s-t(z)}\right) \tag{A.13}$$

Appendix B

Positive semidefinite constraints

B.1 Positive semidefinite matrices and partial-wave inequality

It is often the case that SDPB [4] must be used to perform numerical optimization. So as to make use of it, one is required to cast every constraint in a positive semidefinite matrix form: doing so calls for a base knowledge of what semidefinite matrices are.

Let A be a symmetric matrix whose entries are all positive (it may be generalized for complex matrices, but it is beyond the scope of this section). A is said to be *positive semidefinite*, $A \succeq 0$, if (the following conditions are all equivalent) [52–54]:

1. All eigenvalues of A are non-negative.
2. A = $U^T U$ for some matrix U.
3. $x^T A x \geq 0$ for every $x \in \mathbb{R}^n$.
4. All principal minors of A are non-negative.

In most cases, the first conditions is used. However, for our purposes, the last one is more useful.

As an example, we check if the matrix constraints used in Section 3.3 are positive semidefinite. We start by recovering the family of matrices at hand,

$$\begin{pmatrix} 1 - \frac{\operatorname{Im} a}{2} & \operatorname{Re} a \\ \operatorname{Re} a & 2 \operatorname{Im} a \end{pmatrix} \succeq 0 \tag{B.1}$$

where $a \equiv \sqrt{\frac{s-4}{s}} f_\ell(s)$. For a 2×2 matrix, the principal minors correspond to the diagonal entries. Thus,

$$\begin{aligned} 1 - \frac{\operatorname{Im} a}{2} \geq 0 \quad &\wedge \quad 2 \operatorname{Im} a \geq 0 \\ \Leftrightarrow \operatorname{Im} a \leq 2 \quad &\wedge \quad \operatorname{Im} a \geq 0 \end{aligned} \tag{B.2}$$

In addition, if all the eigenvalues are non-negative, it means that the determinant must be non-negative as well. Therefore,

$$2 \operatorname{Im} a \geq \operatorname{Im}^2 a + \operatorname{Re}^2 a \tag{B.3}$$

All of the conditions above are simply remnants of the unitarity condition, $|S_\ell(s)|^2 \leq 1$, and we proceed with proving so. If $S_\ell(s) = 1 + i \times a$, then

$$\begin{aligned} & |S_\ell(s)|^2 \leq 1, \quad s \geq 4m^2 \\ \Leftrightarrow\ & S_\ell^\dagger S_\ell \leq 1 \\ \Leftrightarrow\ & (1 - i \times a^\dagger(s))(1 + i \times a(s)) \leq 1 \\ \Leftrightarrow\ & 1 + i \left[a(s) - a^\dagger(s) \right] + |a(s)|^2 \leq 1 \\ \Leftrightarrow\ & 2 \operatorname{Im} a(s) \geq |a(s)|^2 = \operatorname{Im}^2 a + \operatorname{Re}^2 a \end{aligned} \tag{B.4}$$

which is precisely Equation B.3. To prove the remaining conditions, we shift our attention to the inequality $|S_\ell(s)| \leq 1$. The previous inequality implies that $-1 \leq \operatorname{Re} S_\ell(s) \leq 1$ at most. Developing this idea further,

$$\begin{aligned} & \operatorname{Re} S_\ell(s) \leq 1 \\ \Leftrightarrow\ & 1 - \operatorname{Im} a \leq 1 \\ \Leftrightarrow\ & \operatorname{Im} a \geq 0 \end{aligned} \tag{B.5}$$

and

$$\begin{aligned} & -1 \leq \operatorname{Re} S_\ell(s) \\ \Leftrightarrow\ & -1 \leq 1 - \operatorname{Im} a \\ \Leftrightarrow\ & \operatorname{Im} a \leq 2 \end{aligned} \tag{B.6}$$

which proves B.2. Hence, we conclude that the given matrix constraint is, in fact, positive semidefinite as required.

B.2 Partial-wave inequality generalization

In Appendix B.1, we showed that

$$\frac{|a(s)|^2}{2} \leq \operatorname{Im} a(s) \leq 2 \tag{B.7}$$

However, the study of particle production in 4D requires us to slightly modify this equation so as to impose an inelastic profile directly of the S-matrix partial-waves.

Let us consider that unitarity reads

$$|S_\ell(s)|^2 \leq \beta(s), \quad s \geq 4m^2 \tag{B.8}$$

Developing this expression,

$$\begin{aligned} |S_\ell(s)|^2 \leq \beta(s), \quad s \geq 4m^2 \\ \Leftrightarrow S_\ell^\dagger S_\ell \leq \beta(s) \\ \Leftrightarrow (1 - i \times a^\dagger(s))(1 + i \times a^\dagger(s)) \leq \beta(s) \\ \Leftrightarrow 1 + i\left[a(s) - a^\dagger(s)\right] + |a(s)|^2 \leq \beta(s) \\ \Leftrightarrow 2 \operatorname{Im} a(s) \geq |a(s)|^2 + 1 - \beta(s) \end{aligned} \tag{B.9}$$

To get the upper bound, we note that $|S_\ell(s)|^2 \leq \beta(s)$ implies that $-\sqrt{\beta(s)} \leq \operatorname{Re} S_\ell(s) \leq \sqrt{\beta(s)}$. Thus,

$$\begin{aligned} -\sqrt{\beta(s)} \leq \operatorname{Re} S_\ell(s) \\ \Leftrightarrow -\sqrt{\beta(s)} \leq 1 - \operatorname{Im} a \\ \Leftrightarrow \operatorname{Im} a \leq 1 + \sqrt{\beta(s)} \end{aligned} \tag{B.10}$$

In conclusion,

$$\frac{1 - \beta(s)}{2} + \frac{|a(s)|^2}{2} \leq \operatorname{Im} a(s) \leq 1 + \sqrt{\beta(s)} \tag{B.11}$$

If one were to impose these inequalities in the SDPB program, it would be needed to cast Equation B.11 in a positive semidefinite matrix condition. Unfortunately, doing so proves a bit arduous, and as such we resort to `Mathematica`. Since it must happen that $\operatorname{Im} a(s) \leq 1 + \sqrt{\beta(s)}$, which is the same as $1 - \frac{\operatorname{Im} a}{1+\sqrt{\beta(s)}} \geq 0$: this form is already known to us, and corresponds to the condition that the first entry on a positive semidefinite matrix

must be non-negative. Therefore, we propose the general matrix

$$\begin{pmatrix} 1-\frac{\operatorname{Im} a}{1+\sqrt{\beta(s)}} & \alpha_1+\alpha_2 \operatorname{Re} a+\alpha_3 \operatorname{Im} a \\ \alpha_4+\alpha_5 \operatorname{Re} a+\alpha_6 \operatorname{Im} a & \alpha_7+\alpha_8 \operatorname{Re} a+\alpha_9 \operatorname{Im} a \end{pmatrix} \succeq 0 \tag{B.12}$$

and impose that the determinant is precisely B.9. Doing so gives the matrix condition

$$\begin{pmatrix} 1-\frac{\operatorname{Im} a}{1+\sqrt{\beta(s)}} & \operatorname{Re} a \\ \operatorname{Re} a & \beta(s)-1+\left(1+\sqrt{\beta(s)}\right) \operatorname{Im} a \end{pmatrix} \tag{B.13}$$

In the limit $\beta(s) \to 1$, the matrix B.1 is recovered

$$\begin{pmatrix} 1-\frac{\operatorname{Im} a}{2} & \operatorname{Re} a \\ \operatorname{Re} a & 2 \operatorname{Im} a \end{pmatrix} \succeq 0 \tag{B.14}$$

which leads us to believe that the family of continuous matrix conditions B.13 is the appropriate one.

Appendix C

Bounds on the threshold pole coefficient

In section 3.4, the threshold pole was introduced so as to maximize the value of the amplitude at $s = t = u = 4/3$. However, changing the Ansatz 3.10 has some consequences, especially when imposing unitarity for each partial-wave. Therefore, such conditions serve as confirmation whether our optimization results are valid.

We start by recalling Equations 3.10 and 3.12, respectively

$$T(s,t,u) = \alpha\left(\frac{1}{\rho_s - 1} + \frac{1}{\rho_t - 1} + \frac{1}{\rho_u - 1}\right) + \sum_{a,b,c=0} \alpha_{abc}\, \rho_s^a \rho_t^b \rho_u^c \tag{C.1}$$

and

$$S_\ell(s) = 1 + \frac{i}{32\pi}\sqrt{\frac{s-4}{s}} \int_{-1}^{1} dx\, P_\ell(x) T(s, t(x)) \tag{C.2}$$

where, in the first one, the relevant modifications for the problem at hand were already made. Now, unitarity in the $\ell = 0$ partial-wave amplitude entails

$$|S_0(s)| \leq 1 \implies \operatorname{Re} S_0(s) \leq 1 \tag{C.3}$$

For this specific partial-wave, the relevant integral in C.2 is $\int_{-1}^{1} dx\, T(s, t(x))$, which we split into the *pole term* and the *triple ρ term*. Concerning the former,

$$\begin{aligned}\int_{-1}^{1} dx \left(\frac{1}{\rho_s - 1} + \frac{1}{\rho_t - 1} + \frac{1}{\rho_u - 1}\right) &= -1 - \frac{2}{\sqrt{6 - \frac{3s}{2}}} + \left[-1 - \frac{4\sqrt{\frac{2}{3}}}{2 + \sqrt{s}}\right] \times 2 \\ &= -3 - \frac{8\sqrt{\frac{2}{3}}}{2 + \sqrt{s}} - \frac{2}{\sqrt{6 - \frac{3s}{2}}}\end{aligned} \tag{C.4}$$

We expand the previous result (multiplied by $\sqrt{\frac{s-4}{s}}$) in a Taylor series near the threshold point, $s = 4m^2$. This results in the term

$$-i\sqrt{\frac{2}{3}} + \mathcal{O}(\sqrt{s-4}) \tag{C.5}$$

For the latter term, doing the same we find that,

$$\int_{-1}^{1} dx \sum_{a,b,c=0} \alpha_{abc}\, \rho_s^a \rho_t^b \rho_u^c = 2\alpha_{0,0,0} + (...)(\text{Real numbers}) \tag{C.6}$$

which near the threshold behaves like

$$\text{const.} + \mathcal{O}(\sqrt{s-4}) \tag{C.7}$$

Thus

$$\begin{aligned} S_0(s) &= 1 + \frac{i}{32\pi}\sqrt{\frac{s-4}{s}} \int_{-1}^{1} dx\, P_\ell(x) T(s, t(x)) \\ &= 1 + \frac{i}{32\pi}\left[i\alpha \left(-\sqrt{\frac{2}{3}} + \mathcal{O}(s-4) \right) + \text{const.} \right] \\ \implies \text{Re}\, S_0(s) &= 1 + \frac{\alpha}{32\pi}\sqrt{\frac{2}{3}} \\ \implies -1 &\leq 1 + \frac{\alpha}{16\sqrt{6}\pi} \leq 1 \\ \Leftrightarrow -32\sqrt{6}\pi &\leq \alpha \leq 0 \end{aligned} \tag{C.8}$$

Therefore, when looking for solutions to the optimization problem of the maximization of the quartic coupling subject to the usual constraints, α must comply with the conditions $-32\sqrt{6}\pi \leq \alpha \leq 0$.

Appendix D

Inelastic dual

In section 4.2, we introduced the dual objective without clarifying where the expression came from. Hopefully, in this appendix, we will make it clearer.

Similarly to subsection 2.2.1, we introduce the Lagrangian density function

$$\mathcal{L}(T,\omega,\lambda) = g_1^2 + \int_{4m^2}^{\infty} ds\ \omega(s)\mathcal{A}(s) + \lambda(s)\mathcal{U}(s) \tag{D.1}$$

where $\mathcal{A}(s)$ was related to the dispersive representation of the amplitude function and $\mathcal{U}(s)$ contained the unitarity condition. Since we wish to impose particle production, only the latter function must be modified accordingly, whereas $\mathcal{A}(s)$ still has the form

$$\mathcal{A}(s) \equiv T(s) - \left(T_\infty - \frac{g_1^2}{s-m_1^2} + \int_{4m^2}^{\infty} \frac{dz}{\pi} \frac{\operatorname{Im} T(z)}{s-z+i0^+} + (s \leftrightarrow 4m^2 - s) \right) = 0, \quad s \geq 4m^2 \tag{D.2}$$

To determine the most suitable form for $\mathcal{U}(s)$, we start by recalling that

$$S(s) \equiv 1 + i\frac{T(s)}{2\sqrt{s\left(s-4m^2\right)}} \tag{D.3}$$

According to the new unitarity condition,

$$\begin{aligned}
|S(s)|^2 \leq \beta(s), \quad s \geq 4m^2 \\
\Leftrightarrow S^*(s)S(s) \leq \beta(s) \\
\Leftrightarrow \left(1 + i\,\frac{T(s)}{2\sqrt{s(s-4)}}\right)\left(1 - i\,\frac{T^*(s)}{2\sqrt{s(s-4)}}\right) \leq \beta(s) \\
\Leftrightarrow 1 + i\,\frac{1}{2\sqrt{s(s-4)}}\left(T(s) - T^*(s)\right) + \frac{1}{4s(s-4)}\,|T(s)|^2 \leq \beta(s) \\
\Leftrightarrow 2\sqrt{s(s-4)}\left(1-\beta(s)\right) + 2\operatorname{Im} T(s) - \frac{1}{2\sqrt{s(s-4)}}\,|T(s)|^2 \geq 0
\end{aligned} \tag{D.4}$$

To check if Equation D.4 is consistent with Equation 2.38, we set $\beta(s) = 1$. Hence, the previous equation yields

$$2\,\mathrm{Im}\,T(s) - \frac{|T(s)|^2}{2\sqrt{s(s-4)}} \geq 0 \tag{D.5}$$

which checks out. Thus, we define

$$\mathcal{U}(s) \equiv 2\sqrt{s(s-4)}\,\big(1-\beta(s)\big) + 2\,\mathrm{Im}\,T(s) - \frac{1}{2\sqrt{s(s-4)}}\,|T(s)|^2 \geq 0 \tag{D.6}$$

With this new expression in mind, we carry out the same process as in subsection 2.2.1: one defines $d(\omega,\lambda) = \sup_{\{T,g_1^2\}} \mathcal{L}(T,\omega,\lambda)$, which we then try to minimize subject to $\lambda(s) \geq 0$. When varying $T(s)$ (in order to maximize the Lagrangian density), $T_c(s)$ remains the same, since the difference is in terms that are neither $\mathrm{Im}\,T(s)$ nor $\mathrm{Re}\,T(s)$. The only real difference is in the expression for $d(W,\lambda)$, which now reads

$$d(W,\lambda) = \int_{4m^2}^{\infty} ds\,\left[\frac{|W(s)|^2}{4\lambda(s)} + \mathrm{Re}\,W(s) + \beta(s)\lambda(s)\right]\frac{1}{\rho_{11}^2} \tag{D.7}$$

Minimizing over $\lambda(s)$, we now get the expression

$$D(W,\lambda) = \int_{4m^2}^{\infty} ds\,\left[|W(s)|\beta(s) + \mathrm{Re}\,W(s)\right]\frac{1}{\rho_{11}^2} \tag{D.8}$$

where $\lambda(s) = \frac{|W(s)|}{2\sqrt{\beta(s)}}$ is the chosen solution. Equation D.8 has all the right limits when $\beta(s) \to 1$ and corresponds to the expression used for the optimization process in section 4.2.

Bibliography

[1] R. J. Eden, P. V. Landshoff, D. I. Olive and J. C. Polkinghorne, *The analytic S-matrix* (Cambridge University Press, 2002).

[2] M. Correia, A. Sever and A. Zhiboedov, "An analytical toolkit for the s-matrix bootstrap," (2020).

[3] M. F. Paulos, J. Penedones, J. Toledo, B. C. van Rees and P. Vieira, *The S-matrix bootstrap II: two dimensional amplitudes*, Journal of High Energy Physics **2017** (2017), 10.1007/jhep11(2017)143.

[4] D. Simmons-Duffin, "A semidefinite program solver for the conformal bootstrap," (2015).

[5] J. T. Cushing, *Theory construction and selection in modern physics: The S matrix* (Cambridge University Press, 1990).

[6] J. Mehra, *The Conceptual Completion and Extensions of Quantum Mechanics 1932-1941. Epilogue: Aspects of the Further Development of Quantum Theory 1942-1999: Subject Index: Volumes 1 to 6* (Springer Science & Business Media, 2004).

[7] J. A. Wheeler, *On the mathematical description of light nuclei by the method of resonating group structure*, Physical Review **52**, 1107 (1937).

[8] M. Kruczenski, J. Penedones and B. C. van Rees, "Snowmass white paper: S-matrix bootstrap," (2022).

[9] G. Veneziano, *Construction of a crossing - symmetric, Regge behaved amplitude for linearly rising trajectories*, Nuovo Cim. A **57**, 190 (1968).

[10] R. Rattazzi, V. S. Rychkov, E. Tonni and A. Vichi, *Bounding scalar operator dimensions in 4D CFT*, Journal of High Energy Physics **2008**, 031 (2008).

[11] P. D. B. Collins, *An Introduction to Regge Theory and High Energy Physics*, Cambridge Monographs on Mathematical Physics (Cambridge University Press, 1977).

[12] D. Olive, *Unitarity and the evaluation of discontinuities*, Il Nuovo Cimento (1955-1965) **26**, 73 (1962).

[13] G. Sommer, *Present state of rigorous analytic properties of scattering amplitudes*, Fortschritte der Physik **18**, 577 (1970).

[14] N. Bogoliubov, B. Medvedev and M. Polivanov, "Voprossy teorii dispersionnykh sootnoshenii (fitmatgiz, moscow, 1958); nn bogoliubov and dv shirkov, introduction to the theory of quantized fields," (1959).

[15] H. Lehmann, *Analytic properties of scattering amplitudes as functions of momentum transfer*, Il Nuovo Cimento (1955-1965) **10**, 579 (1958).

[16] J. Bros, H. Epstein and V. Glaser, *Some rigorous analyticity properties of the four-point function in momentum space*, Il Nuovo Cimento (1955-1965) **31**, 1265 (1964).

[17] A. Martin, *Extension of the axiomatic analyticity domain of scattering amplitudes by unitarity-I*, Il Nuovo Cimento A (1965-1970) **42**, 930 (1966).

[18] J. Bros, H. Epstein and V. Glaser, *A proof of the crossing property for two-particle amplitudes in general quantum field theory*, Communications in Mathematical Physics **1**, 240 (1965).

[19] M. F. Paulos, J. Penedones, J. Toledo, B. C. van Rees and P. Vieira, "The s-matrix bootstrap iii: Higher dimensional amplitudes," (2017).

[20] P. Vieira, *(Mostly Two Dimensional) S-matrix Bootstrap*, Lecture Notes (2020).

[21] A. B. Zamolodchikov, *Exact Two Particle s Matrix of Quantum Sine-Gordon Solitons*, Pisma Zh. Eksp. Teor. Fiz. **25**, 499 (1977).

[22] I. Arefeva and V. Korepin, *Scattering in two-dimensional model with Lagrangian (1/gamma) ((d(mu)u)**2/2 + m**2 cos(u-1))*, Pisma Zh. Eksp. Teor. Fiz. **20**, 680 (1974).

[23] M. Hogervorst and S. Rychkov, *Radial coordinates for conformal blocks*, Physical Review D **87** (2013), 10.1103/physrevd.87.106004.

[24] P. Dorey, in *Eotvos Summer School in Physics: Conformal Field Theories and Integrable Models* (1996) pp. 85–125, arXiv:hep-th/9810026 .

[25] A. B. Zamolodchikov and A. B. Zamolodchikov, *Factorized S-matrices in two dimensions as the exact solutions of certain relativistic quantum field theory models*, Annals of Physics **120**, 253 (1979).

[26] M. Creutz, *Rigorous Bounds on Coupling Constants in Two-Dimensional Field Theories*, Phys. Rev. D **6**, 2763 (1972).

[27] G. Mussardo and P. Simon, *Bosonic-type S -matrix, vacuum instability and CDD ambiguities*, Nuclear Physics B **578**, 527 (2000).

[28] H. Chen, A. L. Fitzpatrick and D. Karateev, *Bootstrapping 2d ϕ^4 theory with Hamiltonian truncation data*, Journal of High Energy Physics **2022** (2022), 10.1007/jhep02(2022)146.

[29] S. Caron-Huot and V. Van Duong, *Extremal effective field theories*, Journal of High Energy Physics **2021**, 1 (2021).

[30] A. B. Zamolodchikov, *Resonance factorized scattering and roaming trajectories*, Journal of Physics A: Mathematical and General **39**, 12847 (2006).

[31] L. Córdova, Y. He, M. Kruczenski and P. Vieira, *The O(N) S-matrix monolith*, Journal of High Energy Physics **2020** (2020), 10.1007/jhep04(2020)142.

[32] A. L. Guerrieri, A. Homrich and P. Vieira, *Dual S-matrix bootstrap. Part I. 2D theory*, Journal of High Energy Physics **2020** (2020), 10.1007/jhep11(2020)084.

[33] A. L. Guerrieri, J. Penedones and P. Vieira, *Bootstrapping QCD Using Pion Scattering Amplitudes*, Physical Review Letters **122** (2019), 10.1103/physrevlett.122.241604.

[34] S. Mizera, *Crossing symmetry in the planar limit*, Physical Review D **104** (2021), 10.1103/physrevd.104.045003.

[35] S. Mizera, *Bounds on Crossing Symmetry*, Phys. Rev. D **103**, 081701 (2021), arXiv:2101.08266 [hep-th] .

[36] D. Poland, D. Simmons-Duffin and A. Vichi, *Carving out the space of 4D CFTs*, Journal of High Energy Physics **2012** (2012), 10.1007/jhep05(2012)110.

[37] A. Homrich, J. Penedones, J. Toledo, B. C. van Rees and P. Vieira, *The S-matrix bootstrap IV: multiple amplitudes*, Journal of High Energy Physics **2019** (2019), 10.1007/jhep11(2019)076.

[38] A. Hebbar, D. Karateev and J. Penedones, "Spinning s-matrix bootstrap in 4d," (2020).

[39] C. Lopez and G. Mennessier, *Bounds on the pi0 pi0 Amplitude*, Nucl. Phys. B **118**, 426 (1977).

[40] L. Lukaszuk and A. Martin, *Absolute upper bounds for pi pi scattering*, Nuovo Cim. A **52**, 122 (1967).

[41] J. B. Healy, *New Rigorous Bounds on Coupling Constants in Field Theory*, Phys. Rev. D **8**, 1904 (1973).

[42] G. Auberson, L. Epele, G. Mahoux and F. R. A. Simao, *Rigorous Absolute Bounds for Pion Pion Scattering. 3. Dispersion Relations on Algebraic Manifolds and Computation of Bounds*, Nucl. Phys. B **94**, 311 (1975).

[43] B. Bonnier, C. Lopez and G. Mennessier, *Improved Absolute Bounds on the pi0 pi0 Amplitude*, Phys. Lett. B **60**, 63 (1975).

[44] G. Auberson, L. Epele and F. Simão, *Almost optimality of an axiomatic bound for pi0pi0 scattering*, Nuclear Physics B **133**, 266 (1978).

[45] A. Guerrieri, J. Penedones and P. Vieira, *Where Is String Theory in the Space of Scattering Amplitudes?*, Physical Review Letters **127** (2021), 10.1103/physrevlett.127.081601.

[46] A. L. Guerrieri, J. Penedones and P. Vieira, *S-matrix bootstrap for effective field theories: massless pions*, Journal of High Energy Physics **2021** (2021), 10.1007/jhep06(2021)088.

[47] M. E. Peskin, *An introduction to quantum field theory* (CRC press, 2018).

[48] P. Tourkine and A. Zhiboedov, *Scattering from production in 2d*, Journal of High Energy Physics **2021** (2021), 10.1007/jhep07(2021)228.

[49] M. D. Schwartz, *Quantum field theory and the standard model* (Cambridge University Press, 2014).

[50] A. Martin and S. Roy, *Lower bound on inelasticity in pion-pion scattering*, Physical Review D **96** (2017), 10.1103/physrevd.96.114014.

[51] A. Sinha and A. Zahed, *Crossing Symmetric Dispersion Relations in Quantum Field Theories*, Physical Review Letters **126** (2021), 10.1103/physrevlett.126.181601.

[52] A. Van den Bos, *Appendix C: Positive Semidefinite and Positive Definite Matrices*, Parameter Estimation for Scientists and Engineers. John Wiley & Sons, Inc , 259 (2007).

[53] R. Bahtia, "Positive definite matrices, princeton series in applied mathematics," (2007).

[54] R. A. Horn and C. R. Johnson, *Matrix analysis* (Cambridge university press, 2012).